

Dynamical Systems and Scalar Fields in Cosmology

Tsikoundoura Anna
8388

Supervisor: Leandros Perivolaropoulos
University of Ioannina
Department of Physics
Ioannina, 2025

“ The universe is not only
queerer than we suppose, but
queerer than we can suppose ”

– John B. S. Haldane

Abstract

This thesis investigates two non-interacting quintessence models: one with an exponential self-interacting potential and another with an inverse power-law potential. Through a dynamical systems analysis, we find that the first model fails to account for the observed accelerating expansion of the universe, while the latter succeeds in doing so but encounters challenges with the theoretical and observational consistency of its parameters. Additionally, we numerically explore the dynamics of quintessence and phantom scalar fields with a step-like potential. Both models exhibit a continuous Hubble parameter with a change in slope and a sharp variation in the deceleration parameter at the onset of the transition. Concurrently, the quintessence model displays a positive spike in the field's equation of state parameter due to the gained kinetic energy, whereas the phantom field demonstrates either a negative spike or a pole, depending on its amplitude. Finally, a statistical analysis is performed to fit the phantom field model to observational data, yielding best-fit parameters of $z_t = 3.00$, $h = 0.7104$ and $s = 0.001$, with $\Delta\text{AIC} = -9.44$ and $\Delta\text{BIC} = -4.00$. In this scenario, the comoving angular diameter distance to last scattering deviates by approximately 0.3% from that of the ΛCDM model, and the absolute magnitude of supernovae is found to exhibit a 3.1σ discrepancy with the value obtained from Cepheid measurements.

Acknowledgments

I would like to thank professor Leandros Perivolaropoulos for his valuable discussions, guidance, and continuous support throughout the course of this work. I would also like to extend my thanks to ChatGPT for facilitating the writing of this thesis in English.

Contents

Abstract	1
Introduction	6
1 Dynamical Systems	9
1.1 Introduction to dynamical systems	9
1.2 Linear stability analysis	10
1.2.1 Example	11
1.3 Center manifold theory	12
2 Modern Cosmology	15
2.1 The cosmological principle	15
2.2 Hubble's Law	16
2.3 FLRW cosmology	17
2.4 Friedmann equations	18
2.5 Dark energy	20
2.6 Alternatives to dark energy	21
3 Observational Cosmology	22
3.1 Cosmic distance ladder	22
3.1.1 Parallax	22
3.1.2 Cepheids	23
3.1.3 Type Ia Supernovae (SNIa)	24
3.2 Baryonic Acoustic Oscillations (BAO)	25
3.3 Cosmic Microwave Background (CMB)	27
3.4 The χ^2 function	29
3.4.1 SNIa	30
3.4.2 BAO	30
3.4.3 CMB	32

4	Scalar Fields	33
4.1	Quintessence fields	33
4.2	Phantom fields	36
5	Dynamical Systems In Cosmology	38
5.1	Introduction	38
5.2	Λ CDM	39
5.2.1	Dynamical analysis	39
5.2.2	Challenges of the model	42
5.3	Quintessence	43
5.3.1	Exponential potential	45
5.3.2	Inverse power-law potential	51
6	Transition Quintessence	55
6.1	Unified Dark Matter	55
6.2	Λ_s CDM	56
6.3	Step-like potential	59
6.3.1	Qualitative behavior	60
6.3.2	Statistical analysis	66
	Conclusions	70
A	Derivation of Friedmann Equations	72
A.1	Einstein field equations	72
A.2	Friedmann equations	75
B	Center Manifold Theory with Inverse Power-Law Potential	79
B.1	Fixed point E	79
B.2	Fixed point C	81
B.3	Fixed point D	82
C	Proof of the Rescaled Cosmological Equations	83
	Bibliography	87

List of Figures

3.1	Stellar parallax.	23
3.2	The period-luminosity relation for Milky Way Cepheids [64].	24
3.3	Light curves of various SNIa before (left) and after (right) calibration [65].	25
3.4	The temperature power spectrum of CMB. The light-blue curve represents the theoretical predictions of the Λ CDM model [75].	28
5.1	Phase space portrait for the Λ CDM dynamical system. The pink region indicates the area where the acceleration of the universe can occur.	42
5.2	The phase space portrait for the exponential potential with $0 < \lambda^2 < 3(w_b + 1)$ (specifically, $\lambda = 1$ and $w_b = 0$). As before, the pink region indicates the area where the acceleration of the universe can occur.	48
5.3	The phase space portrait for the exponential potential with $3(w_b + 1) < \lambda^2 < 6$ (specifically, $\lambda = 2$ and $w_b = 0$).	49
5.4	The phase space portrait for the exponential potential with $\lambda^2 > 6$ (specifically, $\lambda = 3$ and $w_b = 0$).	50
5.5	The phase space portrait for the inverse power-law potential, with the specific parameters set as $w_b = 0$ and $\Gamma = 1.1$	54
6.1	The EoS parameter for quintessence with $\Delta V = 0.1$, $\phi_t = 2$ and $s = 0.001$. Each line represents a different initial value of the field, leading to variations in speed and z_t	60
6.2	The Hubble parameter in the quintessence case with $\Delta V = 0.5$, $s = 0.001$ and $n = 5$ (dashed line), $n = 5.6$ (dot-dashed line) and $n = 6$ (thick line). The dot-dashed black line represents the Λ CDM.	61
6.3	The deceleration parameter in the quintessence case with $\Delta V = 0.1$, $s = 0.001$ and $n = 5$ (dashed line) and $n = 4$ (thick line). The dot-dashed black line represents the Λ CDM.	62
6.4	Energy density parameter for phantom field with transition redshift $z_t = 2.32$ (thick line) and $z_t = 2.45$ (dashed line).	63

6.5	EoS parameter for a phantom field whose energy density changes sign (thick line) and another that does not (dashed line).	63
6.6	The effective EoS parameter in the case of a phantom field with $\Delta V = -0.7$, $s = 0.001$ and $z_t = 3.00$	64
6.7	The Hubble parameter in the case of a phantom field with $\Delta V = -0.7$ and $s = 0.001$. The dot-dashed black line represents the Λ CDM.	64
6.8	The deceleration parameter for phantom field with $\Delta V = -0.7$ and $s = 0.001$. The dot-dashed black line represents the Λ CDM, while the dashed red line represents the Λ_s CDM with a transition at $z_t = 2.3$	65

List of Tables

4.1	Summary of the Friedmann equations and the EoS parameter for different cosmological models.	37
5.1	Properties of the critical points for the autonomous system of Λ CDM.	41
5.2	Properties of the critical points for the autonomous system with the exponential potential. Here $\Delta = \sqrt{(w_b - 1) ((7 + 9w_b)\lambda^2 - 24(w_b + 1)^2)}$	46
5.3	Properties of the critical points for the autonomous system with the inverse power-law potential.	52
6.1	Comparison of the best-fit parameters for Λ CDM and the scalar field model with a step-like potential across different datasets.	67
6.2	The value of z_t for each h , ensuring that $D_M(z_{ls})$ matches that of the Λ CDM model.	68

Introduction

Our universe remains a profoundly enigmatic place, and cosmologists continuously try to unravel its mysteries using every tool at their disposal. Current cosmological understanding suggests that the universe began with a Hot Big Bang (in [1, 2] a second Big Bang, named “Dark Big Bang”, is proposed), but while we have made significant progress in understanding its origins, the ultimate fate of the universe remains uncertain. Observations of the universe’s accelerating expansion [3–5] have led to the hypothesis that it may culminate in a catastrophic event, such as the Big Rip [6–8]. This accelerated expansion is attributed to vacuum energy, which forms the foundation of the standard cosmological model, Λ CDM. Although this model effectively explains many observational phenomena, it is not without its shortcomings [9–13]. One of the most prominent challenges to the Λ CDM framework is the so-called “Hubble tension”. This refers to the discrepancy in the measured values of the Hubble constant (H_0) when derived using different methods, such as local distance measurements versus observations of the cosmic microwave background. These tensions suggests the possibility of physics beyond the standard model, hinting at the need for an even more comprehensive cosmological framework.

In an effort to address these challenges, the concept of quintessence was introduced [14–16]. Quintessence is a scalar field that evolves over time under the influence of a potential, offering a dynamic explanation for dark energy. This framework is broadly classified into two categories: non-interacting quintessence and interacting quintessence [17–20], the latter involving interactions between dark energy and dark matter. They are further characterized based on the behavior of their potentials. They can be divided into thawing models [21, 22], where the scalar field is initially frozen and begins to evolve as the universe expands, and freezing models [23], where the field evolves rapidly at first but gradually slows down as it approaches a stable state.

Generally, most attempts to address the H_0 tension can be categorized into early- and late-time modifications of the Λ CDM expansion history. Early-time

modifications [24–27] focus on altering the sound horizon r_s , which affects the inferred value of H_0 from the Cosmic Microwave Background (CMB). In contrast, late-time modifications [28–31] aim to increase H_0 by adjusting the expansion history during more recent epochs. Additionally, gravitational transition models [32–36] have been proposed as a potential solution to the Hubble tension. These models involve a rapid change in the effective gravitational coupling G_{eff} at low redshift, which alters the inferred absolute magnitude of type Ia supernovae M [37, 38], thus providing a better fit than smooth $H(z)$ models. However, recent studies suggest that the origin of the Hubble tension may arise from systematic issues inherent in the distance ladder method or from an incomplete understanding of local physics [39].

Therefore, the question is, can we identify a framework superior to the Λ CDM model for explaining dark energy? This thesis aims to explore alternative theories that could account for the accelerated expansion of the universe. But how can we assess the viability of a cosmological model? The simplest answer lies in solving the Einstein field equations within a cosmological context; however, due to their complexity and non-linear nature, obtaining analytical solutions is often impractical. This is where the theory of dynamical systems becomes a valuable tool. While it may not provide precise solutions, dynamical systems theory allows us to gain qualitative insights into the behavior of a model. By analyzing critical points and their stability, we can evaluate whether a model is theoretically consistent and compatible with observational constraints. If the initial results are promising, more rigorous and precise methods can then be employed to further refine the model and its predictions.

This thesis is organized into six chapters and three appendices, each addressing a distinct aspect of the study. Chapter 1 introduces the fundamental principles of dynamical systems, providing the mathematical foundation necessary for the analysis conducted in later chapters. It includes an overview of linear stability analysis and center manifold theory, tools that are applied throughout this work. Chapter 2 presents the theoretical framework of modern cosmology, discussing essential topics such as the cosmological principle, Hubble’s law, the FLRW metric, and the Friedmann equations, along with an introduction to dark energy and its alternatives. Chapter 3 explores the observational foundation of cosmology, outlining key methods for measuring cosmic distances and constraining cosmological parameters. It discusses the cosmic distance ladder, from parallax and Cepheid variables to Type Ia supernovae, followed by Baryon Acoustic Oscillations (BAO) and the Cosmic Microwave Background (CMB) as probes of the universe’s expansion and structure. Finally, it introduces the χ^2 function as a statistical tool for comparing

theoretical models with observational data. Chapter 4 introduces quintessence and phantom fields, outlining their fundamental properties and equations.

Building on this foundation, Chapter 5 applies dynamical systems theory to cosmology, starting with an analysis of the Λ CDM model and its challenges. This chapter then investigates the dynamical behavior of quintessence models with exponential and inverse power-law potentials, providing qualitative insights into their evolution. Chapter 6 transitions to more advanced models, including unified dark matter (UDM), the Λ_s CDM framework, and phantom scalar fields with step-like potentials. For the phantom field model, both qualitative behavior and a detailed statistical analysis are performed to evaluate its compatibility with observational data.

The appendices provide supplementary material to support the main text. Appendix A derives the Friedmann equations starting from the Einstein field equations, ensuring a self-contained treatment of the theoretical framework. Appendix B delves deeper into the center manifold theory applied to the inverse power-law potential, offering detailed analysis of specific fixed points. Finally, Appendix C presents a proof of the rescaled cosmological equations used in Section 6.3.

Throughout this thesis, natural units ($c = \hbar = 1$) are used, and the metric signature is chosen to be $(+, -, -, -)$. All mathematical computations and symbolic analyses have been performed using Wolfram Mathematica 13 and the corresponding files can be found [here](#).

Chapter 1

Dynamical Systems

The purpose of this chapter is to establish the mathematical framework that will be employed throughout this thesis [40–43].

1.1 Introduction to dynamical systems

A dynamical system determines the temporal behavior of an evolutionary process, providing qualitative insights when analytical solutions are unattainable. The temporal evolution can be either continuous or discrete. Our focus will be solely on the continuous-time case, as it is of particular interest in cosmology. In such scenarios, systems are described by ordinary differential equations (ODEs) since the only independent variable involved is time, which does not necessarily coincide with cosmic time.

The mathematical representation of the system is [40]

$$\frac{d\mathbf{x}}{dt} \equiv \dot{\mathbf{x}} = \mathbf{f}(\mathbf{x}, t), \quad (1.1)$$

where $\mathbf{x} = \mathbf{x}(t) \in \mathbb{R}^n$, $t \in I \subseteq \mathbb{R}$ is the vector representing the dynamics of the continuous system. The function $\mathbf{f}(\mathbf{x}, t)$ is a sufficiently smooth function defined on a subset $U \subset \mathbb{R}^{n+1}$, usually nonlinear. The space \mathbb{R}^n , in which the vector $\mathbf{x}(t)$ evolves, constitutes the phase space of the system.

There are two classes of dynamical systems. The first consists of ODEs explicitly dependent on time, while the second comprises ODEs that do not explicitly depend on time; the latter are referred to as non-autonomous dynamical systems and autonomous dynamical systems, respectively. In this thesis, we will focus

exclusively on autonomous dynamical systems, and equation (1.1) takes the form,

$$\frac{d\mathbf{x}}{dt} \equiv \dot{\mathbf{x}} = \mathbf{f}(\mathbf{x}). \quad (1.2)$$

Each solution of equation (1.2), denoted by $\psi(t)$, corresponds to a point moving along a curve in the phase space, commonly referred to as a trajectory or orbit. There are an infinite number of trajectories that would fill the phase space when they are plotted. However, the qualitative behavior can be defined by plotting just a few trajectories with different initial conditions. The set of these trajectories is called phase portrait.

To study the local behavior of a system, we need to identify its fixed points, also known as equilibrium points or critical points.

Definition 1: The autonomous system (1.2) is said to have a fixed point at $\mathbf{x} = \mathbf{x}_0$ if and only if $\dot{\mathbf{x}}_0 = 0 \Rightarrow \mathbf{f}(\mathbf{x}_0) = 0$.

From the above definition, can be concluded that at a fixed point, the system remains unchanged. Nevertheless, the goal is to determine the behavior of trajectories near those points under small perturbations. This leads us to the need to study the stability of the system's fixed points.

Without giving the mathematical definitions, a stable fixed point is one where trajectories initially close remain close at all later times. If it is stable and solutions approach it for all nearby initial conditions, then it is called asymptotically stable. Otherwise, it is unstable and trajectories that start sufficiently close move away from it over time.

1.2 Linear stability analysis

The most straight forward approach to study the stability of a fixed point is by analyzing the nonlinear system through its linearized counterpart.

Expanding $\mathbf{f}(\mathbf{x})$ in the neighborhood of the fixed point \mathbf{x}_0 gives

$$\mathbf{f}(\mathbf{x}) = \mathbf{f}(\mathbf{x}_0) + (\mathbf{x} - \mathbf{x}_0) \left. \frac{\partial \mathbf{f}}{\partial \mathbf{x}} \right|_{\mathbf{x}=\mathbf{x}_0} + \mathcal{O}(|\mathbf{x} - \mathbf{x}_0|^2). \quad (1.3)$$

By definition, $\mathbf{f}(\mathbf{x}_0) = 0$. Neglecting quadratic or higher terms due to their smallness, since $\mathbf{x} - \mathbf{x}_0 = \delta\mathbf{x}$ is a small perturbation, we obtain the linearized

system

$$\delta\dot{\mathbf{x}} = J\delta\mathbf{x}, \quad (1.4)$$

where $J = D\mathbf{f}(\mathbf{x}_0)$ is the Jacobian matrix evaluated at the critical point \mathbf{x}_0 , from which information about the stability of the fixed point can be derived based on its eigenvalues.

If all the eigenvalues of the Jacobian matrix have positive real parts, the corresponding fixed point is an unstable node. On the other hand, if all the eigenvalues of the Jacobian matrix have negative real parts, it is a stable node. And lastly, if the eigenvalues of the Jacobian matrix have opposite signs, the fixed point is a saddle node; meaning that there are trajectories attracted to it and others that are repelled.

Definition 2: A fixed point is called hyperbolic if none of the eigenvalues of the Jacobian matrix, evaluated at that point, have zero real part.

The Hartman-Grobman Theorem: The behavior of a nonlinear dynamical system in a domain near a hyperbolic fixed point is qualitative the same as the behavior of its linearization near this fixed point.

Linearization, unfortunately, has its limitations; it only applies to hyperbolic fixed points. When dealing with non-hyperbolic fixed points, determining their stability properties using the linearized system becomes impossible¹. If at least one of the non-zero eigenvalues has positive real part, the fixed point is asymptotically unstable. However, when all non-zero eigenvalues have negative real parts, it is uncertain whether the point is stable or a saddle. For this reason, alternative methods are necessary for a conclusive analysis.

1.2.1 Example

Consider the 2-D dynamical system [41]

$$\dot{x} = x + y^2 \quad (1.5a)$$

$$\dot{y} = -y. \quad (1.5b)$$

¹The system is not structurally stable; therefore, a small perturbation might alter the qualitative behavior of the system.

To determine the fixed points, we set $\dot{x} = \dot{y} = 0$ which yields a single fixed point at the origin $(0, 0)$. The Jacobian matrix of the system evaluated at this point is

$$J|_{(0,0)} = \begin{pmatrix} \partial_x(x + y^2) & \partial_y(x + y^2) \\ \partial_x(-y) & \partial_y(-y) \end{pmatrix}_{(0,0)} = \begin{pmatrix} 1 & 0 \\ 0 & -1 \end{pmatrix}. \quad (1.6)$$

The eigenvalues of the Jacobian are $\lambda = \pm 1$, which indicate that the fixed point $(0, 0)$ is a saddle point.

1.3 Center manifold theory

One alternative method is the Lyapunov stability analysis. This approach is applicable to both hyperbolic and non-hyperbolic fixed points. Although a powerful tool, one must find the so-called Lyapunov function, which is not an easy task, especially for complex nonlinear systems since there is no systematic procedure to deduct it.

That leads us to another method for studying the stability of non-hyperbolic fixed points, the center manifold theory. The advantage of this method lies to the reduction of the system's dimensionality and the determination of the stability properties from the reduced system. One can determine the behavior of the nonlinear system by examining the qualitative behavior of the flow on the center manifold near the non-hyperbolic fixed point.

Consider the nonlinear dynamical system (1.2), having a fixed point at \mathbf{x}_0 . Transforming the fixed point to the origin using the translation $\bar{\mathbf{x}} = \mathbf{x} - \mathbf{x}_0$ and Taylor expanding about $\mathbf{x} = \mathbf{x}_0$ gives

$$\dot{\bar{\mathbf{x}}} = J\bar{\mathbf{x}} + \mathbf{R}(\bar{\mathbf{x}}) \quad (1.7)$$

where $\mathbf{R}(\bar{\mathbf{x}}) = \mathcal{O}(|\bar{\mathbf{x}}|^2)$. It is always possible to find a similarity transformation T that transforms the Jacobian matrix J into a block diagonal matrix Λ , such that

$$TJT^{-1} = \Lambda = \begin{pmatrix} A & 0 & 0 \\ 0 & B & 0 \\ 0 & 0 & C \end{pmatrix} \quad (1.8)$$

where A is an $s \times s$ matrix with all of its eigenvalues having a negative real part, B is an $u \times u$ matrix having eigenvalues with positive real part, and C is an $c \times c$

matrix with zero real part eigenvalues. Now the system (1.7) takes the form [42]

$$\dot{\mathbf{x}} = A\mathbf{x} + \mathbf{F}(\mathbf{x}, \mathbf{y}, \mathbf{z}) \quad (1.9a)$$

$$\dot{\mathbf{y}} = B\mathbf{y} + \mathbf{G}(\mathbf{x}, \mathbf{y}, \mathbf{z}) \quad (1.9b)$$

$$\dot{\mathbf{z}} = C\mathbf{z} + \mathbf{H}(\mathbf{x}, \mathbf{y}, \mathbf{z}) \quad (1.9c)$$

where $(\mathbf{x}, \mathbf{y}, \mathbf{z}) \in \mathbb{R}^s \times \mathbb{R}^u \times \mathbb{R}^c$, $\mathbf{F}(0) = \mathbf{G}(0) = \mathbf{H}(0) = 0$ and $D\mathbf{F}(0) = D\mathbf{G}(0) = D\mathbf{H}(0) = 0$

The Center Manifold Theorem[43]: Suppose (1.9) is C^r , $r \geq 2$. Then the fixed point $(\mathbf{x}, \mathbf{y}, \mathbf{z}) = 0$ of (1.9) possesses a C^r s -dimensional local, invariant stable manifold, $W^s(0)$, a C^r u -dimensional local, invariant unstable manifold, $W^u(0)$, and a C^r c -dimensional local, invariant center manifold, $W^c(0)$, all intersecting at $(\mathbf{x}, \mathbf{y}, \mathbf{z}) = 0$. These manifolds are all tangent to the respective invariant subspaces of the linear vector field at the origin and, hence, are locally representable as graphs. In particular,

$$\begin{aligned} W^s(0) &= \{(\mathbf{x}, \mathbf{y}, \mathbf{z}) \in \mathbb{R}^s \times \mathbb{R}^u \times \mathbb{R}^c \mid \mathbf{y} = h_1^s(\mathbf{x}), \mathbf{z} = h_2^s(\mathbf{x}); \\ &\quad Dh_1^s(0) = Dh_2^s(0) = 0; |\mathbf{x}| \text{ sufficiently small} \} \end{aligned}$$

$$\begin{aligned} W^u(0) &= \{(\mathbf{x}, \mathbf{y}, \mathbf{z}) \in \mathbb{R}^s \times \mathbb{R}^u \times \mathbb{R}^c \mid \mathbf{x} = h_1^u(\mathbf{y}), \mathbf{z} = h_2^u(\mathbf{y}); \\ &\quad Dh_1^u(0) = Dh_2^u(0) = 0; |\mathbf{y}| \text{ sufficiently small} \} \end{aligned}$$

$$\begin{aligned} W^c(0) &= \{(\mathbf{x}, \mathbf{y}, \mathbf{z}) \in \mathbb{R}^s \times \mathbb{R}^u \times \mathbb{R}^c \mid \mathbf{x} = h_1^c(\mathbf{z}), \mathbf{y} = h_2^c(\mathbf{z}); \\ &\quad Dh_1^c(0) = Dh_2^c(0) = 0; |\mathbf{z}| \text{ sufficiently small} \} \end{aligned}$$

It is important to note that trajectories initially located within the local stable manifold $W^s(0)$ tend to converge exponentially towards the origin as time progresses towards positive infinity, whereas trajectories with initial conditions within the local unstable manifold $W^u(0)$ diverge from the origin. As for trajectories in the local center manifold $W^c(0)$, they exhibit a more complex behavior such as oscillatory, periodic, or other neutral modes of motion. Therefore, our focus is on understanding the dynamics of trajectories in the local center manifold of the origin.

The flow on the center manifold of the origin is governed by

$$\dot{\mathbf{z}} = C\mathbf{z} + \mathbf{H}(h_1(\mathbf{z}), h_2(\mathbf{z}), \mathbf{z}). \quad (1.10)$$

This implies that we need to determine the forms of $h_1(\mathbf{z})$ and $h_2(\mathbf{z})$ to study the behavior of the system within the center manifold of the origin.

By definition, $\mathbf{x} = h_1(\mathbf{z})$ and $\mathbf{y} = h_2(\mathbf{z})$. Differentiating them with respect to time gives,

$$\dot{\mathbf{x}} = \frac{dh_1(\mathbf{z})}{dt} = \frac{\partial h_1}{\partial \mathbf{z}} \frac{d\mathbf{z}}{dt} = Dh_1(\mathbf{z}) \dot{\mathbf{z}} \quad (1.11)$$

$$\dot{\mathbf{y}} = \frac{dh_2(\mathbf{z})}{dt} = \frac{\partial h_2}{\partial \mathbf{z}} \frac{d\mathbf{z}}{dt} = Dh_2(\mathbf{z}) \dot{\mathbf{z}} \quad (1.12)$$

Since every point on the center manifold $W^c(0)$ obeys the dynamics of the system (1.9), equations (1.9a) and (1.9b) take the forms

$$Dh_1(\mathbf{z}) [C\mathbf{z} + \mathbf{H}(h_1(\mathbf{z}), h_2(\mathbf{z}), \mathbf{z})] = Ah_1(\mathbf{z}) + \mathbf{F}(h_1(\mathbf{z}), h_2(\mathbf{z}), \mathbf{z}) \quad (1.13)$$

$$Dh_2(\mathbf{z}) [C\mathbf{z} + \mathbf{H}(h_1(\mathbf{z}), h_2(\mathbf{z}), \mathbf{z})] = Bh_2(\mathbf{z}) + \mathbf{G}(h_1(\mathbf{z}), h_2(\mathbf{z}), \mathbf{z}) \quad (1.14)$$

where we have used equation (1.10) to substitute $\dot{\mathbf{z}}$.

Rearranging (1.13) and (1.14), we get the quasilinear partial differential equations that $h_1(\mathbf{z})$ and $h_2(\mathbf{z})$ must satisfy.

$$\begin{aligned} N_1(h_1(\mathbf{z}), h_2(\mathbf{z})) &\equiv \\ Dh_1(\mathbf{z}) [C\mathbf{z} + \mathbf{H}(h_1(\mathbf{z}), h_2(\mathbf{z}), \mathbf{z})] - Ah_1(\mathbf{z}) - \mathbf{F}(h_1(\mathbf{z}), h_2(\mathbf{z}), \mathbf{z}) &= 0 \end{aligned} \quad (1.15)$$

$$\begin{aligned} N_2(h_1(\mathbf{z}), h_2(\mathbf{z})) &\equiv \\ Dh_2(\mathbf{z}) [C\mathbf{z} + \mathbf{H}(h_1(\mathbf{z}), h_2(\mathbf{z}), \mathbf{z})] - Bh_2(\mathbf{z}) - \mathbf{G}(h_1(\mathbf{z}), h_2(\mathbf{z}), \mathbf{z}) &= 0 \end{aligned} \quad (1.16)$$

Although solving the above equations is very difficult, if not impossible, we can approximate the solutions to any degree of accuracy we desire.

The Approximation Theorem: Let $\phi : \mathbb{R}^c \rightarrow \mathbb{R}^s$ be a mapping with $\phi(0) = D\phi(0) = 0$ such that $N_1(\phi(\mathbf{z})) = \mathcal{O}(|\mathbf{z}|^q)$ as $\mathbf{z} \rightarrow 0$ for some $q > 1$. Then

$$|h_1(\mathbf{z}) - \phi(\mathbf{z})| = \mathcal{O}(|\mathbf{z}|^q) \text{ as } \mathbf{z} \rightarrow 0$$

The above theorem also applies if $\phi : \mathbb{R}^c \rightarrow \mathbb{R}^u$, making the necessary modifications.

Chapter 2

Modern Cosmology

This section aims to introduce the fundamentals of modern cosmology, a science that considers the universe as a whole and seeks to answer profound questions such as: How did it all begin? What will be our fate? What is the universe made of? Overall, cosmology seeks to unravel the profound mysteries of existence. Although it is highly theoretical, it is predominantly grounded in observational evidence.

2.1 The cosmological principle

The cosmological principle, also known as the Copernican principle, is a cornerstone of cosmology, essential for constructing the universe's metric as we will see further on. While matter is unevenly distributed on small scales, such as within our solar system or a galaxy, this irregularity doesn't hold true on larger scales exceeding 100 Mpc. Instead, the universe appears more uniform. Furthermore, analysis of the CMB temperatures indicates that the universe is isotropic around all points on these scales, denoting the absence of a preferred center, a concept that inherently implies homogeneity [44]. Hence, assuming homogeneity and isotropy for the universe on large scales is justified. These two characteristics collectively constitute the cosmological principle. One particularly intriguing aspect of this principle is its assurance that observations made from our single vantage point are representative of the universe as a whole. Consequently, these observations can legitimately serve as a basis for testing cosmological models [45].

An extension of the cosmological principle, the perfect cosmological principle, posits that isotropy and homogeneity extend not only through space but also across time [46]. However, this notion implies a static universe, contradicting the dynamic reality revealed by the Big Bang theory, among other evidence. Conse-

quently, the perfect cosmological principle is rejected.

2.2 Hubble's Law

The first serious cosmological models emerged following Einstein's theory of General Relativity. Initially, Einstein proposed a static universe and introduced the cosmological constant (Λ) to counteract gravitational collapse. However, shortly thereafter, Friedmann and then Lemaître proposed the idea of an evolving universe, specifically one undergoing expansion. What fundamentally altered our perception of the universe's structure and dynamics was Hubble's Law. This law provided compelling evidence for an expanding universe and laid the groundwork for the modern field of observational cosmology.

Hubble studied the motion of galaxies in the universe using the Doppler effect. In 1929, he observed that the spectra of the vast majority of galaxies were redshifted, indicating that these galaxies were receding from us [47]. Furthermore, he found that the further away a galaxy is, the greater its redshift. This implies that the relation between a galaxy's velocity and its distance from Earth is linear.

$$\vec{u} = H\vec{d}, \quad (2.1)$$

where H is the Hubble parameter, a quantity that represents the expansion rate of the universe. The value of this parameter today is known as the Hubble constant and is denoted as H_0 . It is commonly expressed as [48]

$$H_0 = 100h \text{ km s}^{-1} \text{ Mpc}^{-1}. \quad (2.2)$$

This notation arises because the Hubble parameter is determined through observations, and its value varies depending on the method used for measurement and the time at which the measurement is taken [49]. Thus, it provides a convenient and practical way to express the Hubble constant, facilitating the handling of uncertainties and standardization across various studies and theoretical models.

It is important to note that in our Galaxy, there is generally an equal number of stars displaying blueshifted and redshifted spectra. This balance occurs because the Milky Way is neither contracting nor expanding. The shifts in the spectral lines of stars are solely due to the Doppler effect caused by their peculiar motions [46]. Hubble's Law is observed only on large scales because, on smaller scales, the motion of objects is dominated by inhomogeneities in the gravitational field. These inhomogeneities lead to phenomena such as virial orbital motions. Also,

in such scales, objects held together by other, stronger forces resist the Hubble expansion. For instance, atoms, molecules, and solid objects are bound by electromagnetic forces, which are significantly stronger than the expansive force due to the universe's expansion. Therefore, on the scales of atoms, molecules, and even macroscopic objects like planets and stars, electromagnetic forces maintain their integrity against the Hubble expansion.

2.3 FLRW cosmology

As previously mentioned, we will rely on the cosmological principle to construct the metric of the universe¹. According to this principle, spacelike coordinates must be homogeneous and isotropic; therefore, the spatial component needs to be maximally symmetric. The most general metric that possesses the necessary symmetries is the Friedmann-Lemaître-Riemann-Walker (FLRW) metric $g_{\mu\nu}$ with line element (for a detailed proof, see [44])

$$ds^2 = g_{\mu\nu} dx^\mu dx^\nu = dt^2 - a^2(t) \left[\frac{dr^2}{1 - kr^2} + r^2 (d\theta^2 + \sin^2\theta d\phi^2) \right] \quad (2.3)$$

where k is the spatial curvature and takes the values -1, 0, and +1 corresponding to an open, flat, and closed universe respectively. The function $a(t)$ represents the scale factor, which explicitly illustrates the dependence of the universe's expansion on time. Its present value is normalized to $a_0 = 1$, rendering it dimensionless and simplifying the comparison of the universe's size at different times. Also, the coordinates (r, θ, ϕ) are comoving coordinates, implying that an observer at rest in these coordinates remains at rest. Given the strong evidence supporting the spatial flatness of the universe [50], we will assume $k = 0$ throughout this thesis, unless otherwise specified. Thus, the line element becomes

$$ds^2 = dt^2 - a^2(t) [dr^2 + r^2 (d\theta^2 + \sin^2\theta d\phi^2)] . \quad (2.4)$$

The exact form of the scale factor is derived by solving Einstein's field equations. This form is highly dependent on the density distribution of the universe. Therefore, it is essential to discuss the energy-momentum tensor $T_{\mu\nu}$, which encapsulates the density and flux of energy and momentum in spacetime, playing a crucial role in determining the scale factor.

¹Actually, the cosmological principle alone is insufficient. We also employ Weyl's postulate [44], which will be discussed later.

Weyl's postulate states that galaxies in the universe behave like particles in a perfect fluid, characterized by energy density ρ and pressure p . Apart from the bulk motion of the fluid, represented by the 4-vector velocity u^μ , the relative movement of the particles must be negligible. Although this postulate does not perfectly apply to galaxies, the deviation is remarkably small; hence, the energy-momentum tensor can be approximated as that of a perfect fluid [48, 49]. In a generally curved spacetime, the simplest form of this tensor is expressed as [44]

$$T_{\mu\nu} = (\rho + p) u_\mu u_\nu - p g_{\mu\nu}. \quad (2.5)$$

For simplicity, we will use the fluid's instantaneous rest frame (IRF), in which the 4-velocity has only a time component, i.e., $[u_\mu] = (1, 0, 0, 0)$. Due to the homogeneity and isotropy of the universe, the energy density and pressure of the fluid depend solely on cosmic time. These two quantities are related by the equation of state (EoS)

$$p = w\rho, \quad (2.6)$$

where w is the EoS parameter and varies based on the fluid being described. For a non-relativistic perfect fluid, $w = 0$, while for a relativistic perfect fluid, $w = \frac{1}{3}$. For barotropic fluids, the EoS parameter is independent of time; however, this time-independence is not a requirement for all types of fluids, as will be discussed later.

2.4 Friedmann equations

The most effective gravitational theory available to date is Einstein's theory of General Relativity. Consequently, the equations that govern the evolution of the universe must be derived from the field equations of this theory.

The well-known Einstein field equations relate the curvature of spacetime to the energy and momentum of matter and radiation present. These equations are given by (for a proof, see Appendix A.1)

$$R_{\mu\nu} - \frac{1}{2} g_{\mu\nu} R = -\kappa^2 T_{\mu\nu}. \quad (2.7)$$

$R_{\mu\nu}$ is the Ricci tensor, which is a contraction of the Riemann curvature tensor and describes how volume changes along geodesics. The term $R \equiv g^{\mu\nu} R_{\mu\nu}$, known as the Ricci scalar, provides an overall measure of curvature at a point. Both of these quantities describe the geometric properties of spacetime and its interaction

with matter and energy. Lastly, $\kappa = \sqrt{8\pi G}$ represents the inverse of the reduced Planck mass.

By employing the FLRW metric in equation (2.7), the renowned Friedmann equations are derived (for a proof, see Appendix A.2). From the (00)-component, is obtained the first Friedmann equation

$$\frac{\dot{a}^2}{a^2} = \frac{\kappa^2}{3} \rho, \quad (2.8)$$

where the dot denotes derivative with respect to time. On the other hand, the (ii)-component yields the second Friedmann equation

$$2 \frac{\ddot{a}}{a} + \frac{\dot{a}^2}{a^2} = -\kappa^2 p. \quad (2.9)$$

A combination of (2.8) and (2.9) gives rise to the acceleration equation

$$\frac{\ddot{a}}{a} = -\frac{\kappa^2}{6} (\rho + 3p). \quad (2.10)$$

Equations (2.8) and (2.10) govern the dynamical evolution of the universe by providing a solution for the scale factor $a(t)$. To fully solve these equations, it is imperative to also consider the conservation of energy equation, known as the continuity equation

$$\dot{\rho} + 3 \frac{\dot{a}}{a} (\rho + p) = 0. \quad (2.11)$$

By substituting equation (2.6) into equation (2.11), it is straightforward to determine the function $\rho(a)$. Specifically, after performing a basic integration, it is found that

$$\rho = \rho_0 a^{-3(1+w)}, \quad (2.12)$$

which is valid for $w \neq -1$ and ρ_0 is an integration constant. As mentioned earlier, for a radiation dominated universe, $w = \frac{1}{3}$, and therefore

$$\rho_r = \rho_{0r} a^{-4}, \quad (2.13)$$

while for a dust-like era, $w = 0$, and we have

$$\rho_m = \rho_{0m} a^{-3} \quad (2.14)$$

Both cases correspond to a decelerated expansion of the universe.

As discussed in Section 2.2, the universe is accelerating. From equation (2.10), it can be concluded that an accelerating expansion occurs when the EoS parameter takes values $w < -\frac{1}{3}$. This condition results in a repulsive effect due to the negative pressure, which counteracts gravitational attraction and leads to the acceleration of the universe's expansion. Since this condition cannot be satisfied by any known form of matter, it necessitates the introduction of a new form of energy. This exotic form of energy, known as “dark energy”, is a hypothetical entity characterized by an EoS parameter that meets this criterion.

Finally, it is essential to establish the concept of the energy density parameter Ω . The total energy density at which spacetime is flat is referred to as the critical energy density [51]. From equation (2.8), it is defined as [44, 45, 49]

$$\rho_{crit} \equiv \frac{3H^2}{\kappa^2}, \quad (2.15)$$

where H is the Hubble parameter, defined as $H \equiv \frac{\dot{a}}{a}$. The dimensionless ratio of the energy density of a specific component to the critical density is termed the energy density parameter of that component, and it is given by [44, 45]

$$\Omega_i(t) \equiv \frac{\rho_i(t)}{\rho_{crit}(t)}. \quad (2.16)$$

The total energy density parameter is the sum of the energy density parameters of all components in the universe, and it equals 1. This is expressed as

$$\Omega_{tot} = \sum_i^N \Omega_i = 1. \quad (2.17)$$

2.5 Dark energy

As mentioned, there exists an accelerated expansion of the universe, which cannot be explained solely by matter and radiation; hence, the concept of “dark energy” must be introduced. The exact nature of dark energy is unknown, as it can only be detected indirectly through its effects on cosmic expansion [51]. According to the latest data [50], it is currently the dominant component of the universe, comprising almost 70% of the total mass-energy.

The most widely accepted model of dark energy is the concept of vacuum energy, which constitutes the foundation of the standard cosmological model, commonly referred to as the Λ CDM model. According to quantum field theory, the vacuum is defined as the state of lowest possible energy, containing virtual particles that are continually created and rapidly annihilated. As the universe expands, this lowest possible vacuum energy density remains constant rather than decreasing [51]. Taking into consideration equation (2.11), it is evident that $w = -1$ for the case of the cosmological constant Λ .

The observational data of EoS parameter provide limited information regarding the temporal evolution of w . Consequently, it is plausible to consider scenarios where the equation of state of dark energy varies over time. Such cases include a time-evolving scalar field, with many proposed models such as quintessence, phantoms, K-essence, tachyon, ghost condensates, and dilatonic dark energy, among others [52, 53]. The models of quintessence and phantom fields will be discussed in more detail later on.

Another model of dark energy involves Chaplygin gases and their generalizations. These models form a class of simple cosmological theories based on the use of peculiar perfect fluids [54, 55].

2.6 Alternatives to dark energy

Dark energy is the strongest candidate for the accelerated expansion of the universe, but it is not the only one. Other potential explanations include modified gravity theories [56–59], the Lemaître-Tolman-Bondi (LTB) model [60], cosmic backreaction [61], string theory [62], and others. However, these alternatives are beyond the scope of this thesis and will not be discussed further.

Chapter 3

Observational Cosmology

Observations are the cornerstone of modern cosmology, providing critical insights into the structure, composition, and evolution of the universe. By leveraging various astrophysical phenomena as tools, we can probe vast cosmic distances and explore fundamental parameters of the universe. This chapter delves into the methodologies and principles behind these observations, highlighting their significance in shaping our understanding of the cosmos.

3.1 Cosmic distance ladder

Astronomers employ a variety of methods to measure relative distances in the universe, tailored to the specific characteristics of the objects being observed. These methods collectively form what is known as the cosmic distance ladder. The term “ladder” reflects the hierarchical nature of this approach, where each successive technique builds upon the calibration provided by the preceding one.

3.1.1 Parallax

The parallax method relies on basic geometric principles. When a nearby object is observed from two different positions, it appears to shift relative to the background of more distant objects [63]. By measuring this apparent shift, known as the parallax angle, and knowing the distance between the two observation points along Earth’s orbit, the distance to the nearby star can be accurately calculated. However, this method is only effective when the parallax angle is sufficiently large to be measurable, which restricts its application to relatively nearby objects [46].

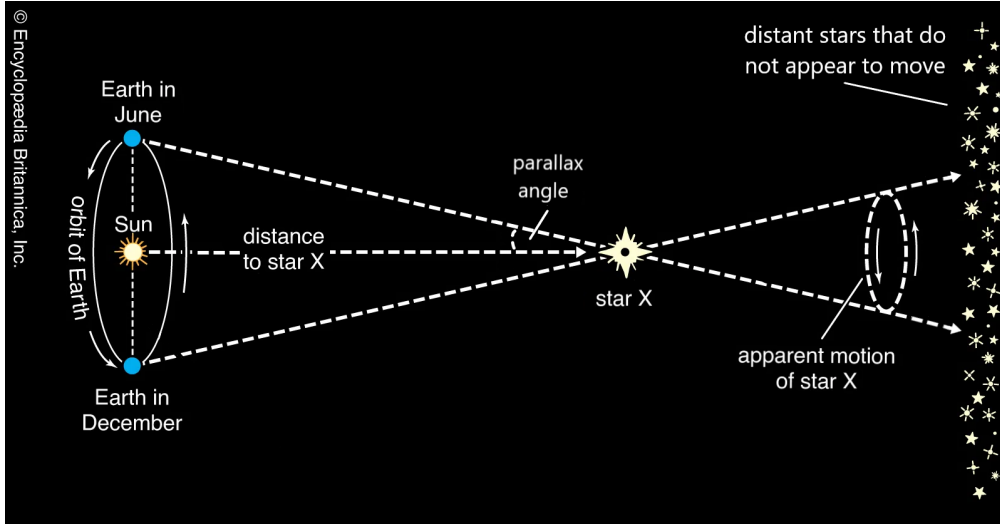


Figure 3.1: Stellar parallax.

3.1.2 Cepheids

Naturally, the need for distance measurements extends well beyond the 100–200 pc limit of the parallax method. To measure greater distances, astronomers rely on Cepheid variables—pulsating stars whose luminosity varies periodically over time. Empirically, it was found that the absolute magnitude¹ of a Cepheid variable is related to its pulsation period through a relation of the form [63]

$$M_v = a + b \log P, \quad (3.1)$$

where M_v is the absolute magnitude of the star, P is the pulsation period, and a , b are constants determined empirically. However, observationally, we measure the apparent magnitude of a star, not its absolute magnitude. To use this equation, we must first determine the constants a and b by studying nearby Cepheids for which distances can be determined using the parallax method. Once these constants are calibrated, the process becomes straightforward: for more distant Cepheids, we measure their pulsation periods and use the period-luminosity relation (3.1) to calculate their absolute magnitudes. Knowing the absolute magnitude, M_v , and measuring the apparent magnitude, m , we can calculate the distance to the star using the distance modulus relation,

$$\mu \equiv m - M = 5 \log d_L + 25, \quad (3.2)$$

where d_L is the luminosity distance in Mpc. This method provides a powerful tool for determining distances to nearby galaxies (up to ~ 25 Mpc [46]).

¹The apparent magnitude represents how bright a star appears from Earth, while the absolute magnitude describes how bright it would appear if located at a standard distance of 10 pc.

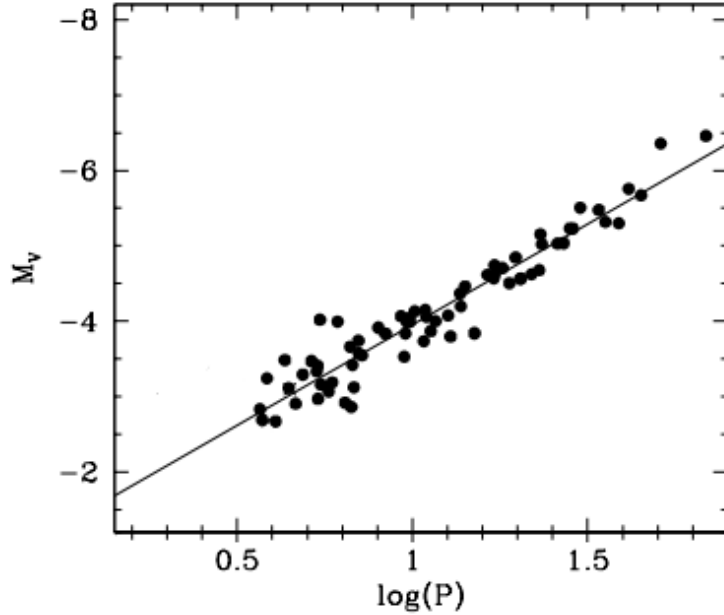


Figure 3.2: The period-luminosity relation for Milky Way Cepheids [64].

3.1.3 Type Ia Supernovae (SNIa)

Initially, the parallax method allowed us to measure distances only to nearby stars, well within our galaxy. With Cepheids, we extended our reach to nearby galaxies, but even this is not sufficient for our needs. To probe even greater distances, we turn to Type Ia supernovae.

SNIa originate from white dwarfs in binary star systems, where the white dwarf accretes mass from its companion star. When the mass of the white dwarf exceeds the Chandrasekhar limit, it undergoes a catastrophic explosion, leaving behind a collapsed remnant. This explosion can make the supernova temporarily brighter than an entire galaxy, rendering them visible over vast cosmic distances.

Unfortunately, not every SNIa exhibits the same maximum apparent magnitude. However, Phillips [66], through observations of SNIa in galaxies with known distances, identified a correlation between their peak absolute magnitudes and the rate at which their brightness declines after maximum light. This relationship,

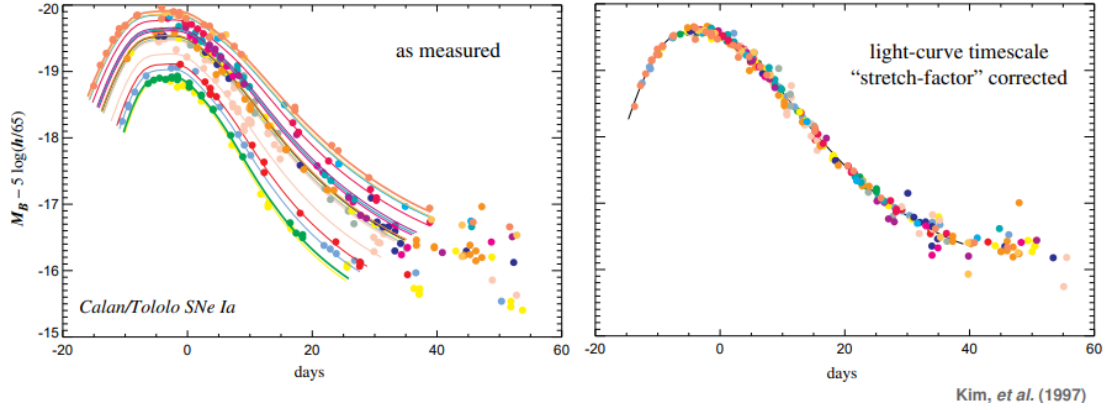


Figure 3.3: Light curves of various SNIa before (left) and after (right) calibration [65].

now known as the Phillips relation, can be expressed as

$$M_{max}(B) = -21.726 + 2.698 \Delta m_{15}(B) \quad (3.3)$$

where M_{max} is the maximum absolute magnitude of the SNIa, and Δm_{15} represents the change in apparent magnitude between the peak and 15 days afterward. The Phillips relation is critically important because it allows for the precise determination of the absolute magnitude of a SNIa. Using this value and the distance modulus relation (3.2), the luminosity distance to the supernova can be accurately calculated, making SNIa reliable standard candles for measuring cosmological distances.

The term “cosmic distance ladder” is now evidently justified. The process begins with the parallax method, which measures distances to nearby stars. These measured distances are then used to calibrate Cepheid variables, allowing for distance measurements to nearby galaxies. Subsequently, the distances determined using Cepheids are employed to calibrate Type Ia supernovae. Once SNIa are calibrated, they enable measurements to distances of up to ~ 1000 Mpc, significantly extending the reach of our cosmic measurements.

3.2 Baryonic Acoustic Oscillations (BAO)

The early universe was a hot, dense plasma where photons, electrons, and protons were tightly coupled, forming a single photon-baryon fluid through Thomson scat-

tering². In contrast, non-baryonic dark matter, which interacts only gravitationally, began forming structures at the epoch of matter-radiation equality. Since the density of dark matter was approximately three times that of the photon-baryon fluid at that time, the latter evolved under the gravitational influence of the dark matter potential wells. Small fluctuations in the dark matter density led to variations in the gravitational potential, creating regions where the photon-baryon fluid would fall inward. As the fluid compressed, its energy density increased, leading to a rise in radiation pressure, which eventually counteracted gravitational collapse and caused the fluid to expand outward. However, as the expanding shell of the fluid moved farther from the initial perturbation, its pressure decreased, allowing gravity to pull it back inward. This process repeated cyclically, with gravity and radiation pressure acting in opposition, setting up acoustic oscillations in the plasma. These oscillations propagated outward as a spherical sound wave at the speed of sound, c_s [68, 69].

The photon-baryon oscillations begin to dampen at the epoch of decoupling (z_{dec}) as photons start to stream freely and radiation pressure weakens [69]. However, the final imprint of the sound wave is preserved at the drag epoch (z_d), when baryons fully decouple from photons. Since the photon density is significantly higher than the baryon density, photons decouple (i.e., stop noticing the baryons) earlier, effectively ceasing their interaction with baryons. However, baryons continue to experience the influence of photons for a brief period before fully decoupling. This delay between photon and baryon decoupling is commonly referred to as “baryon drag” [70]. The redshift corresponding to this epoch, known as the drag redshift z_d , is given by [71, 72]

$$z_d = 1291 \frac{\omega_m^{0.251}}{1 + 0.659 \omega_m^{0.828}} [1 + b_1 \omega_b^{b_2}], \quad (3.4)$$

where $\omega_m \equiv \Omega_{0m} h^2$ is the matter density parameter combination, and $\omega_b \equiv \Omega_{0b} h^2$ is the baryon density parameter combination. The factors b_1 and b_2 are defined as

$$b_1 = 0.313 \omega_m^{-0.419} [1 + 0.607 \omega_m^{0.674}] \quad (3.5)$$

$$b_2 = 0.238 \omega_m^{0.223}. \quad (3.6)$$

The BAO scale is set by the radius of the sound horizon at the drag redshift z_d . The comoving sound horizon at a redshift z is given by [72]

$$r_s(z) = \int_z^\infty \frac{c_s(z')}{H(z')} dz' \quad (3.7)$$

²While protons also interact with free-streaming photons through Thomson scattering, the corresponding cross-section is so small that these interactions can be neglected. Instead, it is the Coulomb interaction with electrons that maintains thermal equilibrium between protons, electrons, and photons [67].

where the speed of sound in the photon-baryon plasma is given by [71, 73]

$$c_s = \frac{1}{\sqrt{3(1 + R_s)}} \quad (3.8)$$

with R representing the ratio of the baryon to photon momentum density, defined as

$$R_s \equiv \frac{3\rho_b}{4\rho_\gamma} = \frac{3\Omega_{0b}}{4\Omega_{0r}} \frac{1}{1+z} \quad (3.9)$$

In practice, BAO data are analyzed within the framework of a fiducial cosmology, using the sound horizon at the drag epoch as a reference scale. An anisotropic BAO analysis enables the independent measurement of the BAO scale along two distinct directions: parallel and perpendicular to the line of sight. This approach allows for simultaneous constraints on both the Hubble parameter $H(z)$ and the comoving angular diameter distance $D_M(z)$, given by

$$D_M(z) = \int_0^z H^{-1}(z') dz' \quad (3.10)$$

In some cases, the constrained quantity is the volume-averaged distance, defined as [74]

$$D_V(z) = [z D_H(z) D_M^2(z)]^{1/3} \quad (3.11)$$

where $D_H(z) = 1/H(z)$ is the Hubble distance. However, since variations in cosmological parameters can alter the sound horizon r_s , BAO measurements do not directly constrain the individual parameters above. Instead, they provide constraints on specific parameter combinations that include the fiducial sound horizon at the drag epoch, $r_d^{fid} = 147.49$ Mpc [72],

$$D_M(z) \times \frac{r_d^{fid}}{r_d}, \quad D_H(z) \times \frac{r_d^{fid}}{r_d}, \quad D_V(z) \times \frac{r_d^{fid}}{r_d}$$

where $r_d = r_s(z_d)$ denotes the sound horizon at the drag epoch.

3.3 Cosmic Microwave Background (CMB)

The CMB is a faint, nearly uniform radiation that permeates the universe. It originates from the epoch when the universe transitioned from an opaque plasma to a transparent state, approximately 375,000 years after the Big Bang, providing the first-ever snapshot of the universe. While these photons were not in the microwave range when they began their journey, the expansion of the universe redshifted them to their current microwave wavelengths by the time they reached us [48].

Importantly, the CMB is not perfectly uniform. Its slight anisotropies contain a wealth of information, allowing us to derive key insights into the universe's composition, geometry, and early evolution.

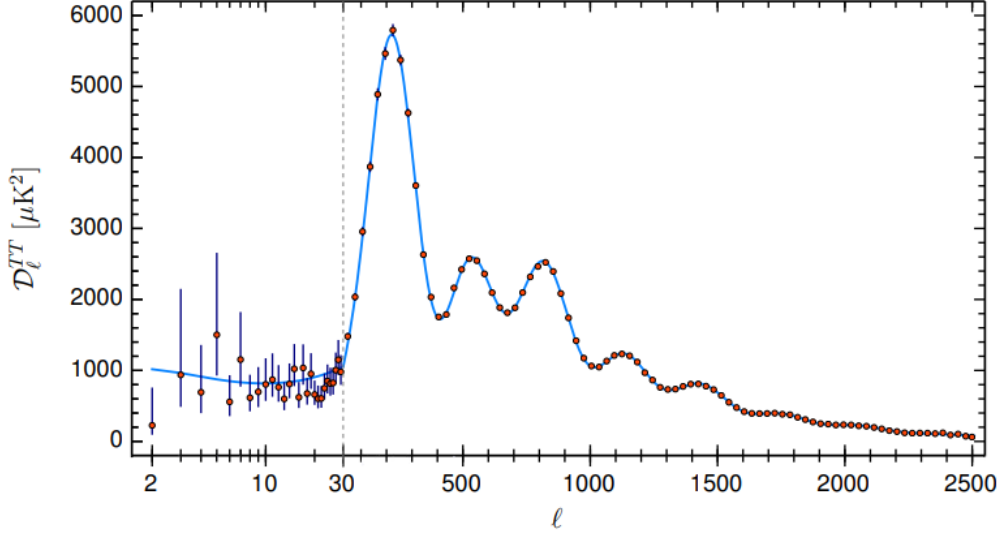


Figure 3.4: The temperature power spectrum of CMB. The light-blue curve represents the theoretical predictions of the Λ CDM model [75].

The largest anisotropy observed in the CMB is the dipole ($\ell = 1$), which arises due to the Doppler effect caused by Earth's motion relative to the CMB. Since the dipole does not provide information about the intrinsic properties of the CMB, studies typically begin at the quadrupole ($\ell = 2$) [48, 76]. Different ranges of ℓ provide distinct insights into the universe. For $\ell \lesssim 100$, the anisotropies primarily reflect the intrinsic inhomogeneities in the distribution of matter. The range $100 \lesssim \ell \lesssim 1000$ corresponds to the acoustic peaks, which are a result of acoustic oscillations in the photon-baryon plasma before recombination. Lastly, at $\ell \gtrsim 1000$, we observe the damping tail, which arises because the recombination process was not instantaneous, leading to a smoothing of small-scale anisotropies [76].

When constraining dark energy parameters, an efficient summary of the CMB data is provided by the shift parameters

$$R \equiv \sqrt{\Omega_m H_0^2} r(z_{dec}) \quad (3.12)$$

$$\ell_A \equiv \frac{\pi r(z_{dec})}{r_s(z_{dec})} \quad (3.13)$$

along with the baryon density parameter combination ω_b [77]. Here, $r(z_{dec})$ represents the comoving distance to the photon-decoupling surface, while $r_s(z_{dec})$ is the comoving sound horizon at photon-decoupling epoch. The parameter ℓ_A , which corresponds to the angular scale of the sound horizon at last scattering, determines the position of the first acoustic peak in the CMB power spectrum.

The redshift at which photons decouple from matter, commonly referred to as the decoupling redshift, can be approximated as [5, 73]

$$z_{dec} = 1048 \left[1 + 0.00124 \omega_b^{-0.738} \right] \left[1 + g_1 \omega_m^{g_2} \right] \quad (3.14)$$

The factors g_1 and g_2 are defined as

$$g_1 = \frac{0.0783 \omega_b^{-0.238}}{1 + 39.5 \omega_b^{0.763}} \quad (3.15)$$

$$g_2 = \frac{0.560}{1 + 21.1 \omega_b^{1.81}}. \quad (3.16)$$

3.4 The χ^2 function

A cosmological model is meaningful only when its predictions are compared with observational data. This comparison is typically performed using the χ^2 function, which, in the case of independent measurements, is defined as

$$\chi^2(k) = \sum_{i=1}^N \frac{[X_{th}(z_i, k) - X_{i,obs}]^2}{\sigma_i^2}. \quad (3.17)$$

This function quantifies the discrepancy between the theoretical predictions of the model, $X_{th}(k)$, and the corresponding observed values, $X_{i,obs}$, at a given redshift z_i . Here, σ_i represents the standard deviation of the observed data at each redshift. The smaller the value of χ^2 , the better the fit of the model to the observational data and, consequently, the more robust the model. When multiple datasets are involved, the total χ^2 is typically used. For instance, if data from the CMB, BAO, and Pantheon+ surveys are available, the total χ^2 is given by the sum of the individual χ^2 values, i.e., $\chi_{tot}^2 = \chi_{CMB}^2 + \chi_{BAO}^2 + \chi_{Panth}^2$.

A detailed theoretical background on statistical methods will not be provided here. However, interested readers are encouraged to refer to [73] and [78] for a

comprehensive discussion of the relevant methodologies.

In practice, the datasets we analyze do not consist of independent measurements. Therefore, a more general definition of the χ^2 function is required. In this case, it takes the form

$$\chi^2(k) = [X_{th}(k) - X_{i,obs}]^T \cdot V^{-1} \cdot [X_{th}(k) - X_{i,obs}] \quad (3.18)$$

where V is the covariance matrix, which accounts for correlations between different data points.

3.4.1 SNIa

For SNIa, the dataset used in this analysis is Pantheon+. A detailed description of the Pantheon+ sample, including the interpretation of each column, can be found in [37]. The residual for each supernova, denoted as $V_{SN,i}$, is defined as

$$V_{SN,i} = m_B(z_i) - M - \mu_{th}(z_i) \quad (3.19)$$

where $m_B(z_i) - M$ represents the distance modulus for the i^{th} supernova, and $\mu_{th}(z_i)$ is the distance modulus predicted by the theoretical model. As seen in equation (3.2), the distance modulus is given by $\mu = 5 \log d_L + 25$ where d_L is the luminosity distance, expressed as

$$d_L = (1 + z) \int_0^z \frac{dz'}{H(z')} \quad (3.20)$$

The χ^2 statistic for SNIa is then computed as

$$\chi_{SN}^2 = V_{SN}^T \cdot C_{tot}^{-1} \cdot V_{SN} \quad (3.21)$$

where C_{tot} is the total covariance matrix, defined as the sum of the statistical and systematic covariance matrices

$$C_{tot} = C_{stat} + C_{syst}. \quad (3.22)$$

3.4.2 BAO

6dFGS & WiggleZ

These surveys measure the distilled parameter d_z , defined as

$$d_z \equiv \frac{r_d}{D_V(z)}. \quad (3.23)$$

The parameter vector for the 6dF Galaxy Survey (6dFGS) and WiggleZ surveys is given by

$$v_{6d,Wig} = \begin{pmatrix} z \\ d_z \\ \sigma_{d_z} \end{pmatrix} \quad (3.24)$$

Thus, the residual vector is defined as

$$V_{6d,Wig} = v_{th} - v_{obs} = \begin{pmatrix} z - z^{obs} \\ d_z - d_z^{obs} \\ \sigma_{d_z} - \sigma_{d_z}^{obs} \end{pmatrix} \quad (3.25)$$

The χ^2 statistic for these datasets is then computed as

$$\chi_{6d,Wig}^2 = V_{6d,Wig}^T \cdot C^{-1} \cdot V_{6d,Wig} \quad (3.26)$$

where C represents the covariance matrix associated with the BAO measurements from these surveys.

SDSS

Through the Sloan Digital Sky Survey (SDSS), we obtain the measurement

$$D_M(z) \times \frac{r_d^{fid}}{r_d} \quad (3.27)$$

Thus, the corresponding data vector is given by

$$V_{SDSS} = \begin{pmatrix} z \\ \frac{D_V}{r_d} \\ \sigma \end{pmatrix} = \begin{pmatrix} z \\ \frac{1}{d_z} \\ \sigma \end{pmatrix} \quad (3.28)$$

In this case, since the measurements are independent, the χ^2 function takes the standard form

$$\chi_{SDSS}^2 = \sum_i \frac{\left[\frac{1}{d_z(z_i)} - \left(\frac{D_V}{r_d} \right)_{i,obs} \right]^2}{\sigma_i^2} \quad (3.29)$$

Ly- α

In this case, we obtain two distinct measurements, $\frac{D_M}{r_d}$ and $\frac{D_H}{r_d}$. Therefore, the corresponding data vectors are given by

$$v_1 = \begin{pmatrix} z \\ \frac{D_M}{r_d} \\ \sigma \end{pmatrix} \quad \text{and} \quad v_2 = \begin{pmatrix} z \\ \frac{D_H}{r_d} \\ \sigma \end{pmatrix} \quad (3.30)$$

However, in some cases, the proper angular diameter distance d_A is used instead of the comoving angular diameter distance D_M . These two distances are related through the expression $D_M = (1+z)d_A$. In the case of the Ly- α , the data vector used is defined as [73]

$$V_{Ly-\alpha} = \begin{pmatrix} \frac{d_A}{r_d} - \left(\frac{d_A}{r_d}\right)_{th} \\ \frac{D_H}{r_d} - \left(\frac{D_H}{r_d}\right)_{th} \end{pmatrix} \quad (3.31)$$

The χ^2 function for this dataset is then computed as

$$\chi_{Ly-\alpha}^2 = V_{Ly-\alpha}^T \cdot C^{-1} \cdot V_{Ly-\alpha}. \quad (3.32)$$

Thus, the total χ^2 function for the BAO data is given by

$$\chi_{BAO}^2 = \chi_{6d,Wig}^2 + \chi_{SDSS}^2 + \chi_{Ly-\alpha}^2. \quad (3.33)$$

3.4.3 CMB

As mentioned in Section 3.3, the parameters R , ℓ_A and ω_B provide an efficient summary of the CMB data. Therefore, these are the quantities utilized in the analysis. The parameter vector for the CMB is defined as

$$v_{CMB} = \begin{pmatrix} R \\ \ell_A \\ \omega_B \end{pmatrix} \quad (3.34)$$

Thus, the residual vector is given by

$$V_{CMB} = v_{th} - v_{obs} = \begin{pmatrix} R - \langle R \rangle \\ \ell_A - \langle \ell_A \rangle \\ \omega_B - \langle \omega_B \rangle \end{pmatrix} \quad (3.35)$$

The χ^2 statistic for the CMB is then computed as

$$\chi_{CMB}^2 = V_{CMB}^T \cdot C_{CMB}^{-1} \cdot V_{CMB} \quad (3.36)$$

where C_{CMB} is the covariance matrix associated with the CMB data.

Chapter 4

Scalar Fields

This chapter aims to provide all the necessary information about the quintessence fields, which will be the focus of the next chapter, and the phantom fields, which will be discussed in the final chapter of this thesis.

4.1 Quintessence fields

Quintessence is a theoretical concept in cosmology that describes a canonical scalar field ϕ which is minimally coupled to gravity¹. Unlike the cosmological constant, which has a constant energy density, quintessence has a dynamic energy density and pressure that evolve over time. Each quintessence model is distinguished by the specific form of the self-interacting potential $V(\phi)$ that is chosen. This potential can take various forms, such as exponential, power-law, or other complex functions, and these forms determine the behavior and evolution of the quintessence field.

The Lagrangian density of a scalar field is [53]

$$\mathcal{L}_\phi = \frac{\epsilon}{2} g^{\mu\nu} \partial_\mu \phi \partial_\nu \phi - V(\phi) \quad (4.1)$$

where $\epsilon = +1$ for quintessence fields and $\epsilon = -1$ for phantom fields, which will be discussed later on in this chapter.

¹The scalar field interacts with gravity exclusively through the metric, whereas in the non-minimal case, the field interacts directly with the curvature of spacetime.

The action of the theory is given by

$$S = S_{EH} + S_\phi + S_m = \frac{1}{2\kappa^2} \int d^4x \sqrt{-g} R + \int d^4x \sqrt{-g} \left(\frac{\epsilon}{2} g^{\mu\nu} \partial_\mu \phi \partial_\nu \phi - V(\phi) \right) + S_m. \quad (4.2)$$

It is important to understand that the scalar field ϕ is distinct from the matter fields included in S_m . By following the same procedure as we did to derive equation (A.16), we obtain

$$R_{\mu\nu} - \frac{1}{2} g_{\mu\nu} R = -\kappa^2 \frac{2}{\sqrt{-g}} \frac{\delta \mathcal{L}_m}{\delta g^{\mu\nu}} - \kappa^2 \frac{2}{\sqrt{-g}} \frac{\delta \mathcal{L}_\phi}{\delta g^{\mu\nu}}. \quad (4.3)$$

Inserting equation (A.17) and defining the energy-momentum tensor of the scalar field as

$$T_{\mu\nu}^{(\phi)} \equiv \frac{2}{\sqrt{-g}} \frac{\delta \mathcal{L}_\phi}{\delta g^{\mu\nu}} \quad (4.4)$$

yields,

$$R_{\mu\nu} - \frac{1}{2} g_{\mu\nu} R = -\kappa^2 (T_{\mu\nu} + T_{\mu\nu}^{(\phi)}). \quad (4.5)$$

Taking into consideration equations (4.1) and (4.4), the form of the energy-momentum tensor can be easily derived as

$$T_{\mu\nu}^{(\phi)} = -\frac{\epsilon}{2} g_{\mu\nu} g^{\alpha\beta} \partial_\alpha \phi \partial_\beta \phi + g_{\mu\nu} V(\phi) + \epsilon \partial_\mu \phi \partial_\nu \phi. \quad (4.6)$$

It is possible to interpret the quintessence field as a perfect fluid. Therefore, the field's energy density and pressure are expressed as

$$\rho_\phi = T_{00}^{(\phi)} = -\frac{\epsilon}{2} g_{00} g^{\alpha\beta} \partial_\alpha \phi \partial_\beta \phi + g_{00} V(\phi) + \epsilon \partial_0 \phi \partial_0 \phi = \frac{\epsilon}{2} \dot{\phi}^2 + V(\phi) \quad (4.7)$$

$$p_\phi = -\frac{T_{ii}^{(\phi)}}{g_{ii}} = \frac{\epsilon}{2} g^{\alpha\beta} \partial_\alpha \phi \partial_\beta \phi - V(\phi) - \epsilon g^{ii} \partial_i \phi \partial_i \phi = \frac{\epsilon}{2} \dot{\phi}^2 - V(\phi) \quad (4.8)$$

respectively. In these expressions, we have used the fact that late-time acceleration requires a very light scalar field with an effective mass of the order of the Hubble parameter. The Compton wavelength of the field will be of the order of or larger than the Hubble scale, which implies that the field is expected to be spatially smooth within the Hubble scale, causing all spatial derivatives to vanish [79].

Varying the action (4.2) with respect to the scalar field ϕ gives the Klein-Gordon equation

$$\epsilon \partial_\mu \partial^\mu \phi + \frac{\partial V(\phi)}{\partial \phi} = 0. \quad (4.9)$$

Now considering the FLRW metric and the fact that $\partial_\mu \partial^\mu \phi = \frac{1}{\sqrt{|g|}} \partial_\alpha \left(\sqrt{|g|} g^{\alpha\beta} \partial_\beta \phi \right)$, equation (4.9) takes the form

$$\ddot{\phi} + 3 \frac{\dot{a}}{a} \dot{\phi} + \epsilon \frac{\partial V(\phi)}{\partial \phi} = 0 \xrightarrow{H=\frac{\dot{a}}{a}} \ddot{\phi} + 3H\dot{\phi} + \epsilon \frac{\partial V(\phi)}{\partial \phi} = 0, \quad (4.10)$$

which is the energy conservation equation of the scalar field at the background level [80]. The first term represents the acceleration of the field, the second term accounts for the damping effect due to cosmic expansion through the Hubble parameter H (Hubble friction), and the final term corresponds to the slope of the potential.

Now, the Friedmann equations take the form

$$\frac{\dot{a}^2}{a^2} = \frac{\kappa^2}{3} \left(\rho + \frac{\epsilon}{2} \dot{\phi}^2 + V(\phi) \right) \quad (4.11)$$

$$2 \frac{\ddot{a}}{a} + \frac{\dot{a}^2}{a^2} = -\kappa^2 \left(p + \frac{\epsilon}{2} \dot{\phi}^2 - V(\phi) \right) \quad (4.12)$$

$$\frac{\ddot{a}}{a} = -\frac{\kappa^2}{6} \left(3p + \rho + 2\epsilon \dot{\phi}^2 - 2V(\phi) \right) \quad (4.13)$$

and the EoS parameter of the scalar field becomes

$$w_\phi = \frac{p_\phi}{\rho_\phi} = \frac{\epsilon \dot{\phi}^2 - 2V(\phi)}{\epsilon \dot{\phi}^2 + 2V(\phi)} \xrightarrow{\text{quintessence}} \frac{\dot{\phi}^2 - 2V(\phi)}{\dot{\phi}^2 + 2V(\phi)} \quad (4.14)$$

It is noticeable that when the kinetic term $\dot{\phi}^2$ dominates, the EoS parameter for the scalar field ϕ takes the value $w_\phi = 1$, causing the field to behave like a stiff fluid. Conversely, when the potential term $2V(\phi)$ is predominant, the EoS parameter approaches $w_\phi = -1$, and the field starts to behave like a cosmological constant. Consequently, the EoS parameter for the scalar field can vary within the range $[-1, 1]$.

If we consider the late-time universe, where the contribution of the barotropic fluid can be neglected, equation (4.13) simplifies to

$$\frac{\ddot{a}}{a} = -\frac{\kappa^2}{3} \left(\dot{\phi}^2 - V(\phi) \right), \quad (4.15)$$

from which becomes evident that accelerated expansion ($\ddot{a} > 0$) occurs when $\dot{\phi}^2 < V(\phi)$, indicating that the potential energy must dominate over the kinetic energy. This implies that a sufficiently flat potential is necessary to achieve the required conditions for accelerated expansion [53].

4.2 Phantom fields

In cosmology, phantom fields are non-canonical² scalar fields minimally coupled to gravity. Unlike quintessence, they violate the dominant energy condition ($\rho_\phi + p_\phi > 0$), resulting in an EoS parameter $w_\phi < -1$. This violation implies that the energy density of the phantom field increases as the universe expands, which is in stark contrast to the behavior of typical matter and energy and potentially makes them physically unstable. However, current observational data appears to be consistent with the existence of a phantom field [81].

In this case, the Klein-Gordon equation (4.10) takes the form

$$\ddot{\phi} + 3H\dot{\phi} - \frac{\partial V(\phi)}{\partial \phi} = 0, \quad (4.16)$$

indicating that the field will tend to run up, rather than down, a potential towards larger energy. This behavior is the opposite of what occurs with quintessence fields, which tend to move down the potential towards lower energy.

The EoS parameter for the phantom fields is

$$w_\phi = \frac{p_\phi}{\rho_\phi} = \frac{\epsilon\dot{\phi}^2 - 2V(\phi)}{\epsilon\dot{\phi}^2 + 2V(\phi)} \stackrel{\text{phantom}}{=} \frac{-\dot{\phi}^2 - 2V(\phi)}{-\dot{\phi}^2 + 2V(\phi)}. \quad (4.17)$$

It is obvious from this expression that w_ϕ of these type of fields can indeed be less than -1 . However, it is important to note that crossing the phantom divide line $w_\phi = -1$ in a continuous manner is not possible. This is because such a transition would necessitate a change in the sign of the kinetic term, which is inherently fixed in both quintessence and phantom field models [82]. In quintessence models, the kinetic term is positive, while in phantom models, it is negative.

Phantom fields are generally plagued by severe ultraviolet (UV) quantum instabilities. Due to the unbounded nature of the energy density of a phantom field from below, the vacuum becomes unstable, leading to the production of ghosts and normal positive-energy fields. Consequently, the fundamental origin and stability of phantom fields remain significant challenges for theoretical physics [53]. However, with an appropriate choice of potential, it is possible to mitigate or even eliminate these instabilities.

²In the sense that they have a negative sign in the kinetic term of the Lagrangian.

Finally, Table 4.1 summarizes all the Friedmann equations that we have derived thus far, which will be useful for the next chapters.

	Only Barotropic Fluid	Λ +Barotropic Fluid
1 st Friedmann eq.	$H^2 = \frac{\kappa^2}{3}\rho$	$H^2 = \frac{\kappa^2}{3}\rho + \frac{\Lambda}{3}$
2 nd Friedmann eq.	$2\dot{H} + 3H^2 = -\kappa^2 p$	$2\dot{H} + 3H^2 = -\kappa^2 p + \Lambda$
Acceleration eq.	$\dot{H} = -\frac{\kappa^2}{2}(\rho + p)$	$\dot{H} = -\frac{\kappa^2}{2}(\rho + p)$
EoS parameter	$w = \frac{p}{\rho}$	$w = \frac{p - \Lambda/\kappa^2}{\rho + \Lambda/\kappa^2}$
	Only Scalar Field	Scalar Field+Barotropic Fluid
1 st Friedmann eq.	$H^2 = \frac{\kappa^2}{3}\rho_\phi$	$H^2 = \frac{\kappa^2}{3}(\rho + \rho_\phi)$
2 nd Friedmann eq.	$2\dot{H} + 3H^2 = -\kappa^2 p_\phi$	$2\dot{H} + 3H^2 = -\kappa^2(p + p_\phi)$
Acceleration eq.	$\dot{H} = -\frac{\kappa^2}{2}(\rho_\phi + p_\phi)$	$\dot{H} = -\frac{\kappa^2}{2}(\rho + \rho_\phi + p + p_\phi)$
EoS parameter	$w_\phi = \frac{p_\phi}{\rho_\phi}$	$w = \frac{p + p_\phi}{\rho + \rho_\phi}$

Table 4.1: Summary of the Friedmann equations and the EoS parameter for different cosmological models.

Chapter 5

Dynamical Systems In Cosmology

This section aims to study different models of dark energy using the dynamical system method and discuss their viability as dark energy candidates.

5.1 Introduction

Solving the Einstein field equations analytically, even with cosmological assumptions, is frequently highly challenging due to their non-linear nature. However, in the context of cosmology, a qualitative insight is often sufficient to obtain an initial understanding and estimation of a cosmological model. Thus, employing dynamical systems theory is a suitable initial approach and widely adopted [53, 59, 83–86].

An acceptable cosmological model must have three key characteristics concerning its critical points. First, it must include unstable points that serve as early-time attractors, from which the universe evolves away. Second, it should have stable points that act as late-time attractors, towards which the universe evolves. These stable points typically correspond to the universe’s accelerated expansion phase, driven by dark energy or a cosmological constant, representing a future asymptotic state. Finally, the model must feature saddle points, which are intermediate stages in the universe’s evolution, neither initial nor final. These saddle points are significant for describing transitional epochs, such as the matter-dominated era, which is crucial for the formation of large-scale structures in the universe [87].

5.2 Λ CDM

Among the studied models of dark energy, the standard cosmological model, Λ CDM, is of paramount importance. In this model, Λ represents the cosmological constant, which denotes the energy of the vacuum, contributing to the accelerated expansion of the universe. The “CDM” stands for “Cold Dark Matter”, referring to non-baryonic, non-relativistic matter that interacts only with gravity and significantly exceeds the amount of visible baryonic matter [88–92]. This model provides a comprehensive framework that successfully explains a wide range of cosmological observations.

5.2.1 Dynamical analysis

To construct the dynamical system for the model, we consider the Friedmann equations, incorporating matter, radiation, and the cosmological constant. These equations are derived in Appendix A.2. By rearranging equation (A.28), we obtain

$$1 = \frac{\kappa^2}{3H^2} \rho_r + \frac{\kappa^2}{3H^2} \rho_m + \frac{\Lambda}{3H^2}. \quad (5.1)$$

From equation (A.30), with $w_r = \frac{1}{3}$ and $w_m = 0$, we derive

$$\dot{H} = -\frac{2\kappa^2}{3} \rho_r - \frac{\kappa^2}{2} \rho_m \xrightarrow[H \neq 0]{/(3H^2)} \frac{\dot{H}}{3H^2} = -\frac{2}{3} \frac{\kappa^2}{3H^2} \rho_r - \frac{1}{2} \frac{\kappa^2}{3H^2} \rho_m. \quad (5.2)$$

To facilitate the analysis, it is convenient to introduce a new set of variables

$$y \equiv \Omega_r = \frac{\kappa^2 \rho_r}{3H^2}, \quad x \equiv \Omega_m = \frac{\kappa^2 \rho_m}{3H^2} \quad \text{and} \quad \Omega_\Lambda \equiv \frac{\Lambda}{3H^2}.$$

These variables are commonly referred to as the expansion normalized variables (EN variables). This normalization helps to remove the explicit time dependence of the Hubble parameter, allowing for a clearer analysis of the system’s behavior. Additionally, EN variables lead to a more compact dynamical system and exploit underlying symmetries to reduce complexity.

Equations (5.1) and (5.2) take the form

$$1 = y + x + \Omega_\Lambda \quad (5.3)$$

$$\frac{\dot{H}}{3H^2} = -\frac{2}{3} y - \frac{1}{2} x \quad (5.4)$$

respectively. To construct the dynamical system, we differentiate the EN variables x and y^1 with respect to the number of e-foldings N , which is a dimensionless time variable. The number of e-folding is defined as $N = \log a$, so $dN = \frac{\dot{a}}{a} dt = H dt$.

$$y' \equiv \frac{dy}{dN} = \frac{1}{H} \frac{dy}{dt} = \frac{\kappa^2}{3H} \left[\frac{\dot{\rho}_r}{H^2} - 2 \frac{\dot{H}}{H^3} \rho_r \right] \stackrel{(2.11)}{\stackrel{(2.6)}}{=} - \frac{\kappa^2}{3H^3} \left[4H\rho_r + 2 \frac{\dot{H}}{H} \rho_r \right] = -y \left[4 + 2 \frac{\dot{H}}{H^2} \right] \quad (5.5a)$$

$$x' \equiv \frac{dx}{dN} = \frac{1}{H} \frac{dx}{dt} = \frac{\kappa^2}{3H} \left[\frac{\dot{\rho}_m}{H^2} - 2 \frac{\dot{H}}{H^3} \rho_m \right] \stackrel{(2.11)}{\stackrel{(2.6)}}{=} - \frac{\kappa^2}{3H^3} \left[3H\rho_m + 2 \frac{\dot{H}}{H} \rho_m \right] = -x \left[3 + 2 \frac{\dot{H}}{H^2} \right] \quad (5.5b)$$

By substituting equation (5.4) into the dynamical system (5.5), we ultimately derive the autonomous dynamical system

$$y' = 4y^2 + 3xy - 4y \quad (5.6a)$$

$$x' = 3x^2 + 4xy - 3x \quad (5.6b)$$

From the definitions of the variables y and x , it is evident that both variables are non-negative, i.e., $y, x \geq 0$. Considering that we are examining the scenario with a positive cosmological constant, we can rearrange equation (5.3) to derive the constraint $y + x \leq 1$. Taking into account these two requirements, the region of the phase space that yields viable cosmological results will be a triangular region defined by the vertices at $(0, 0)$, $(1, 0)$ and $(0, 1)$.

Besides the stability of each point, another useful tool is the effective EoS parameter of the universe, denoted by w_{eff} , as it provides a unified description of the combined effects of all components of the universe, including matter, radiation, and dark energy.

$$w_{eff} = \frac{p_{tot}}{\rho_{tot}} = \frac{\kappa^2}{3H^2} \left(\frac{\rho_r}{3} - \frac{\Lambda}{\kappa^2} \right) = \frac{y}{3} - \Omega_\Lambda = -1 + x + \frac{4}{3}y \quad (5.7)$$

where equation (5.3) was used to eliminate Ω_Λ .

By setting equations (5.6a) and (5.6b) to zero, we identify the critical points $A(0, 0)$, $B(0, 1)$ and $C(1, 0)$. Performing a linear stability analysis near these critical points (as discussed in Section 1.2), we calculate the eigenvalues of the Jacobian matrix. These eigenvalues enable us to determine the stability of each critical point. The relevant information is summarized in Table 4.1.

¹From equation (5.3), it is evident that one of the three variables can be expressed in terms of the remaining two, reducing the dynamical system to a 2D one. The choice of the two variables used is arbitrary.

Point	x	y	w_{eff}	Eigenvalues	Stability
A	0	0	-1	$\{-4, -3\}$	Stable Point
B	0	1	$1/3$	$\{1, 4\}$	Unstable Point
C	1	0	0	$\{-1, 3\}$	Saddle Point

Table 5.1: Properties of the critical points for the autonomous system of Λ CDM.

The first critical point, Point A , is characterized by both eigenvalues of the Jacobian matrix being negative, indicating that the point is stable. Additionally, the effective EoS parameter at this point is -1 , which is characteristic of a cosmological constant. Consequently, this critical point corresponds to the dark energy dominated era of the universe. The second critical point, Point B , has two positive eigenvalues, signifying that it is unstable. At this point, $w_{eff} = 1/3$, which is identical to the EoS parameter of radiation. Thus, this point represents the radiation-dominated era of the universe. And the third critical point, Point C , exhibits eigenvalues of the Jacobian matrix with different signs, designating it as a saddle point. The effective EoS parameter at this point is 0, corresponding to the matter-dominated era.

Observing Figure 5.1, these statements are corroborated. All trajectories originate from Point B , indicating it as the past attractor, and they converge at Point A , designating it as the future attractor. The position of Point A within the pink region signifies that the universe can accelerate in this state. Additionally, as illustrated in the same figure, some trajectories approach Point C while others diverge from it, which is characteristic of a saddle point. Each trajectory represents a different initial condition for the universe. It is evident that all initial conditions commence from the radiation dominated era and ultimately transition to a dark energy dominated era.

As we know, the universe underwent a radiation dominated era, followed by a matter dominated era, and is progressing towards a dark energy dominated era. This evolutionary path is represented by transitioning from Point B to Point C and then to Point A . However, the trajectory required for this sequence is highly constrained. If the value of the cosmological constant Λ is slightly higher than its actual value, selecting a trajectory that deviates from the line directly connecting Points B and C , the transition to the dark energy dominated era will occur earlier than it should, thereby bypassing the matter dominated epoch.

While this model is the most accurate representation we have to date, it is not

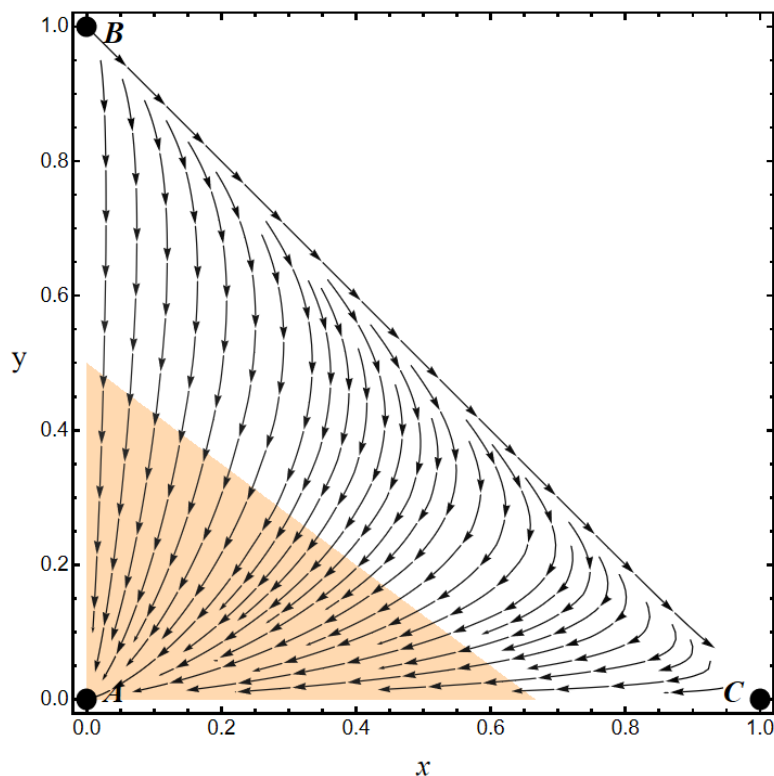


Figure 5.1: Phase space portrait for the Λ CDM dynamical system. The pink region indicates the area where the acceleration of the universe can occur.

without its imperfections and encounters issues that need to be addressed.

5.2.2 Challenges of the model

One of the most well-known issues is the “cosmological constant fine-tuning problem”. This problem arises from the observation that the measured value of the cosmological constant energy density deviates by at least 44 orders of magnitude from theoretical predictions, meaning the cosmological constant energy density is exceedingly small compared to typical particle physics scales. Specifically, quantum field theory predicts a vacuum energy density that is vastly larger than the observed value of the cosmological constant, necessitating an extremely precise cancellation to reconcile theory with observation [11, 53].

Another significant issue is the “coincidence problem”. This problem pertains to the observation that the energy densities of matter and dark energy are ap-

proximately equal in the present epoch, despite decreasing at different rates over time. Specifically, while the energy density of matter decreases as the universe expands, the energy density of dark energy remains constant. This phenomenon necessitates very specific initial conditions to achieve such a coincidence.

One proposed solution to this problem is the “anthropic principle” [93]. According to this principle, the fundamental constants of nature must fall within a narrow range that allows for the emergence of intelligent life in our universe. Once the cosmological constant begins to dominate the dynamics of the universe, structure formation halts because density perturbations no longer grow. Therefore, structure formation must be largely completed before vacuum energy domination; otherwise, there would be no observers, such as ourselves, to notice the universe. This argument results in a cosmological constant value that is two orders of magnitude different from the observed value of the vacuum energy density [94]. However, [95] argues that a scalar field with a linear potential could offer a potential resolution to this problem.

The most significant problem with the Λ CDM model is the “Hubble tension”, the discrepancy between the Hubble constant H_0 , measured using the distance ladder approach and the value inferred from the angular scale of fluctuations in the CMB within the context of this model. According to the latest Planck data [50], the best value for the Hubble constant is $H_0 = 67.64 \pm 0.52 \text{ km s}^{-1} \text{ Mpc}^{-1}$ while the Pantheon+ dataset combined with SH0ES gives a best fit value of $H_0 = 73.4 \pm 1.1 \text{ km s}^{-1} \text{ Mpc}^{-1}$ [96].

There are also additional issues, such as the growth tension, CMB anisotropy anomalies, cosmic dipoles, small scale problems [12], and a few more (for an extensive discussion on the challenges of the model, see [13]).

5.3 Quintessence

Rearranging the first Friedmann equation from Table 4.1, in the presence of a barotropic fluid and a scalar field, yields

$$1 = \frac{\kappa^2}{3H^2}\rho_b + \frac{\kappa^2}{6H^2}\dot{\phi}^2 + \frac{\kappa^2}{3H^2}V, \quad (5.8)$$

where ρ_b is the energy density of the barotropic fluid and ρ_ϕ was replaced using equation (4.7). Remember that for quintessence fields $\epsilon = +1$. In this context, we define the EN variables as follows,

$$x \equiv \sqrt{\frac{\kappa^2}{6H^2} \dot{\phi}^2} = \frac{\kappa}{\sqrt{6}H} \dot{\phi}, \quad y \equiv \sqrt{\frac{\kappa^2}{3H^2} V} = \frac{\kappa}{\sqrt{3}H} \sqrt{V} \quad \text{and} \quad \Omega_b \equiv \frac{\kappa^2}{3H^2} \rho_b.$$

Now, equation (5.8) can be rewritten as

$$\Omega_b + x^2 + y^2 = 1, \quad (5.9)$$

from where we can understand that x^2 represents the kinetic energy density parameter of the field, while y^2 corresponds to its potential energy density parameter. Also, we observe that $0 \leq x^2 + y^2 \leq 1$, indicating that the physically viable solutions are restricted to the unit disc centered at the origin.

Additionally, the acceleration equation will be utilized. By referring to the same Table and inserting the new EN variables along with equations (4.7), (4.8), (2.6) and (5.9), takes the form

$$\frac{\dot{H}}{3H^2} = -\frac{1}{2} (1 + x^2 - y^2 + w_b (1 - x^2 - y^2)) \quad (5.10)$$

Once again, in order to construct the dynamical system, we differentiate the EN variables x and y with respect to the number of e-foldings N . Before proceeding with this differentiation, we introduce two new variables that are crucial for our analysis

$$\lambda \equiv \frac{1}{\kappa V} \frac{dV}{d\phi} \quad \text{and} \quad \Gamma \equiv \frac{d^2 V}{d\phi^2} \frac{V}{(dV/d\phi)^2}.$$

where λ is the roll parameter and Γ is the track parameter. The dynamical system becomes

$$\begin{aligned} x' \equiv \frac{dx}{dN} &= \frac{1}{H} \frac{dx}{dt} = \frac{\kappa}{\sqrt{6}H} \left[\frac{\ddot{\phi}}{H} - \frac{\dot{H}}{H} \dot{\phi} \right] \stackrel{(4.10)}{\stackrel{(5.10)}}{=} \\ &= -\frac{3}{2} \left[2x + x^3 (w_b - 1) + (1 + w_b) x (y^2 - 1) - \sqrt{\frac{2}{3}} \lambda y^2 \right] \end{aligned} \quad (5.11a)$$

$$\begin{aligned} y' \equiv \frac{dy}{dN} &= \frac{1}{H} \frac{dy}{dt} = \frac{\kappa}{\sqrt{3}H} \left[\frac{1}{H} \frac{dV}{d\phi} \dot{\phi} - \frac{\dot{H}}{H^2} \sqrt{V} \right] \stackrel{(5.10)}{=} \\ &= -\frac{3}{2} y \left[(w_b - 1) x^2 + (1 + w_b) (y^2 - 1) + \sqrt{\frac{2}{3}} \lambda x \right]. \end{aligned} \quad (5.11b)$$

However, since λ is dependent on the scalar field ϕ , the dynamical system cannot be considered closed with only the EN variables. Therefore, we will introduce λ as an additional dynamical variable to ensure the completeness of the system.

Consequently, the autonomous 3D dynamical system for a general potential $V(\phi)$ can be written as

$$x' = -\frac{3}{2} \left[2x + x^3 (w_b - 1) + (1 + w_b) x (y^2 - 1) - \sqrt{\frac{2}{3}} \lambda y^2 \right] \quad (5.12a)$$

$$y' = -\frac{3}{2} y \left[(w_b - 1) x^2 + (1 + w_b) (y^2 - 1) + \sqrt{\frac{2}{3}} \lambda x \right] \quad (5.12b)$$

$$\lambda' = -\sqrt{6} \lambda^2 x [\Gamma - 1]. \quad (5.12c)$$

Although Γ is explicitly dependent on the scalar field, it can be related to λ . If $\lambda(\phi)$ is invertible, one can express ϕ as a function of λ and subsequently obtain Γ as a function of λ . However, if $\lambda(\phi)$ is not invertible, it will be necessary to define a different set of variables than those currently in use.

Under the reflection $(x, y) \rightarrow (x, -y)$, the point (x', y') reflects to $(x', -y')$. Consequently, the autonomous system of (x', y') is symmetric under this reflection, allowing us to study only the upper half-plane of the disc, as the lower half-plane mirrors the upper one. Additionally, under the assumption $\Gamma(-\lambda) = \Gamma(\lambda)$, the system exhibits parity-odd invariance when restricted to planes of constant y . Therefore, we can fully analyze the system by considering only positive values of λ .

Lastly, the effective EoS parameter and the EoS parameter of the scalar field, expressed in terms of the EN variables, are given by

$$w_{eff} = w_b + (1 - w_b) x^2 - (1 + w_b) y^2 \quad (5.13)$$

$$w_\phi = \frac{x^2 - y^2}{x^2 + y^2}, \quad (5.14)$$

respectively.

5.3.1 Exponential potential

One promising potential to begin investigating quintessence is the exponential potential, which arises naturally from theories of gravity such as scalar-tensor theories [97, 98] or string theories [99, 100]. This potential is of the form

$$V(\phi) = V_0 e^{-\lambda \kappa \phi}. \quad (5.15)$$

From the definitions of λ and Γ , it is straightforward to determine that λ is a constant while Γ is equal to one. Therefore, the autonomous dynamical system

(5.12) reduces to a 2D system.

To determine the fixed points, we set equations (5.12a) and (5.12b) to zero simultaneously. This yields the fixed Points $A(-1, 0)$, $B(0, 0)$, $C(1, 0)$, $D\left(\frac{\lambda}{\sqrt{6}}, \sqrt{1 - \frac{\lambda^2}{6}}\right)$, and $E\left(\sqrt{\frac{3}{2}} \frac{1+w_b}{\lambda}, \sqrt{\frac{3}{2}} \frac{1-w_b^2}{\lambda^2}\right)$. These Points exist for all values of λ except for Points D and E , which exist only for $\lambda^2 < 6$ and $\lambda^2 \geq 3(1 + w_b)$ respectively². By performing a linear stability analysis, we obtain the information presented in Table 5.2.

Point	x	y	w_{eff}	Eigenvalues	Stability
A	-1	0	1	$\{3 - 3w_b, 3 + \sqrt{\frac{3}{2}} \lambda\}$	Unstable Node for $\lambda > -\sqrt{6}$ Saddle for $\lambda < -\sqrt{6}$
B	0	0	w_b	$\{\frac{3}{2}(w_b + 1), \frac{3}{2}(w_b - 1)\}$	Saddle Point
C	1	0	1	$\{3 - 3w_b, 3 - \sqrt{\frac{3}{2}} \lambda\}$	Unstable Node for $\lambda < \sqrt{6}$ Saddle for $\lambda > \sqrt{6}$
D	$\frac{\lambda}{\sqrt{6}}$	$\sqrt{1 - \frac{\lambda^2}{6}}$	$\frac{\lambda^2}{3} - 1$	$\{\frac{\lambda^2}{2} - 3, \lambda^2 - 3w_b - 3\}$	Saddle for $3(w_b + 1) < \lambda^2 < 6$ Stable Node for $\lambda^2 < 3(w_b + 1)$
E	$\sqrt{\frac{3}{2}} \frac{1+w_b}{\lambda}$	$\sqrt{\frac{3}{2}} \frac{1-w_b^2}{\lambda^2}$	w_b	$\{\frac{3}{4\lambda}((w_b - 1)\lambda + \Delta), \frac{3}{4\lambda}((w_b - 1)\lambda - \Delta)\}$	Stable Spiral for $\lambda^2 > \frac{24(w_b+1)^2}{7+9w_b}$ Stable Node for $3(w_b + 1) < \lambda^2 < \frac{24(w_b+1)^2}{7+9w_b}$

Table 5.2: Properties of the critical points for the autonomous system with the exponential potential. Here $\Delta = \sqrt{(w_b - 1)((7 + 9w_b)\lambda^2 - 24(w_b + 1)^2)}$

We observe that for different values of λ , some critical points exhibit varying

²The former condition is derived by requiring $0 < y < 1$, while the latter follows from the constraint $0 \leq x^2 + y^2 \leq 1$.

stability properties. Points A and C display similar behaviors. Specifically, they can act as either an unstable node or a saddle point based on the value of λ . In these cases, the universe is dominated by the kinetic energy of the scalar field, resulting in a stiff fluid EoS parameter.

The concept of stiff matter was first introduced by Zel'dovich to describe a cold gas of baryons interacting via a meson field [101]. He referred to it as “stiff” because it represents the most rigid EoS possible, where the pressure is directly proportional to the energy density ($w = 1$). In this context, any increase in energy density results in an equal increase in pressure. Furthermore, for values of $w > 1$, the speed of sound would exceed the speed of light, violating the causality limits imposed by General Relativity [102].

However, in the context of scalar fields, the term “stiff fluid” takes on a different meaning. Rather than referring to a physical baryonic gas, it characterizes a regime where the kinetic energy of the scalar field dominates over its potential energy. In this regime, the scalar field exhibits an EoS parameter of $w = 1$, meaning the pressure and energy density are tightly coupled. Unlike Zel'dovich's use of the term, where stiff matter is associated with a physical fluid, in the case of the scalar field, the stiff fluid represents a dynamical state in which the scalar field mimics the behavior of stiff matter due to its rapid kinetic evolution.

While a stiff fluid EoS is generally not viable at the classical macroscopic level, these solutions are typically relevant only during the early stages of the universe's evolution. It is during these times that new phenomena, such as inflation, are expected to begin manifesting. Consequently, the effective description provided by the quintessence model may break down in this regime, leading to the stiff fluid solutions being largely ignored in most cosmological scenarios [83].

Moving on, Point B , which represents the origin of the phase space portrait, corresponds to the fluid-dominated era. As expected, it always acts as a saddle point, with the scalar field being absent during this phase.

One possible late-time attractor is Point D , which represents the scalar field-dominated solution and exists for sufficiently flat potentials (specifically, it exists for $\lambda^2 < 6$). The EoS parameter for this point can lead to accelerated expansion of the universe if and only if $\lambda^2 < 2$. However, the behavior of the system changes depending on whether λ^2 is greater or less than $3(w_b + 1)$. In the former case, the late-time attractor shifts to Point E . At this point, the ratio of the energy density of dark energy to that of the barotropic fluid remains constant, and the scalar field

closely follows the dynamics of the background fluid, resulting in what is known as a scaling solution. While this solution can help address the coincidence problem, it does not lead to accelerated expansion, as the effective EoS parameter remains constant and equal to w_b .

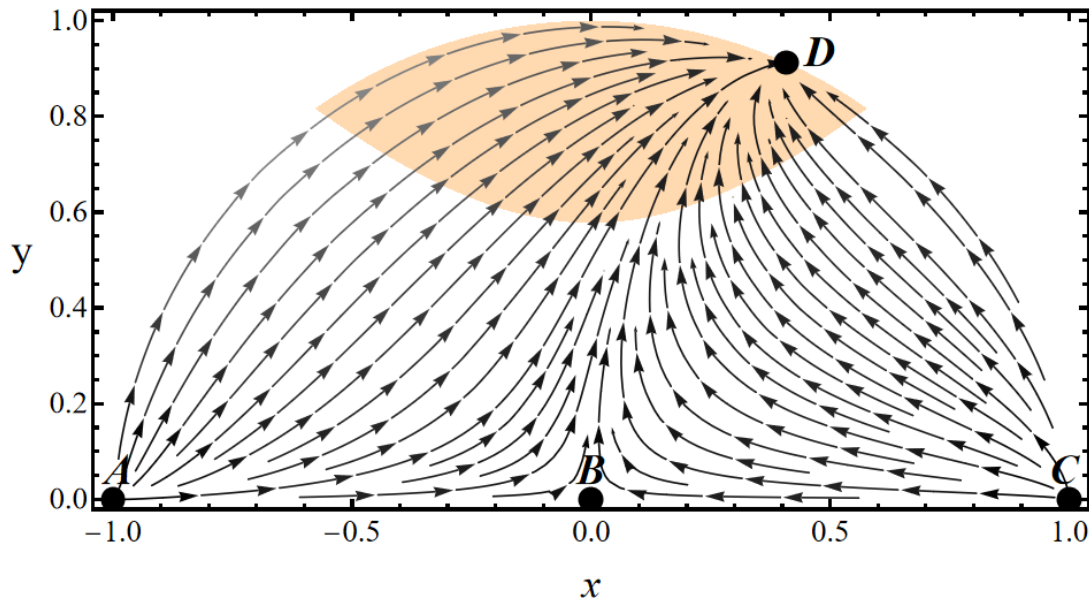


Figure 5.2: The phase space portrait for the exponential potential with $0 < \lambda^2 < 3(w_b + 1)$ (specifically, $\lambda = 1$ and $w_b = 0$). As before, the pink region indicates the area where the acceleration of the universe can occur.

Figures 5.2, 5.3 and 5.4 illustrate the phase space portraits for all possible values of λ . In the regime where $0 < \lambda^2 < 3(w_b + 1)$ (as shown in Figure 5.2), the universe evolves toward Point D , the scalar field-dominated solution. This point lies within the region that allows for accelerated expansion, as the value of λ was chosen to be 1 for the specific phase space portrait. It is important to remember that accelerated expansion can only occur when $\lambda^2 < 2$. According to [84], the existence of such a scalar field today is unlikely unless its energy density has been significantly suppressed relative to the attractor value for the majority of the dust-dominated era.

When $3(w_b + 1) < \lambda^2 < 6$ (as shown in Figure 5.3), the evolution changes. In this scenario, both Points D and E exist. Point D acts as a saddle point, while Point E is a stable spiral³. The late-time attractor always lies outside the desired

³If we had selected a value satisfying $\lambda^2 \leq \frac{24(w_b+1)^2}{7+9w_b}$ while still within the range $3(w_b + 1) <$

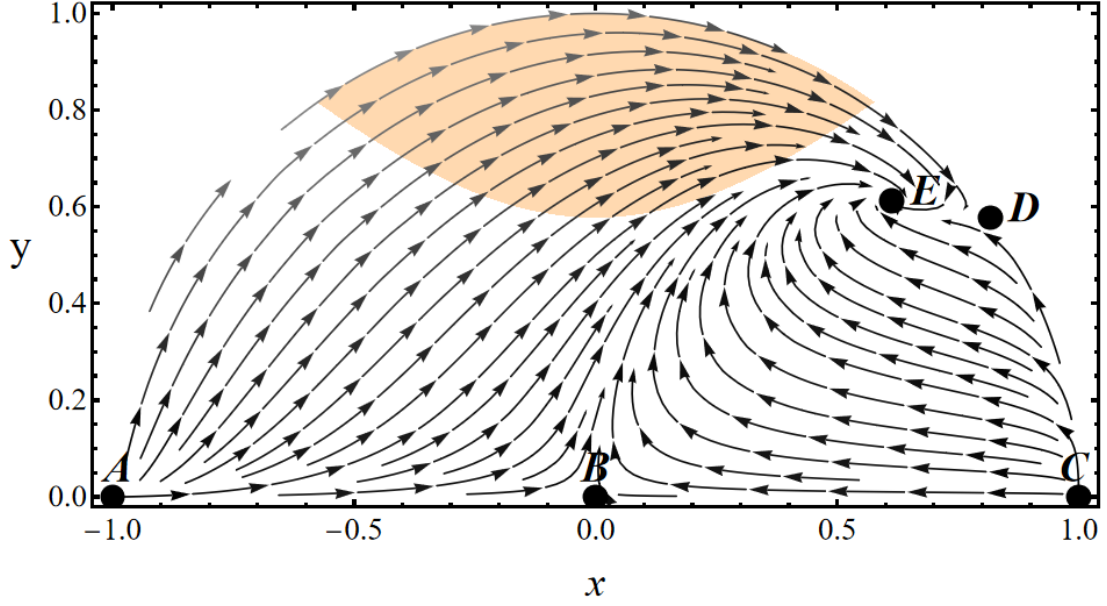


Figure 5.3: The phase space portrait for the exponential potential with $3(w_b + 1) < \lambda^2 < 6$ (specifically, $\lambda = 2$ and $w_b = 0$).

acceleration regime, making it unsuitable for describing the behavior of dark energy. At this point, the effective EoS parameter aligns with that of the background fluid, causing the universe to undergo a barotropic-like expansion, even though it is not entirely dominated by the barotropic fluid.

Lastly, in the case where $\lambda^2 > 6$, Point D ceases to exist as a viable critical point, as the potential is too steep for the scalar field to dominate. Consequently, the universe evolves towards Point E , which represents a scaling solution. In this regime, the scalar field cannot drive exponential acceleration, as its energy density remains subdominant relative to the background fluid. However, if the slope of the exponential potential becomes sufficiently shallow, satisfying $\lambda^2 < 2$ near the present time, the dynamics of the system shift. The universe will exit the scaling regime, allowing the scalar field to dominate and move towards Point D .

In an effort to understand the existence of the attractor, authors in [103] investigate the evolution of the scalar field $\phi(t)$ and show that for a sufficiently steep exponential potential, when the energy density of the scalar field significantly exceeds that of the background fluid, the potential energy remains small relative to

$\lambda^2 < 6$, Point E would be a stable node rather than a stable spiral. Nevertheless, Point E would remain stable.

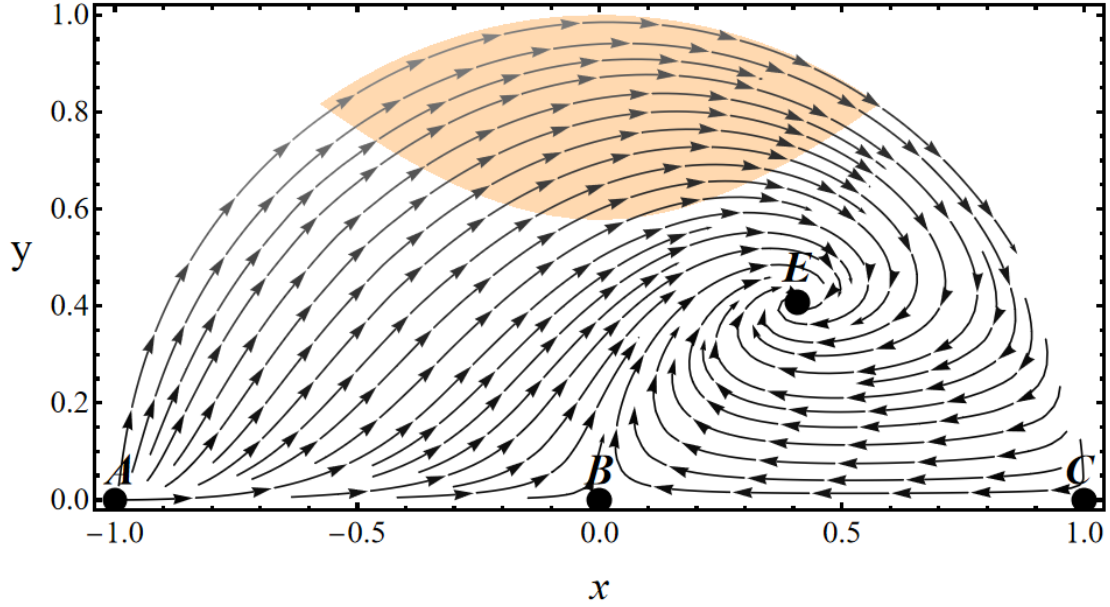


Figure 5.4: The phase space portrait for the exponential potential with $\lambda^2 > 6$ (specifically, $\lambda = 3$ and $w_b = 0$).

the kinetic energy. This condition allows the field to maintain a rapid scaling behavior. This rapid scaling is driven by the steep potential, which causes the scalar field to evolve quickly, leading to a faster decrease in its energy density compared to that of the background fluid. However, when the energy density of the scalar field is significantly less than that of the background fluid, the damping effect from the dominant background fluid becomes more pronounced. This increased damping slows the evolution of the scalar field, causing the potential energy to stabilize and eventually catch up with the kinetic energy. As a result, the rate at which the scalar field's energy density scales diminishes, allowing the background fluid's energy density to decrease more rapidly. The time at which the scalar field will enter the attractor solution is thus determined by its initial energy density.

Returning to the idea of varying the value of λ over time, one can achieve this by combining potentials with different slopes [53, 104]. This approach allows for the construction of solutions that initially experience a period of scaling during the radiation and matter-dominated eras. These solutions can then smoothly transition to dominate the energy density in the present epoch, effectively explaining the current accelerated expansion of the universe.

5.3.2 Inverse power-law potential

As previously mentioned, if λ changes dynamically, it is possible to achieve exponential acceleration. A widely studied potential, that exhibits this behavior, and can be found in models of supersymmetric QCD [105], is the inverse power-law potential, which is given by

$$V(\phi) = V_0 \phi^{-\alpha}. \quad (5.16)$$

An interesting feature of this potential is that it can also help alleviate the fine-tuning problem associated with initial conditions. This is achieved through the introduction of the “tracker solution” [106, 107]. The tracker solution acts as an attractor in the phase space, in the sense that a wide range of initial conditions for ϕ and $\dot{\phi}$ rapidly converge to a common evolutionary path. As a result, the cosmology becomes largely independent of the specific initial conditions of the scalar field, reducing the sensitivity to the early universe’s state.

It is straightforward, from their definitions, to derive that $\lambda = \frac{\alpha}{\kappa\phi}$ and $\Gamma = 1 + \frac{1}{\alpha}$. For a tracker solution to exist, the condition $\Gamma > 1$ must be satisfied [107], which implies that $\alpha > 0$.

Because $\lambda \rightarrow \infty$, we make a change of variable to constrain the phase space within finite boundaries [108]. Specifically, we use the transformation

$$\lambda = \frac{z}{1-z} \Rightarrow z = \frac{\lambda}{\lambda+1} \quad (5.17)$$

so that $z \in [0, 1]$, with the $z = 0$ surface corresponding to $\lambda = 0$ and the $z = 1$ surface corresponding to $\lambda \rightarrow \infty$. The dynamical system (5.12) now takes the form

$$x' = -\frac{3}{2} \left[2x + x^3 (w_b - 1) + (1 + w_b) x (y^2 - 1) - \sqrt{\frac{2}{3}} \frac{z}{1-z} y^2 \right] \quad (5.18a)$$

$$y' = -\frac{3}{2} y \left[(w_b - 1) x^2 + (1 + w_b) (y^2 - 1) + \sqrt{\frac{2}{3}} \frac{z}{1-z} x \right] \quad (5.18b)$$

$$z' = -\sqrt{6} z^2 x [\Gamma - 1]. \quad (5.18c)$$

However, $\lim_{z \rightarrow 1^-} x' \rightarrow +\infty$ and $\lim_{z \rightarrow 1^-} y' \rightarrow \mp\infty$, depending on whether x is positive or negative. To avoid this issue, we multiply the right-hand side of (5.18) by $(1 - z)$. Although this approach is not mathematically rigorous, the critical points and their stability will remain unaffected since $1 - z > 0$. Consequently, the 3D

autonomous dynamical system becomes

$$x' = -\frac{3}{2}(1-z) [2x + x^3(w_b - 1) + (1 + w_b)x(y^2 - 1)] + \sqrt{\frac{3}{2}}zy^2 \quad (5.19a)$$

$$y' = -\frac{3}{2}(1-z)y [(w_b - 1)x^2 + (1 + w_b)(y^2 - 1)] - \sqrt{\frac{3}{2}}yzx \quad (5.19b)$$

$$z' = -\sqrt{6}z^2x(1-z)[\Gamma - 1]. \quad (5.19c)$$

This system yields five critical points; Points $A(0, 0, \text{arbitrary})$, $B(\text{arbitrary}, 0, 1)$, $C(-1, 0, 0)$, $D(1, 0, 0)$ and $E(0, 1, 0)$. The fixed points and their properties are summarized in Table 5.3.

Point	x	y	z	w_{eff}	Eigenvalues	Stability
A	0	0	arbitrary	w_b	$\{0, -\frac{3}{2}(w_b - 1)(z - 1), -\frac{3}{2}(w_b + 1)(z - 1)\}$	Saddle Line
B	arbitrary	0	1	$w_b + (1 - w_b)x^2$	$\{-\sqrt{\frac{3}{2}}x, 0, \sqrt{6}(\Gamma - 1)x\}$	Saddle Line
C	-1	0	0	1	$\{3, 0, 3 - 3w_b\}$	Unstable Node
D	1	0	0	1	$\{3, 0, 3 - 3w_b\}$	Saddle Point
E	0	1	0	-1	$\{-3, 0, -3 - 3w_b\}$	Stable Node

Table 5.3: Properties of the critical points for the autonomous system with the inverse power-law potential.

Starting with Point A , it is important to note that we are not dealing with a single isolated point, but rather an entire line and specifically, the z -axis. The two non-zero eigenvalues of the Jacobian matrix along this line always have opposite signs⁴, making this critical line a saddle. It corresponds to the fluid domination era, with the energy density of the scalar field non-existent, and the dynamics governed entirely by the barotropic fluid.

Point B also corresponds to a critical line. By the definition of z , all points with $z = 1$ represent the limit $\lambda \rightarrow \infty$. Since there are no other critical points in the $z = 1$ plane, this critical line fully characterizes the $\lambda \rightarrow \infty$ limit. As mentioned

⁴Do not forget that $0 \leq z \leq 1$ and the barotropic fluid EoS parameter satisfies $0 \leq w_b \leq 1/3$.

earlier, we focus in the case where $\alpha > 0$, which means that the non-zero eigenvalues always have opposite signs, regardless of whether $x > 0$ or $x < 0$, making this critical line a saddle as well. When $x = 0$, all the eigenvalues become zero, causing the point $(0, 0, 1)$ to behave as a center. The effective EoS parameter falls within the range $w_b \leq w_{eff} \leq 1$, which means that the universe cannot achieve the desired accelerated expansion.

Moving on, Point C is once again identified as a non-hyperbolic critical point. This point is isolated in the phase space, and the non-zero eigenvalues of the Jacobian matrix at this point have the same sign. To determine the stability, we analyze its center manifold, as non-hyperbolic points require more careful examination. The detailed mathematical analysis, which can be found in Appendix B.2, reveals that the center manifold of Point C is parallel to the z -axis. By studying the flow along this manifold, we conclude that Point C is an unstable node and, therefore, a past attractor. A similar situation occurs with Point D , except that the center manifold analysis in Appendix B.3 indicates that it is a saddle point. Both of these points correspond to stiff fluid domination, where the universe is primarily influenced by the kinetic energy of the field.

Lastly, we consider Point E , another non-hyperbolic, isolated fixed point. Its stability is analyzed using center manifold theory. At this point, the potential energy of the scalar field dominates, and the effective EoS parameter corresponds to that of a cosmological constant. As detailed in Appendix B.1, this point is identified as a stable node. Moreover, as illustrated in Figure 5.5, nearly all trajectories converge to the center manifold of Point E , regardless of the initial conditions. This behavior is consistent with the tracker solution discussed earlier.

The larger the value of λ , the easier it is for the scalar field to catch up with the scaling solution since the potential is steeper and the field evolves quicker [109]. Therefore, to achieve the tracking solution at Point E , the roll parameter λ must have a large initial value [110]. Since $\lambda = \frac{\alpha}{\kappa\phi}$, this condition can be satisfied if the scalar field has a small initial value ($\phi_i \ll M_p$ [111]). Small scalar field amplitudes are preferred in the early universe because large excursions of the field, potentially reaching or exceeding the Planck scale, could trigger significant quantum gravitational effects, leading to a breakdown of the effective field theory (EFT) framework [83].

While the tracker solution does not resolve the cosmic coincidence problem, it significantly alleviates the issue of fine-tuning the initial conditions. However, this advantage is tempered by the fact that the fine-tuning is merely transferred to the

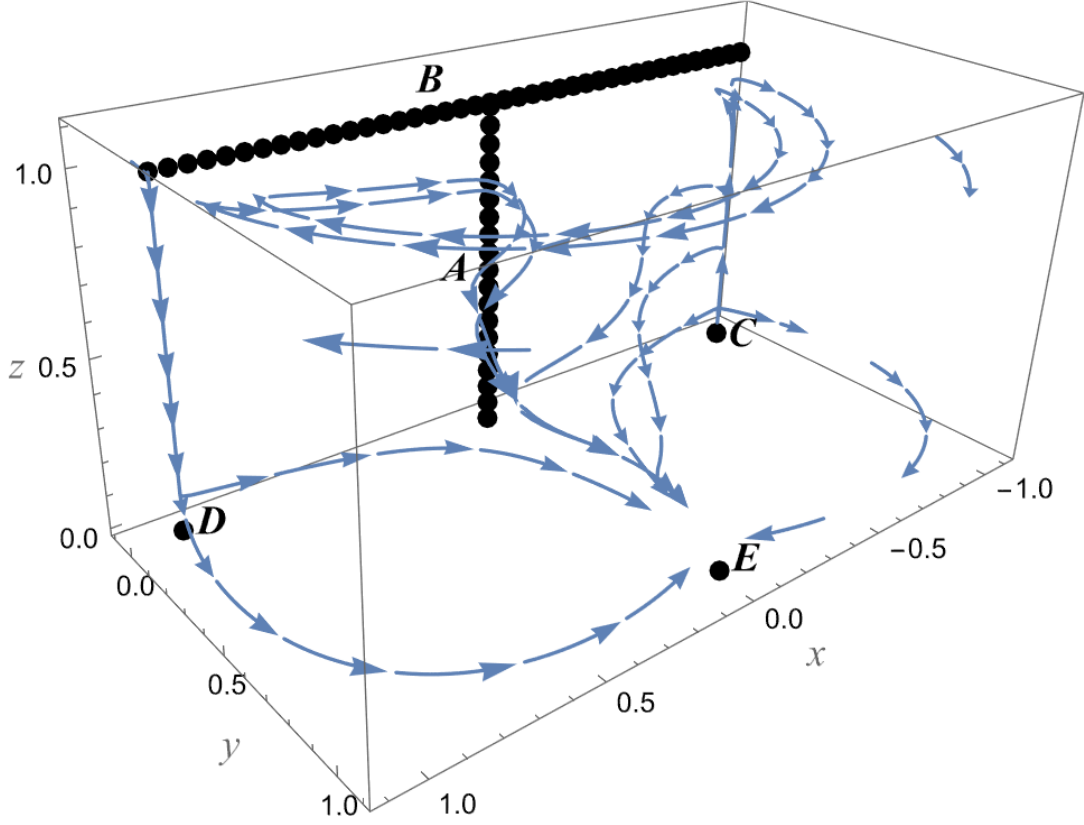


Figure 5.5: The phase space portrait for the inverse power-law potential, with the specific parameters set as $w_b = 0$ and $\Gamma = 1.1$.

parameters of the potential, rather than being eliminated. Thus, the problem persists, although in a different form. Observational constraints favor flatter potentials with $\alpha < 0.075$ [112]. Although the inverse power-law potential emerges from a fermion condensate model in globally supersymmetric gauge theories, the theoretical values of α predicted by such models are typically larger than what observations allow [112]. Moreover, the ultra-light mass of the scalar field ($m_\phi \sim 10^{-33}$ eV [113]) poses a challenge, as it is difficult to reconcile with the energy scales in particle physics.

Chapter 6

Transition Quintessence

Thus far, our analysis has concentrated on models in which the scalar field evolves smoothly over time, without exhibiting any abrupt changes in behavior. In this chapter, we extend the standard Λ CDM framework to include models that feature a distinct transition at a specific redshift. These extensions are designed to explore potential changes in the expansion history of the universe, particularly those that could offer insights into unresolved cosmological tensions such as the Hubble constant discrepancy.

6.1 Unified Dark Matter

A prominent example of late-time modifications is the Unified Dark Matter (UDM) model, also referred to as Quartessence. In this model, a single fluid is responsible for both the formation of large-scale structure in the early universe and the accelerated expansion observed at late times [114, 115]. In other words, dark matter and dark energy are understood as different manifestations of the same underlying dark component, offering a unified framework for both phenomena. While quintessence models are distinguished by the form of their potential, UDM models are differentiated by the a priori choice of pressure or EoS parameter [114]. This distinction fundamentally influences the dynamics of the model, as the pressure or EoS parameter governs the evolution of the dark fluid, determining how it behaves in the early and late universe.

UDM models without phase transitions encounter significant fine-tuning issues with their parameters, making them almost indistinguishable from the standard Λ CDM model [115]. To address this issue, a transition between the dark matter-dominated era and a dark energy-like evolution is introduced [114–117]. This tran-

sition introduces two additional parameters; the speed of the transition, denoted by β , and the scale factor at which the transition occurs, a_t . At a background level, Λ CDM can be viewed as a special case within the broader class of UDM models.

In [115], a UDM model is proposed that allows for an EoS parameter $w < -1$ after the transition without violating the dominant energy condition. By analyzing the properties of perturbations, with a focus on the evolution of the effective speed of sound and the Jeans scale, the authors conclude that a sufficiently fast transition occurring early enough could be compatible with observational data. Following a Bayesian analysis that incorporates data from SNIa, BAO, and the CMB, authors in [114] find that intermediate and fast transitions are favored. In particular, slow transitions are ruled out by the CMB data. However, in [116], it is argued that the fast transition regime fails to resolve the Hubble tension. A Bayesian analysis was performed in this study without the inclusion of BAO data, and the results indicate a preference for a smoother transition over a fast one. Furthermore, the analysis strongly favors the Λ CDM model over the UDM model, suggesting that the latter may not provide a satisfactory resolution to current cosmological tensions.

6.2 Λ_s CDM

Observational data suggest that dark energy may have a negative energy density at higher redshifts ($z \gtrsim 2$) or even behave as pressureless matter at certain redshifts [118, 119]. In [120], the concept of graduated dark energy (gDE) is introduced. This phenomenological model is characterized by a smooth function that captures the transition of the cosmological constant, which switches sign at a certain redshift z_t ¹ and becomes positive in the late universe. This sign change induces a sharp alteration in the Hubble parameter $H(z)$, which could improve the fit to observational data. Notably, the closer the energy density of gDE approximates a step-function, the better the fit to the data. This observation inspired the Λ_s CDM model, a promising late-time modification of the standard model. In this framework, the cosmological constant assumes a negative value in the past and spontaneously switches sign at a specific redshift², eventually attaining its current positive value [28].

¹In the paper, this is denoted as z_* .

²In [28–31], the redshift at which the transition occurs is represented by z_\dagger .

Mathematically, the transition in the cosmological constant can be expressed as

$$\Lambda \rightarrow \Lambda_s \equiv \Lambda_{s0} \text{sgn}(z_t - z), \quad (6.1)$$

where $\Lambda_{s0} > 0$ and sgn denotes the signum function. It is evident that, before the transition ($z > z_t$), the universe has a negative cosmological constant, while after the transition ($z < z_t$), the usual positive cosmological constant is present. Notably, at the time of the transition ($z = z_t$), the cosmological constant momentarily vanishes. Using this formulation, the Hubble parameter takes the form

$$H^2(z) = H_0^2 [\Omega_{0r}(1+z)^4 + \Omega_{0m}(1+z)^3 + \Omega_{0\Lambda_s} \text{sgn}(z_t - z)]. \quad (6.2)$$

It is clear that, after the transition, the Hubble parameter in the Λ_s CDM model becomes identical to that of the standard Λ CDM model. This equivalence also holds at very high redshifts ($z \gtrsim z_{ls}$, where $z_{ls} \approx 1100$ is the redshift of last scattering), at which point the contribution from dark energy becomes negligible.

The comoving angular diameter distance to last scattering, $D_M(z_{ls})$, is determined in an almost model-independent way by the CMB power spectra. Consequently, the Λ_s CDM model must yield the same value for this distance as the standard Λ CDM model. Before the transition, when Λ_s is negative, Λ_s CDM results in a lower value for $H(z)$ compared to Λ CDM. However, in order to match the same $D_M(z_{ls})$ for both models, the Hubble parameter must increase after the transition, leading to higher values of the Hubble constant H_0 . Additionally, H_0 and z_t are inversely correlated, as shown clearly in Figure 2 of [28]. This correlation arises partly because $D_M(z_{ls})$ is fixed, and also because, as the redshift of the transition increases, the negative value of Λ_s exerts less influence on the evolution of $H(z)$.

In addition to potentially higher values of H_0 , this model also provides improved agreement with the Ly- α BAO data. The Ly- α BAO data, which are based on the measurement of BAO using the Ly- α forest, benefit from the abrupt change in the Hubble parameter (see Figure 3 of [28]). The Ly- α forest consists of absorption lines observed in the spectra of distant quasars, which are caused by intervening hydrogen clouds along the line of sight [121]. As light from the quasars passes through these clouds, it is absorbed at the Lyman- α wavelength, resulting in a “forest” of absorption features that provide valuable insights into the distribution of matter in the early universe. These data suggest that the transition redshift, z_t , should be less than 2.34. However, the Galaxy BAO data appear to favor a larger value of z_t , while the CMB data do not offer strong constraints on this parameter.

A recent Bayesian analysis of the Λ_s CDM model [30], incorporating data from the CMB, BAO³, and SNIa (Pantheon+), found strong evidence in favor of the Λ_s CDM model. When additional data from SH0ES and KiDS-1000⁴ were included, the evidence in favor of the model became even stronger. In this case, the best-fit value for the transition redshift was found to be $z_t = 1.72^{+0.09}_{-0.12}$, and the Hubble constant was measured as $H_0 = 73.16 \pm 0.64 \text{ km s}^{-1} \text{ Mpc}^{-1}$, which is in full agreement with the value $H_0 = 73.04 \pm 1.04 \text{ km s}^{-1} \text{ Mpc}^{-1}$ expected from SH0ES. Furthermore, the same study calculated the age of the universe to be $t_0 = 13.522 \pm 0.027 \text{ Gyr}$, which is consistent with the age derived from the oldest globular clusters, $13.50 \pm 0.15 \text{ Gyr}$. In contrast, the Λ CDM model yields $t_0 = 13.787 \pm 0.020 \text{ Gyr}$ [75].

The success of the Λ_s CDM model extends beyond its superior statistical fit to observational data. With the advent of the James Webb Space Telescope (JWST), the high-redshift universe is being explored in unprecedented detail for the first time. This model offers an explanation for the observed more intense growth of luminous galaxies. As mentioned earlier, before the transition, the Hubble parameter in the Λ_s CDM model is lower than that predicted by Λ CDM. This results in reduced resistance to structure formation, thereby facilitating faster growth of cosmic structures. In contrast, the increased expansion rate in the standard Λ CDM model leads to greater resistance to structure growth, slowing down the process [31]. However, some studies [122, 123] suggest that simulations based on the standard Λ CDM model can reproduce galaxies that are consistent with the observations made by JWST. According to these authors, there is no significant discrepancy between the findings of JWST and the predictions of the Λ CDM model.

As demonstrated, the Λ_s CDM model represents one of the simplest extensions of the standard cosmological model, yet it achieves notable phenomenological success. The next challenge lies in identifying an underlying physical mechanism that can account for its behavior. In the following section, we aim to explore this by investigating a step-like potential in both quintessence and phantom fields. The goal is to examine how these field theories can reproduce the phenomenological results observed in the Λ_s CDM model.

³A less model-dependent dataset was used compared to the one in [28, 29].

⁴KiDS-1000 maps the large-scale structure of the universe by measuring the distribution of matter through weak gravitational lensing. By analyzing cosmic shear, which refers to the slight distortions in galaxy shapes caused by intervening matter, KiDS-1000 provides valuable insights into the cosmic structure.

6.3 Step-like potential

To investigate the dynamics of the system, we consider both the acceleration equation and the Klein-Gordon equation for the scalar field

$$\frac{\ddot{a}}{a} = -\frac{\kappa^2}{3} \left(\epsilon \dot{\phi}^2 - V(\phi) \right) - \frac{\Omega_{0m} H_0^2}{2a^3} \quad (6.3)$$

$$\ddot{\phi} + 3\frac{\dot{a}}{a}\dot{\phi} + \epsilon \frac{\partial V(\phi)}{\partial \phi} = 0. \quad (6.4)$$

We consider a step-like potential, which can be expressed as

$$V(\phi) = \frac{3H_0^2}{\kappa^2} \left(V_0 + \Delta V \tanh \left(\frac{\phi - \phi_t}{s} \right) \right). \quad (6.5)$$

The parameter ϕ_t denotes the scalar field value at which the transition occurs, while s defines the width of the transition, thereby controlling the smoothness or abruptness of the potential's step and influencing the speed of the transition. The parameters ΔV , which represents the height or depth of the step in the potential, and V_0 , the central or baseline value of the potential (essentially the value at the midpoint of the step), are selected such that $V_0 - \Delta V = \Omega_{0\phi} = 1 - \Omega_{0m}$. This condition ensures that, in the present epoch, the scalar field is nearly frozen, if not entirely so. By changing the variables as outlined below,

$$\bar{t} = H_0 t \quad (6.6a)$$

$$\bar{\phi} = \frac{\kappa}{\sqrt{3}} \phi \quad (6.6b)$$

$$\bar{V}(\bar{\phi}) = \frac{\kappa^2}{3H_0^2} V(\phi) \quad (6.6c)$$

we transform (6.3) and (6.4) into dimensionless form

$$\frac{a''}{a} = -\epsilon(\bar{\phi}')^2 + \bar{V}(\bar{\phi}) - \frac{\Omega_{0m}}{2a^3} \quad (6.7)$$

$$\bar{\phi}'' + 3\frac{a'}{a}\bar{\phi}' + \epsilon \frac{\partial \bar{V}(\bar{\phi})}{\partial \bar{\phi}} = 0 \quad (6.8)$$

respectively, where the prime denotes differentiation with respect to \bar{t} . The numerical solution of the system then becomes straightforward, starting from the following initial conditions as \bar{t} approaches $\bar{t}_i \simeq 0$.

$$a(\bar{t}_i) = \left(\frac{9}{4} \Omega_{0m} \right)^{1/3} \bar{t}_i^{2/3} \quad (6.9a)$$

$$\bar{\phi}(\bar{t}_i) = \bar{\phi}_i = \bar{\phi}_t + ns \quad (6.9b)$$

$$\bar{\phi}'(\bar{t}_i) = 0 \quad (6.9c)$$

Given that the universe is predominantly matter dominated in its early stages, and considering an inflationary phase, the expansion during this phase would significantly stretch out any variations and motion in the scalar field. Additionally, the strong cosmic damping effect essentially freezes the scalar field in its initial state [82]. For potentials with the same amplitude, the initial value of the field $\bar{\phi}_i$ impacts the speed of the transition. Specifically, a larger value of $\bar{\phi}_i$ allows the scalar field to gain more kinetic energy as it approaches the edge of the potential, resulting in a faster transition.

6.3.1 Qualitative behavior

As the universe expands, the Hubble parameter $H(\bar{t})$ decreases, initiating motion of the field. In the quintessence model, $\bar{\phi}$ starts rolling down the potential, while in the phantom model, it climbs up, as discussed in Section 4.2. As expected, the kinetic energy gained by the scalar field influences its equation of state, resulting in a spike that temporarily increases the value of $w(z)$. As can be seen in Figure 6.1, when the transition ends, and the field freezes once again due to cosmic friction, $w(z)$ returns to -1 , resembling a cosmological constant.

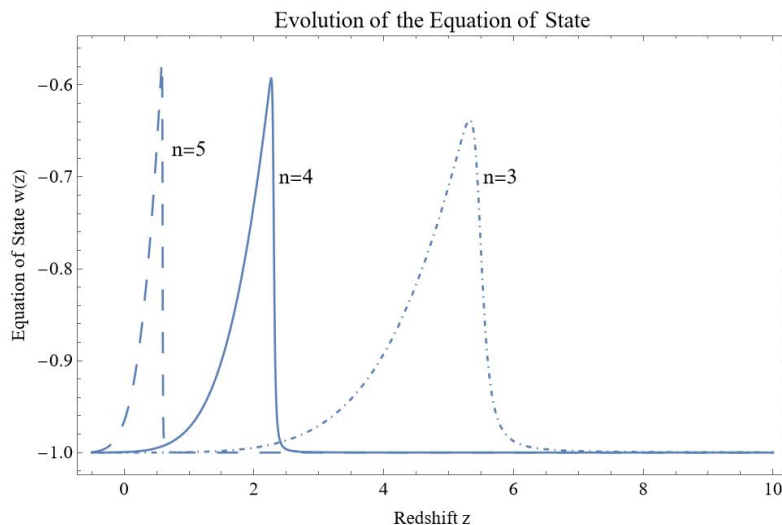


Figure 6.1: The EoS parameter for quintessence with $\Delta V = 0.1$, $\phi_t = 2$ and $s = 0.001$. Each line represents a different initial value of the field, leading to variations in speed and z_t .

Similarly to the EoS parameter, $H(z)$ initially resembles that of the standard Λ CDM model. In the early stages, the two models are indistinguishable, as matter

dominates the dynamics of the universe. However, as the transition begins, a subtle divergence in the slope of the Hubble parameter becomes evident, indicating the influence of the scalar field. As the field evolves, its presence modifies the dynamics of the universe, leading to a noticeable difference in $H(z)$. In the quintessence scenario, $\Omega_{\bar{\phi}}$ initially exceeds Ω_{Λ} , implying a larger effective cosmological constant and consequently a higher value of $H(z)$. By the end of the transition, the scalar field has dissipated its excess energy and can closely approximate the standard cosmological constant. Since $D_M(z_{ls})$ must remain consistent with the Λ CDM model, the quintessence scenario results in a lower value for the Hubble constant. This discrepancy leads to an exacerbation of the H_0 tension, as the predicted value of H_0 is now reduced compared to the measurements obtained from local observations. As shown in Figure 6.2, a larger initial value of the scalar field induces a more pronounced change, as the transition occurs more rapidly.

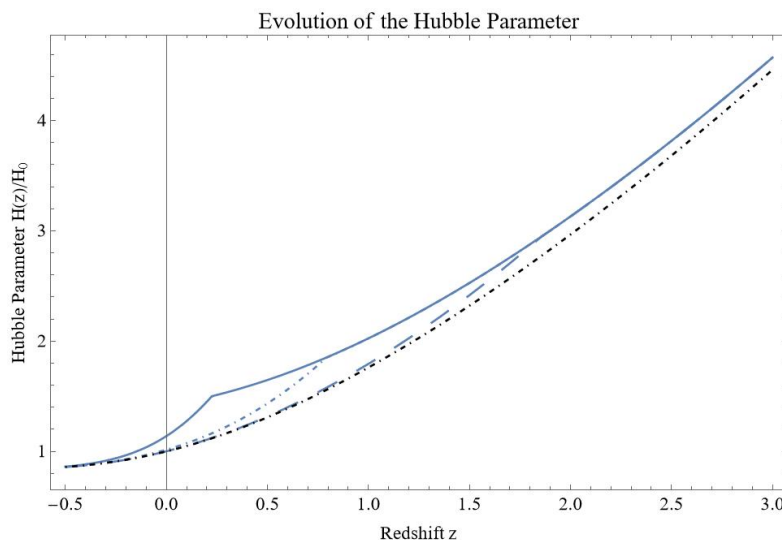


Figure 6.2: The Hubble parameter in the quintessence case with $\Delta V = 0.5$, $s = 0.001$ and $n = 5$ (dashed line), $n = 5.6$ (dot-dashed line) and $n = 6$ (thick line). The dot-dashed black line represents the Λ CDM.

Despite the continuity of $H(z)$, the deceleration parameter $q(z)$ exhibits a sudden change in value at z_t . Once again, the speed of the transition plays a significant role in this sharp change. A faster transition results in a sharper change in $q(z)$. As illustrated in Figure 6.3, it is important to note that the transition redshift does not necessarily coincide with the redshift at which the universe enters the acceleration phase.

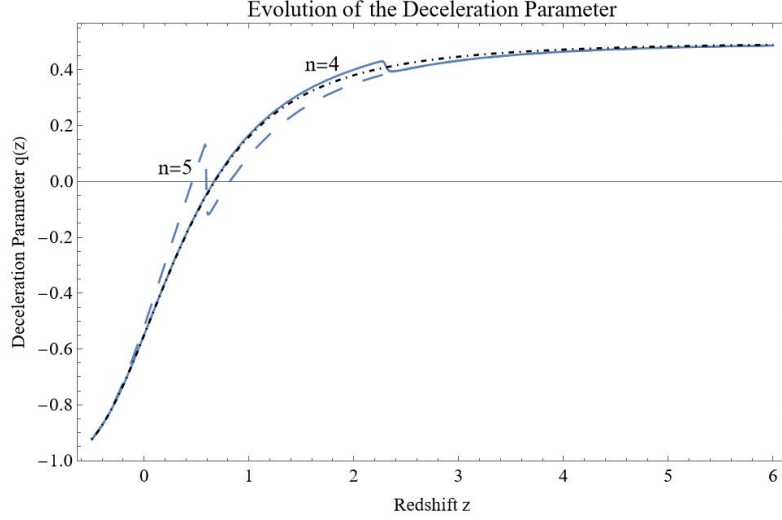


Figure 6.3: The deceleration parameter in the quintessence case with $\Delta V = 0.1$, $s = 0.001$ and $n = 5$ (dashed line) and $n = 4$ (thick line). The dot-dashed black line represents the Λ CDM.

As mentioned earlier, in contrast with quintessence, phantom fields violate the dominant energy condition, allowing for negative energy density. This enables a scalar field with $-\Omega_{0\bar{\phi}}$ in the past and $\Omega_{0\bar{\phi}}$ in the present (see Figure 6.4), which can be utilized in effort to reproduce the Λ_s CDM model and connect it with the scalar field theory. The field's EOS initially behaves like a cosmological constant, until the transition begins. At the redshift where the energy density parameter of the scalar field becomes zero, $w(z)$ exhibits a pole. However, the effective EOS parameter of the universe remains continuous throughout its entire evolution (see Figure 6.6). In cases where the amplitude of the potential is such that the energy density of the field does not change sign, the EOS parameter remains continuous and only decreases, appearing a spike, during the transition period (see Figure 6.5). Similar to Figure 6.1, we observe that the return of $w(z)$ to -1 is smoother than its initial deviation from it. This smoother return can be attributed to the field freezing more gradually than it initially gains kinetic energy, as our analysis considers a rather steep potential ($s = 0.001$).

In the phantom case, as well as with the quintessence field, no discontinuity is observed in the Hubble parameter $H(z)$. Instead, once again, a change in slope is evident. This time, as the field begins to influence the universe's dynamics, the deviation from the Λ CDM case is observed to be initially from below. This is because the effective cosmological constant is smaller and increases as the field evolves (see Figure 6.4). The most interesting aspect of this case is that the

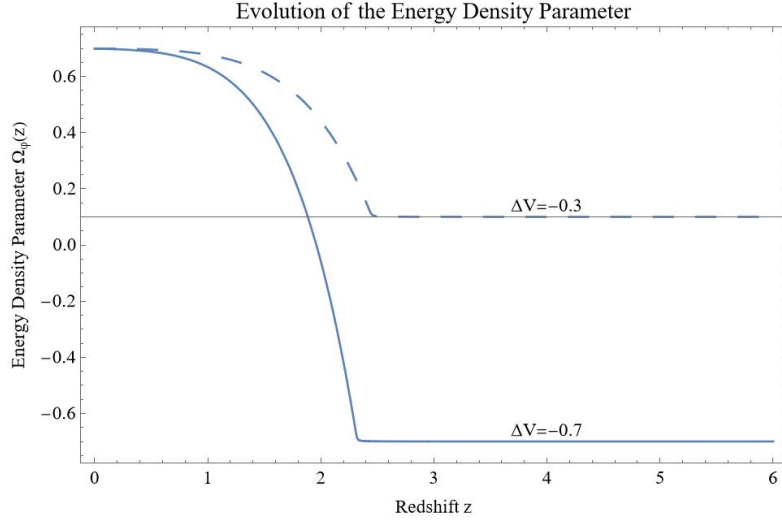


Figure 6.4: Energy density parameter for phantom field with transition redshift $z_t = 2.32$ (thick line) and $z_t = 2.45$ (dashed line).

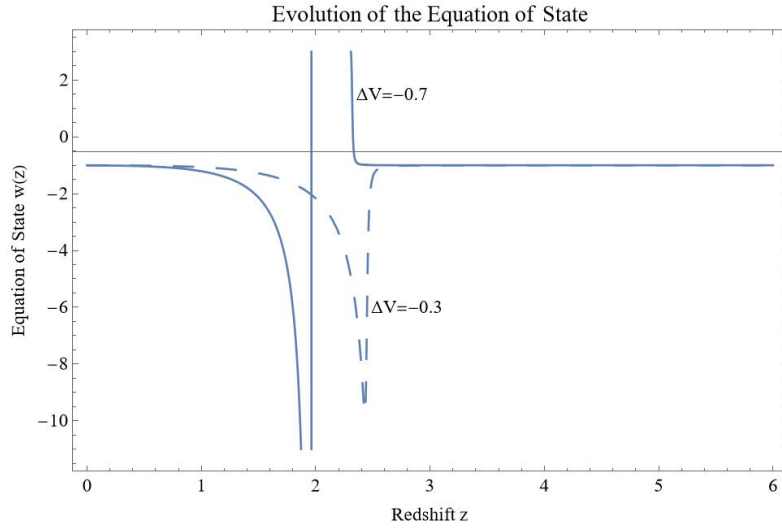


Figure 6.5: EoS parameter for a phantom field whose energy density changes sign (thick line) and another that does not (dashed line).

Hubble parameter surpasses that of Λ CDM, a fundamental characteristic of the Λ_s CDM model. However, we do not observe the discontinuity that is supposed in the abrupt Λ_s CDM. This is due to the presence of the kinetic term. Instead of the energy density parameter of the field jumping instantaneously from $-\Omega_{0\bar{\phi}}$ to $\Omega_{0\bar{\phi}}$, it evolves gradually over a short time period. In Figures 6.7 and 6.8, our

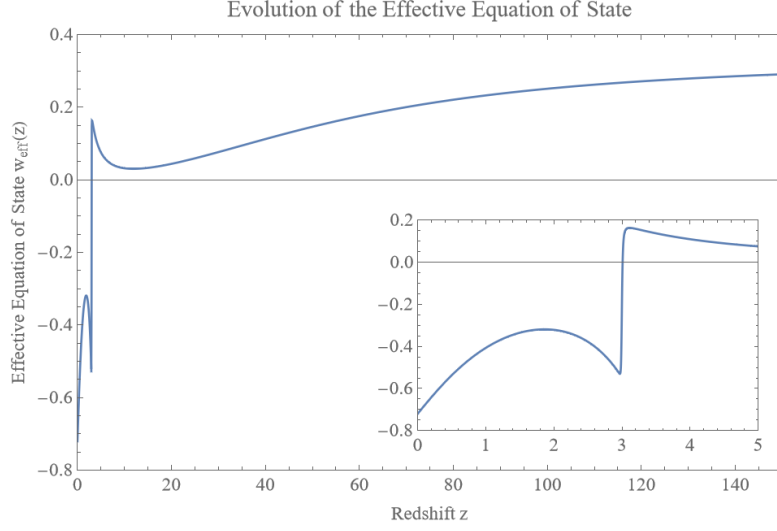


Figure 6.6: The effective EoS parameter in the case of a phantom field with $\Delta V = -0.7$, $s = 0.001$ and $z_t = 3.00$.

model employs $h = 0.7304$ and $\Omega_{0m} = 0.2652$, ensuring that the matter density parameter combination ω_m is consistent with the latest value of that of CMB [50].

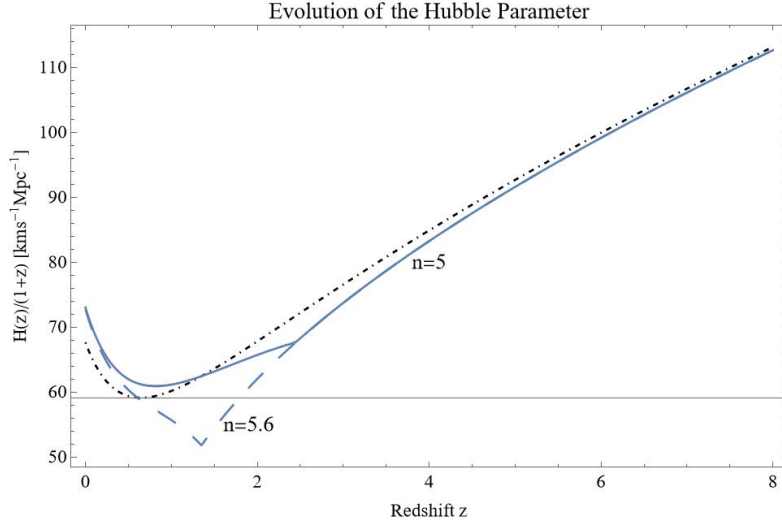


Figure 6.7: The Hubble parameter in the case of a phantom field with $\Delta V = -0.7$ and $s = 0.001$. The dot-dashed black line represents the Λ CDM.

As for the deceleration parameter, once again, a sudden drop in its value occurs at the transition redshift z_t . Approximately, what was applicable in the

quintessence field regarding the transition speed and redshift also applies here. Interestingly, for appropriate values of n and ΔV (thick line in Figure 6.8), the behavior of the deceleration parameter somewhat resembles that of the best fit abrupt Λ_s CDM's deceleration parameter.

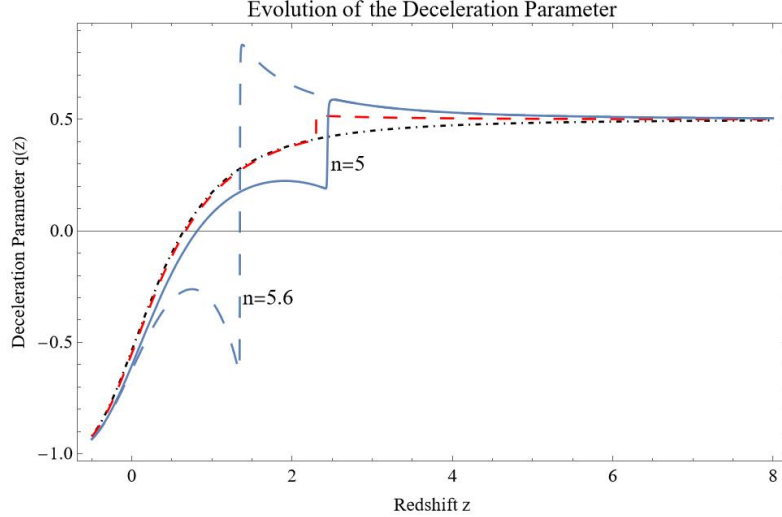


Figure 6.8: The deceleration parameter for phantom field with $\Delta V = -0.7$ and $s = 0.001$. The dot-dashed black line represents the Λ CDM, while the dashed red line represents the Λ_s CDM with a transition at $z_t = 2.3$.

Through this analysis, we observe that the proposed model of a phantom field evolving under a step-like potential shares several key features with the abrupt Λ_s CDM model. The most notable distinction lies in the continuous nature of the Hubble parameter in our model, which remains smooth even at the redshift where the energy density of the scalar field changes sign. This smooth transition contrasts with the discontinuous behavior of the Hubble parameter observed in the abrupt Λ_s CDM.

To evaluate whether this model can serve as a viable candidate for dark energy, a comprehensive statistical analysis is required. While such an analysis was attempted within the scope of this thesis, the results remain uncertain and require further verification.

6.3.2 Statistical analysis

In this subsection, we apply the χ^2 method to assess the fit of the step-like potential model to a combination of datasets, including CMB [124], BAO [73, 125], and Pantheon+⁵. The focus is on examining how well the model parameters align with the available observational constraints. To perform this analysis, we compute the individual χ^2 values for each dataset and their contributions to the total χ^2_{tot} . In this analysis, we systematically vary key parameters to explore its compatibility with observational data. The parameters considered include h , s , and ϕ_i . The parameter ϕ_i is of particular importance, as it determines the transition redshift z_t . Different initial values of the scalar field result in variations in the timing of this transition, which significantly influences the model’s predictions.

To ensure consistency with the CMB constraints, Ω_{0r} and Ω_{0m} are not treated as independent free parameters. Instead, they are constrained to satisfy the observed matter and radiation density parameter combination, ensuring that the background cosmology remains consistent with established measurements.

In the case of the Λ CDM model, the χ^2 function was minimized for individual datasets as well as for their combined dataset, with the results and corresponding 1σ uncertainties presented in Table 6.1. However, for the proposed model, this method could not be directly applied, as the free parameters needed to be fixed in order to solve the system of differential equations. Therefore, as previously noted, we varied the key parameters in the analysis. Specifically, the transition redshift z_t was varied between 1.00 and 3.00, with a step size of 0.25, the width of the potential s was tested for the values 0.001, 0.01, and 0.05, and the Hubble constant H_0 was considered in the range from $67.04 \text{ km s}^{-1} \text{ Mpc}^{-1}$ to $73.04 \text{ km s}^{-1} \text{ Mpc}^{-1}$ with unit steps. For each parameter combination, the χ^2 function was minimized to determine the absolute magnitude of SNIa, M_B . Notably, M_B did not require fixing to solve the ODEs. The best-fit results, along with the best-fit values of the standard cosmological model for comparison, are provided in Table 6.1.

As observed, our model performs better with a more abrupt potential. However, for the Pantheon+ dataset, the best fit was achieved with a value of $s = 0.01$, in contrast to $s = 0.001$, which was favored for the other datasets. In all variations of the parameters, the SNIa data consistently preferred the largest possible value of z_t . The effect of the parameter s on the model’s fit was not particularly significant; for a given value of z_t , different values of s resulted in nearly identical χ^2_{SN} values. For instance, for $z_t = 3.00$, $s = 0.001$ yielded $\chi^2_{SN} = 1539.42$, while for $s = 0.05$,

⁵The Pantheon+ dataset used in this study was obtained from [Pantheon+ Data Release](#).

Λ CDM				
	Pantheon+	BAO	CMB	Combined
Ω_{0m}	0.33 ± 0.02	0.29 ± 0.03	0.32 ± 0.01	0.31 ± 0.01
h	0.7347 ± 0.0101	0.6467 ± 0.0153	0.6709 ± 0.0049	0.6755 ± 0.0035
M_B	-19.248 ± 0.029	—	—	-19.435 ± 0.010
χ^2	1522.98	4.05	0.57	1573.91
Scalar Field Model				
	Pantheon+	BAO	CMB	Combined
Ω_{0m}	0.27	0.30	0.28	0.28
h	0.7204	0.6904	0.7104	0.7104
z_t	3.00	3.00	3.00	3.00
s	0.01	0.001	0.001	0.001
M_B	-19.310 ± 0.004	—	—	-19.338 ± 0.004
χ^2	1539.40	3.67	12.26	1562.47

Table 6.1: Comparison of the best-fit parameters for Λ CDM and the scalar field model with a step-like potential across different datasets.

$\chi^2_{SN} = 1540.19$. In the case of the CMB data, the parameter s had a more pronounced impact. Since our model does not alter the early universe dynamics, the comoving sound horizon at the drag and decoupling redshifts is constrained by the Planck results [75]. However, the fact that this data favored larger values of H_0 raises concerns about the reliability of these results.

The proposed model is more complex than the Λ CDM model and involves a different number of free parameters. For this reason, the χ^2 value alone is insufficient to determine whether the model is preferred. It is essential to evaluate whether the additional complexity introduced by the scalar field model is statistically justified. This can be done by employing criteria such as the Akaike Information Criterion (AIC) [126] or the Bayesian Information Criterion (BIC) [127]. These criteria are defined as [116, 128]

$$\text{AIC} = \chi^2_{min} + 2k \quad (6.10)$$

$$\text{BIC} = \chi^2_{min} + k \ln N, \quad (6.11)$$

where k is the number of free parameters and N represents the number of data points used ($N = 1713$). To draw conclusions, we compute the differences in AIC and BIC between the two models, given by

$$\Delta\text{AIC} = \Delta\chi^2 + 2\Delta k \quad (6.12)$$

$$\Delta\text{BIC} = \Delta\chi^2 + \Delta k \ln N. \quad (6.13)$$

A positive value favors the Λ CDM model, while a negative value indicates a preference for the proposed model. The magnitude of the difference quantifies the strength of the evidence: values in the range $[0, 2)$ signify an insignificant difference between the two models, values in the range $[2, 6)$ reflect moderate evidence, values in the range $[6, 10)$ provide strong evidence, and values greater than 10 indicate very strong evidence in favor of one model over the other [128].

The AIC ($\Delta\text{AIC} = -9.44$) strongly favors our model, whereas the BIC ($\Delta\text{BIC} = -4.00$) provides only moderate evidence in its favor. The discrepancy arises because the BIC imposes a stricter penalty for the inclusion of additional parameters, particularly when analyzing large datasets. This result suggests that while the proposed model significantly enhances the fit to the observational data, the additional parameters are not as strongly justified from the perspective of the BIC. Nevertheless, the agreement between both criteria highlights the robustness of the proposed model in addressing cosmological tensions, such as the Hubble tension, while offering a compelling extension to Λ CDM.

	z_t		
h	$s = 0.001$	$s = 0.01$	$s = 0.05$
0.7304	2.16	2.13	2.12
0.7204	2.30	2.29	2.31
0.7104	2.56	2.50	2.55
0.7004	2.89	2.93	3.15
0.6904	3.60	3.62	4.18
0.6804	4.95	5.35	—
0.6704	—	—	—

Table 6.2: The value of z_t for each h , ensuring that $D_M(z_{ls})$ matches that of the Λ CDM model.

Finally, for the case where $h = 0.7104$, $s = 0.001$, and $z_t = 3.00$, the model

achieves the best fit to the observational data. However, $D_M(z_{ls})$ deviates by 0.31% from the corresponding value predicted by the standard Λ CDM model. Additionally, the absolute magnitude of SNIa is determined to be $M_B = -19.338 \pm 0.004$ mag., which shows a 3.1σ tension with the value $M_B^{R22} = -19.253 \pm 0.027$ mag. reported in [129]. If $D_M(z_{ls})$ is constrained to match the Λ CDM value (see Table 6.2), the fit to the observational data deteriorates significantly. This result highlights the inherent difficulty in simultaneously achieving consistency with both $D_M(z_{ls})$ and M_B .

As a final test, the age of the universe was calculated for the best-fit case, resulting in $t_{un} = 13.611$ Gyr. Although we were unable to obtain uncertainty limits for a more accurate comparison, this value is in agreement with the age determined from the oldest globular clusters, falling within their upper uncertainty bound.

Conclusions

In this thesis, we employed the framework of dynamical systems to analyze two non-interacting quintessence models: one with a self-interacting potential of exponential form and the other with an inverse power-law potential. Our analysis demonstrated the utility of dynamical systems theory as a powerful tool for gaining qualitative insights into the behavior of cosmological models. Our findings indicate that the exponential potential model is unable to account for the observed acceleration, as its solutions lack the required dynamics to drive late-time cosmic acceleration. In contrast, the inverse power-law model exhibits tracker behavior, a feature that allows it to potentially alleviate the fine-tuning problem associated with initial conditions. However, a significant discrepancy remains between the theoretical constraints on the parameter α and those derived from observational data, highlighting the challenges of aligning such models with empirical evidence. Additionally, the ultra-light mass of the scalar field required in these models poses a fundamental challenge, as it conflicts with the energy scales typically associated with particle physics. Despite the existence of viable quintessence models [104, 130–132], none have yet been able to offer a compelling alternative to the Λ CDM model.

A significant competitor to the Λ CDM model is the Λ_s CDM model, which introduces a step-like modification to the cosmological constant, allowing it to transition between two distinct values at a specific redshift. This model has demonstrated excellent statistical performance and offers solutions to several cosmological tensions that the standard Λ CDM model struggles to address. These include the age of the universe, the Hubble constant (H_0), the absolute magnitude of SNIa (M_B), and the S_8 tension. Despite its success, the lack of a concrete physical mechanism underlying this model remains a critical limitation. In the second part of this thesis, we aimed to address this limitation by introducing a phantom scalar field with a tanh self-interacting potential. This approach yielded a model characterized by a smooth transition in the Hubble parameter, even at the redshift where the scalar field's energy density changes sign. This feature contrasts with the abrupt transitions of the original Λ_s CDM model, offering a more physically

motivated alternative.

Statistical analyses, including χ^2 fitting and model comparison criteria such as AIC and BIC, indicated that the proposed model could offer a better fit in certain scenarios. Additionally, the calculated age of the universe in this model aligns with the age derived from the oldest globular clusters, further supporting its consistency with observational data. However, the inclusion of additional parameters introduces complexity, which is statistically justified under specific conditions. Despite these advantages, the model exhibits challenges: at the best-fit values, the comoving angular diameter distance to the last scattering surface deviates by approximately 0.3%, and the absolute magnitude of supernovae (M_B) shows a 3.1σ discrepancy with the value obtained from Cepheid measurements.

The proposed model opens several avenues for further exploration. First, a more precise statistical analysis should be conducted using the latest available datasets. These refined analyses would allow for a better determination of the model's parameters and provide a clearer assessment of its compatibility with observational constraints. Moreover, it is crucial to investigate how this model aligns with the processes of structure formation and the growth of perturbations. Specifically, exploring the impact of the phantom field's dynamics on the matter power spectrum and weak lensing observables could yield valuable insights into its viability.

Appendix A

Derivation of Friedmann Equations

A.1 Einstein field equations

The Einstein field equations can be derived using the stationary-action principle, also known as the principle of least action. The action that describes General Relativity is the Einstein-Hilbert action, which is expressed as

$$S_{EH} = \frac{1}{2\kappa^2} \int d^4x \sqrt{-g} (R - 2\Lambda), \quad (\text{A.1})$$

where Λ is the cosmological constant and g is the determinant of the metric $g_{\mu\nu}$. The total action of the theory includes the matter fields and has the form

$$S = S_{EH} + S_m = \frac{1}{2\kappa^2} \int d^4x \sqrt{-g} (R - 2\Lambda) + S_m, \quad (\text{A.2})$$

where S_m represents the action of the matter fields.

We consider an arbitrary variation in the metric tensor given by

$$g_{\mu\nu} \rightarrow g_{\mu\nu} + \delta g_{\mu\nu}. \quad (\text{A.3})$$

where $\delta g_{\mu\nu}$ and its first derivative vanish on the boundary.

By varying (A.2) with respect to the metric $g_{\mu\nu}$, we obtain

$$\delta S = \delta S_{EH} + \delta S_m = \frac{1}{2\kappa^2} \int d^4x [\delta \sqrt{-g} (R - 2\Lambda) + \sqrt{-g} \delta R] + \delta S_m. \quad (\text{A.4})$$

Without considering the cosmological background, the metric is a symmetric tensor and, according to the spectral theorem, it can be diagonalized. Therefore, applies the relation

$$\ln g = \text{tr}(\ln g_{\mu\nu}) \xrightarrow[\text{w.r.t. } g_{\mu\nu}]{\text{variation}} \frac{\delta g}{g} = \frac{\delta g_{\mu\nu}}{g_{\mu\nu}} = g^{\mu\nu} \delta g_{\mu\nu}. \quad (\text{A.5})$$

Thus,

$$\delta\sqrt{-g} = \frac{-\delta g}{2\sqrt{-g}} = \frac{1}{2\sqrt{-g}} (-g) g^{\mu\nu} \delta g_{\mu\nu} = \frac{1}{2} \sqrt{-g} g^{\mu\nu} \delta g_{\mu\nu}, \quad (\text{A.6})$$

where we used (A.5) to substitute δg .

The variation of the Ricci scalar involves the variation of the Ricci tensor $R_{\mu\nu}$, which is a contraction of the Riemann tensor $R^\rho{}_{\mu\nu\sigma}$. The Riemann tensor, in turn, is a function of the metric tensor and its first and second derivatives.

$$\delta R = \delta(g^{\mu\nu} R_{\mu\nu}) = (\delta g^{\mu\nu}) R_{\mu\nu} + g^{\mu\nu} (\delta R_{\mu\nu}) \quad (\text{A.7})$$

$$R_{\mu\nu} \equiv R^\alpha{}_{\mu\nu\alpha} = \partial_\nu \Gamma^\alpha{}_{\mu\alpha} - \partial_\alpha \Gamma^\alpha{}_{\mu\nu} + \Gamma^\tau{}_{\mu\alpha} \Gamma^\alpha{}_{\tau\nu} - \Gamma^\tau{}_{\mu\nu} \Gamma^\alpha{}_{\tau\alpha} \quad (\text{A.8})$$

$\Gamma^\alpha{}_{\mu\nu}$ are the so-called Christoffel symbols (of the second kind), also referred to as the affine connection¹. They describe changes in basis vectors throughout a given coordinate system and can be associated with the metric tensor as

$$\Gamma^\alpha{}_{\mu\nu} = \frac{1}{2} g^{\alpha\rho} (\partial_\mu g_{\rho\nu} + \partial_\nu g_{\mu\rho} - \partial_\rho g_{\mu\nu}). \quad (\text{A.9})$$

As observed from equation (A.8), a variation in the Ricci tensor arises from a variation in the Christoffel symbols. Consequently, we consider an arbitrary variation in the affine connection

$$\Gamma^\alpha{}_{\mu\nu} \rightarrow \Gamma^\alpha{}_{\mu\nu} + \delta\Gamma^\alpha{}_{\mu\nu}. \quad (\text{A.10})$$

It is essential to note that the Christoffel symbols are not tensors, as they do not adhere to tensor transformation laws. However, $\delta\Gamma^\alpha{}_{\mu\nu}$ constitutes a tensor, given that it is the difference between two connections. In this case, the non-tensorial inhomogeneous terms in the coordinate transformation cancel out.

The variation of equation (A.8) yields

$$\delta R_{\mu\nu} = \partial_\nu (\delta\Gamma^\alpha{}_{\mu\alpha}) - \partial_\alpha (\delta\Gamma^\alpha{}_{\mu\nu}) + (\delta\Gamma^\tau{}_{\mu\alpha}) \Gamma^\alpha{}_{\tau\nu} + \Gamma^\tau{}_{\mu\alpha} (\delta\Gamma^\alpha{}_{\tau\nu}) - (\delta\Gamma^\tau{}_{\mu\nu}) \Gamma^\alpha{}_{\tau\alpha} - \Gamma^\tau{}_{\mu\nu} (\delta\Gamma^\alpha{}_{\tau\alpha}). \quad (\text{A.11})$$

¹Throughout our discussion we assume a torsionless spacetime, where $\Gamma^\alpha{}_{\mu\nu}$ is symmetric in its last two indices, i.e., $\Gamma^\alpha{}_{\mu\nu} = \Gamma^\alpha{}_{\nu\mu}$.

Given that (A.11) represents a tensor identity, it is advantageous to work in local geodesic coordinates by considering an arbitrary point P at which $\Gamma^\alpha_{\mu\nu}(P) = 0$. In the vicinity of this point, partial derivatives coincide with covariant derivatives. Consequently, at this point,

$$\delta R_{\mu\nu} = \nabla_\nu (\delta \Gamma^\alpha_{\mu\alpha}) - \nabla_\alpha (\delta \Gamma^\alpha_{\mu\nu}). \quad (\text{A.12})$$

Since (A.12) is a tensor identity and P is an arbitrary point, this relation holds true in any coordinate system.

The last necessary relation is

$$g^{\mu\nu} g_{\mu\nu} = \delta^\mu_\mu \xrightarrow[\text{w.r.t. } g_{\mu\nu}]{\text{variation}} (\delta g^{\mu\nu}) g_{\mu\nu} + g^{\mu\nu} (\delta g_{\mu\nu}) = 0 \Rightarrow g^{\mu\nu} (\delta g_{\mu\nu}) = -(\delta g^{\mu\nu}) g_{\mu\nu}. \quad (\text{A.13})$$

Now, (A.4) takes the form

$$\begin{aligned} \delta S &= \frac{1}{2\kappa^2} \int dx^4 \left[-\frac{1}{2} \sqrt{-g} (\delta g^{\mu\nu}) g_{\mu\nu} (R - 2\Lambda) + \sqrt{-g} (\delta g^{\mu\nu}) R_{\mu\nu} \right] + \\ &\quad \frac{1}{2\kappa^2} \int dx^4 \sqrt{-g} g^{\mu\nu} [\nabla_\nu (\delta \Gamma^\alpha_{\mu\alpha}) - \nabla_\alpha (\delta \Gamma^\alpha_{\mu\nu})] + \delta S_m \xrightarrow[\text{relabelling}]{\nabla_\alpha g^{\beta\gamma} = 0} \\ \delta S &= \frac{1}{2\kappa^2} \int dx^4 \sqrt{-g} \left[-\frac{1}{2} g_{\mu\nu} (R - 2\Lambda) + R_{\mu\nu} \right] \delta g^{\mu\nu} + \\ &\quad \frac{1}{2\kappa^2} \int dx^4 \sqrt{-g} \nabla_\sigma (g^{\mu\sigma} \delta \Gamma^\alpha_{\mu\alpha} - g^{\mu\nu} \delta \Gamma^\sigma_{\mu\nu}) + \delta S_m. \end{aligned} \quad (\text{A.14})$$

According to the divergence theorem, the second term corresponds to a surface integral. However, this integral vanishes because we have assumed that $\delta g_{\mu\nu}$ and its first derivative are zero on the boundary. Generally, we may be interested in what happens on the boundary. In such cases, we cannot make the previous assumption; instead, we include an additional term in the action, such as the Gibbons-Hawking-York (GHY) boundary term, which cancels out the resulting surface term.

As noted at the beginning of this section, the derivation follows from the principle of least action, hence $\delta S = 0$.

$$\begin{aligned} \frac{1}{2\kappa^2} \int dx^4 \sqrt{-g} \left[-\frac{1}{2} g_{\mu\nu} (R - 2\Lambda) + R_{\mu\nu} \right] \delta g^{\mu\nu} + \delta S_m &= 0 \Rightarrow \\ \frac{1}{2\kappa^2} \int dx^4 \sqrt{-g} \left[-\frac{1}{2} g_{\mu\nu} (R - 2\Lambda) + R_{\mu\nu} \right] \delta g^{\mu\nu} &= - \int dx^4 \frac{\delta \mathcal{L}_m}{\delta g^{\mu\nu}} \delta g^{\mu\nu}. \end{aligned} \quad (\text{A.15})$$

Considering that the variation $\delta g^{\mu\nu}$ is arbitrary, we obtain

$$\begin{aligned} \frac{1}{2\kappa^2} \sqrt{-g} \left[-\frac{1}{2} g_{\mu\nu} (R - 2\Lambda) + R_{\mu\nu} \right] &= -\frac{\delta \mathcal{L}_m}{\delta g^{\mu\nu}} \Rightarrow \\ -\frac{1}{2} g_{\mu\nu} (R - 2\Lambda) + R_{\mu\nu} &= -\kappa^2 \frac{2}{\sqrt{-g}} \frac{\delta \mathcal{L}_m}{\delta g^{\mu\nu}}. \end{aligned} \quad (\text{A.16})$$

The final step needed to recover the Einstein field equations is to define the matter energy-momentum tensor as

$$T_{\mu\nu} \equiv \frac{2}{\sqrt{-g}} \frac{\delta \mathcal{L}_m}{\delta g^{\mu\nu}}. \quad (\text{A.17})$$

Using (A.16) and the definition given by (A.17), we attain the desired result

$$R_{\mu\nu} - \frac{1}{2} g_{\mu\nu} R + \Lambda g_{\mu\nu} = -\kappa^2 T_{\mu\nu}. \quad (\text{A.18})$$

To derive equation (2.7), it suffices to set $\Lambda = 0$.

A.2 Friedmann equations

As discussed in Section 2.3, the metric that describes the universe is the FLRW metric. Generally, the line element of a metric is given by

$$ds^2 = g_{\mu\nu} dx^\mu dx^\nu. \quad (\text{A.19})$$

Therefore, by combining equations (2.4) and (A.19), we can determine the covariant components of the FLRW metric $g_{\mu\nu}$ ² as

$$g_{00} = 1, \quad g_{11} = -a^2, \quad g_{22} = -a^2 r^2, \quad g_{33} = -a^2 r^2 \sin^2 \theta. \quad (\text{A.20})$$

Because the metric is diagonal, the contravariant components $g^{\mu\nu}$ are the reciprocals of the covariant components. Thus,

$$g^{00} = 1, \quad g^{11} = -a^{-2}, \quad g^{22} = -a^{-2} r^{-2}, \quad g^{33} = -a^{-2} r^{-2} \sin^{-2} \theta. \quad (\text{A.21})$$

To solve Einstein's field equations, the first step is to compute the Christoffel symbols as given by equation (A.9).

²Wherever a is used, it specifically denotes $a(t)$

- $\Gamma^\sigma_{\sigma\sigma} = \frac{1}{2} g^{\sigma\rho} (\partial_\sigma g_{\rho\sigma} + \partial_\sigma g_{\sigma\rho} - \partial_\rho g_{\sigma\sigma}) \xrightarrow[\text{diagonal}]{g^{\mu\nu} \text{ is}} \Gamma^\sigma_{\sigma\sigma} = \frac{1}{2} g^{\sigma\sigma} \partial_\sigma g_{\sigma\sigma} = 0$
- $\Gamma^\alpha_{\mu\nu} = \frac{1}{2} g^{\alpha\rho} (\partial_\mu g_{\rho\nu} + \partial_\nu g_{\mu\rho} - \partial_\rho g_{\mu\nu}) \xrightarrow[\text{diagonal}]{g^{\mu\nu} \text{ is}} \Gamma^\alpha_{\mu\nu} = 0 \quad (\alpha \neq \mu \neq \nu)$
- $\Gamma^\alpha_{\nu\nu} = \frac{1}{2} g^{\alpha\rho} (\partial_\nu g_{\rho\nu} + \partial_\nu g_{\nu\rho} - \partial_\rho g_{\nu\nu}) \xrightarrow[\text{diagonal}]{g^{\mu\nu} \text{ is}} \Gamma^\alpha_{\nu\nu} = -\frac{1}{2} g^{\alpha\alpha} \partial_\alpha g_{\nu\nu} \quad (\alpha \neq \nu)$
- $\Gamma^\mu_{\mu\nu} = \frac{1}{2} g^{\mu\rho} (\partial_\mu g_{\rho\nu} + \partial_\nu g_{\mu\rho} - \partial_\rho g_{\mu\nu}) \xrightarrow[\text{diagonal}]{g^{\mu\nu} \text{ is}} \Gamma^\mu_{\mu\nu} = \frac{1}{2} g^{\mu\mu} \partial_\nu g_{\mu\mu} \quad (\mu \neq \nu)$

So, there are only 12 non-vanishing Christoffel symbols.

1. $\Gamma^0_{11} = -\frac{1}{2} g^{00} \partial_0 g_{11} = -\frac{1}{2} \partial_t (-a^2) = a\dot{a}$
2. $\Gamma^0_{22} = -\frac{1}{2} g^{00} \partial_0 g_{22} = -\frac{1}{2} \partial_t (-a^2 r^2) = a\dot{a} r^2$
3. $\Gamma^0_{33} = -\frac{1}{2} g^{00} \partial_0 g_{33} = -\frac{1}{2} \partial_t (-a^2 r^2 \sin^2 \theta) = a\dot{a} r^2 \sin^2 \theta$
4. $\Gamma^1_{22} = -\frac{1}{2} g^{11} \partial_1 g_{22} = -\frac{1}{2} (-a^{-2}) \partial_r (-a^2 r^2) = -r$
5. $\Gamma^1_{33} = -\frac{1}{2} g^{11} \partial_1 g_{33} = -\frac{1}{2} (-a^{-2}) \partial_r (-a^2 r^2 \sin^2 \theta) = -r \sin^2 \theta$
6. $\Gamma^2_{33} = -\frac{1}{2} g^{22} \partial_2 g_{33} = -\frac{1}{2} (-a^{-2} r^{-2}) \partial_\theta (-a^2 r^2 \sin^2 \theta) = -\sin \theta \cos \theta$
7. $\Gamma^1_{10} = \frac{1}{2} g^{11} \partial_0 g_{11} = \frac{1}{2} (-a^{-2}) \partial_t (-a^2) = \frac{\dot{a}}{a}$
8. $\Gamma^2_{20} = \frac{1}{2} g^{22} \partial_0 g_{22} = \frac{1}{2} (-a^{-2} r^{-2}) \partial_t (-a^2 r^2) = \frac{\dot{a}}{a}$
9. $\Gamma^3_{30} = \frac{1}{2} g^{33} \partial_0 g_{33} = \frac{1}{2} (-a^{-2} r^{-2} \sin^{-2} \theta) \partial_t (-a^2 r^2 \sin^2 \theta) = \frac{\dot{a}}{a}$
10. $\Gamma^2_{21} = \frac{1}{2} g^{22} \partial_1 g_{22} = \frac{1}{2} (-a^{-2} r^{-2}) \partial_r (-a^2 r^2) = \frac{1}{r}$
11. $\Gamma^3_{31} = \frac{1}{2} g^{33} \partial_1 g_{33} = \frac{1}{2} (-a^{-2} r^{-2} \sin^{-2} \theta) \partial_r (-a^2 r^2 \sin^2 \theta) = \frac{1}{r}$
12. $\Gamma^3_{32} = \frac{1}{2} g^{33} \partial_2 g_{33} = \frac{1}{2} (-a^{-2} r^{-2} \sin^{-2} \theta) \partial_\theta (-a^2 r^2 \sin^2 \theta) = \frac{\cos \theta}{\sin \theta}$

Moreover, we need to compute the non-zero components of the Ricci tensor, as given by equation (A.8), along with the Ricci scalar. For brevity, detailed mathematical operations will be omitted as they are beyond the scope of this discussion. Therefore, we have

$$R_{00} = 3\frac{\ddot{a}}{a}, \quad R_{11} = -a\ddot{a} - 2\dot{a}^2, \quad R_{22} = -r^2 (a\ddot{a} + 2\dot{a}^2), \quad R_{33} = -r^2 \sin^2 \theta (a\ddot{a} + 2\dot{a}^2) \quad (\text{A.22})$$

$$\begin{aligned}
R &\equiv g^{\mu\nu} R_{\mu\nu} = g^{00} R_{00} + g^{11} R_{11} + g^{22} R_{22} + g^{33} R_{33} \\
&= 3 \frac{\ddot{a}}{a} + \frac{1}{a^2} (a\ddot{a} + 2\dot{a}^2) + \frac{1}{a^2 r^2} r^2 (a\ddot{a} + 2\dot{a}^2) + \frac{1}{a^2 r^2 \sin^2 \theta} r^2 \sin^2 \theta (a\ddot{a} + 2\dot{a}^2) \\
&= 6 \frac{\ddot{a}}{a} + 6 \frac{\dot{a}^2}{a^2} = 6 \left(\frac{\ddot{a}}{a} + \frac{\dot{a}^2}{a^2} \right)
\end{aligned} \tag{A.23}$$

With equations (A.20), (A.22), and (A.23), we have all the necessary components to determine the left-hand side of the field equations (A.18). To complete the right-hand side, we need to determine the covariant components of the fluid's energy-momentum tensor. According to Section 2.3, $T_{\mu\nu}$ can be approximated as that of a perfect fluid, and its form is given by equation (2.5). Consequently,

$$T_{00} = \rho, \quad T_{ii} = -p g_{ii} \tag{A.24}$$

Now we have everything required to derive the Friedmann equations from the Einstein field equations.

For $\mu = \nu = 0$, (A.18) becomes

$$\begin{aligned}
R_{00} - \frac{1}{2} g_{00} R + \Lambda g_{00} &= -\kappa^2 T_{00} \Rightarrow 3 \frac{\ddot{a}}{a} - \frac{1}{2} 6 \left(\frac{\ddot{a}}{a} + \frac{\dot{a}^2}{a^2} \right) + \Lambda = -\kappa^2 \rho \\
&\Rightarrow \frac{\dot{a}^2}{a^2} = \frac{\kappa^2}{3} \rho + \frac{\Lambda}{3}.
\end{aligned} \tag{A.25}$$

This is the well-known first Friedmann equation.

All spatial components of (A.18) yield the same result, due to the homogeneity and isotropy; therefore, we will compute only the case for $\mu = \nu = 1$.

$$\begin{aligned}
R_{11} - \frac{1}{2} g_{11} R + \Lambda g_{11} &= -\kappa^2 T_{11} \Rightarrow -a\ddot{a} - 2\dot{a}^2 + \frac{1}{2} a^2 6 \left(\frac{\ddot{a}}{a} + \frac{\dot{a}^2}{a^2} \right) - \Lambda a^2 = -\kappa^2 a^2 p \\
&\Rightarrow 2 \frac{\ddot{a}}{a} + \frac{\dot{a}^2}{a^2} = -\kappa^2 p + \Lambda.
\end{aligned} \tag{A.26}$$

This is the second Friedmann equation.

However, by combining the Friedmann equations we can derive the Raychaudhuri equation, also known as the acceleration equation, given the fact that includes only the second derivative term of the scale factor. This equation can be expressed as

$$\frac{\ddot{a}}{a} = -\frac{\kappa^2}{6} (\rho + 3p) + \frac{\Lambda}{3}. \tag{A.27}$$

By setting $\Lambda = 0$ in equations (A.25), (A.26) and (A.27) we obtain equations (2.8), (2.9) and (2.10) respectively.

Taking into consideration that $H = \frac{\dot{a}}{a}$, equations (A.25) and (A.26) can be reformulated as

$$H^2 = \frac{\kappa^2}{3}\rho + \frac{\Lambda}{3} \quad (\text{A.28})$$

$$2\dot{H} + 3H^2 = -\kappa^2 p + \Lambda \quad (\text{A.29})$$

respectively. Combining equations (A.28) and (A.29) yields

$$\dot{H} = -\frac{\kappa^2}{2}(\rho + p). \quad (\text{A.30})$$

Appendix B

Center Manifold Theory with Inverse Power-Law Potential

In this appendix, we apply center manifold theory to the case of the inverse power-law potential in order to assess the stability of the non-hyperbolic fixed points C , D , and E .

B.1 Fixed point E

The first step is to shift the fixed point to the origin. For this purpose, we use the translation $\bar{y} = y - 1$. The system (5.19) becomes

$$x' = -\frac{3}{2}(1-z) [2x + x^3(w_b - 1) + x(1 + w_b)((\bar{y} + 1)^2 - 1)] + \sqrt{\frac{3}{2}}z(\bar{y} + 1)^2 \quad (\text{B.1a})$$

$$\bar{y}' = -\frac{3}{2}(1-z)(\bar{y} + 1) [x^2(w_b - 1) + (1 + w_b)((\bar{y} + 1)^2 - 1)] - \sqrt{\frac{3}{2}}zx(\bar{y} + 1) \quad (\text{B.1b})$$

$$z' = -\sqrt{6}z^2x(1-z)(\Gamma - 1) \quad (\text{B.1c})$$

Now, we need to find the similarity transformation T . Let M be a matrix with the eigenvectors of the Jacobian matrix as its columns. Then T will be the inverse of M .

$$M = \begin{pmatrix} 1 & \frac{1}{\sqrt{6}} & 0 \\ 0 & 0 & 1 \\ 0 & 1 & 0 \end{pmatrix}, \quad T = M^{-1} = \begin{pmatrix} 1 & 0 & -\frac{1}{\sqrt{6}} \\ 0 & 0 & 1 \\ 0 & 1 & 0 \end{pmatrix}$$

Changing the variables as

$$\begin{pmatrix} u \\ v \\ q \end{pmatrix} = T \begin{pmatrix} x \\ \bar{y} \\ z \end{pmatrix} = \begin{pmatrix} 1 & 0 & -\frac{1}{\sqrt{6}} \\ 0 & 0 & 1 \\ 0 & 1 & 0 \end{pmatrix} \begin{pmatrix} x \\ \bar{y} \\ z \end{pmatrix} = \begin{pmatrix} x - \frac{z}{\sqrt{6}} \\ z \\ \bar{y} \end{pmatrix},$$

yields the dynamical system

$$\begin{aligned} u' = & -3u + \sqrt{\frac{3}{2}}v(1+q)^2 + (1-v)v^2 \left(u + \frac{v}{\sqrt{6}}\right) (\Gamma - 1) + 3uv \\ & + \frac{3}{2}(1-v) \left[(1-w_b) \left(\left(u + \frac{v}{\sqrt{6}}\right)^3 - \frac{v}{\sqrt{6}} \right) - (1+w_b) \left((1+q)^2 \left(u + \frac{v}{\sqrt{6}}\right) - u \right) \right] \end{aligned} \quad (\text{B.2a})$$

$$v' = -\sqrt{6}(1-v)v^2 \left(u + \frac{v}{\sqrt{6}}\right) (\Gamma - 1) \quad (\text{B.2b})$$

$$\begin{aligned} q' = & -3(1+w_b) - \sqrt{\frac{3}{2}}v(1+q) \left(u + \frac{v}{\sqrt{6}}\right) \\ & - \frac{3}{2}(1+q)(1-v) \left(u + \frac{v}{\sqrt{6}}\right)^2 (w_b - 1) - \frac{3}{2}(1+w_b)q[-2v + (1-v)q(3+q)]. \end{aligned} \quad (\text{B.2c})$$

According to the center manifold theorem, there exists a center manifold for the system (B.2). Thus, we define $u = h_1(v)$ and $q = h_2(v)$ to represent this manifold. Using the approximation theorem, we can series expand $h_1(v)$ and $h_2(v)$. So,

$$h_1(v) = a_1v^2 + a_2v^3 + a_3v^4 + \mathcal{O}(|v|^5) \quad (\text{B.3})$$

$$h_2(v) = b_1v^2 + b_2v^3 + b_3v^4 + \mathcal{O}(|v|^5). \quad (\text{B.4})$$

Making the appropriate substitutions in equation (1.15), we obtain two quasilinear partial differential equations. These equations must hold true for every value of v . After solving for the coefficients, keeping terms up to the fourth power of v , we find the values to be

$$\begin{aligned} a_1 &= \frac{1}{\sqrt{6}}, & a_2 &= \frac{\Gamma+2}{3\sqrt{6}}, & a_3 &= \frac{\Gamma}{\sqrt{6}} \\ b_1 &= -\frac{1}{12}, & b_2 &= -\frac{1}{6}, & b_3 &= -\frac{57+16\Gamma}{288} \end{aligned}$$

Consequently,

$$u = h_1(v) = \frac{1}{\sqrt{6}}v^2 + \frac{\Gamma + 2}{3\sqrt{6}}v^3 + \frac{\Gamma}{\sqrt{6}}v^4 + \mathcal{O}(|v|^5) \quad (\text{B.5})$$

$$q = h_2(v) = -\frac{1}{12}v^2 - \frac{1}{6}v^3 - \frac{57 + 16\Gamma}{288}v^4 + \mathcal{O}(|v|^5). \quad (\text{B.6})$$

The form of the center manifold of E can be determined using (B.5) and (B.6). Now, the flow on the center manifold of the fixed point E can be studied by substituting (B.5) into (B.2b) which gives

$$v' = (1 - \Gamma)v^3 + \mathcal{O}(|v|^5). \quad (\text{B.7})$$

We are interested in the case where $\Gamma > 1$. Also, considering that $v = z$ and that our phase space is constrained to $z > 0$, we can conclude that the fixed point E is a stable node.

B.2 Fixed point C

Following the same procedure, we first need to transfer the fixed point to the origin. This is accomplished by using $\bar{x} = x + 1$. The system (5.19) takes the form

$$\begin{aligned} \bar{x}' = & 3(1 - w_b)\bar{x} + \sqrt{\frac{3}{2}}zy^2 + \\ & \frac{3}{2} [(\bar{x} - 1)((z - 1)y^2(w_b + 1) + z(1 - w_b)) + (w_b - 1)((\bar{x} - 1)^3z - \bar{x}^2(\bar{x} - 3))] \end{aligned} \quad (\text{B.8a})$$

$$\begin{aligned} y' = & 3y - \sqrt{\frac{3}{2}}yz(\bar{x} - 1) + \\ & \frac{3}{2}y [(w_b - 1)((\bar{x} - 1)^2(z - 1) + 1) + (w_b + 1)(y^2(z - 1) - z)] \end{aligned} \quad (\text{B.8b})$$

$$z' = -\sqrt{6}z^2(\bar{x} - 1)(1 - z)(\Gamma - 1) \quad (\text{B.8c})$$

Since the system (B.8) already has the desired form, we can apply the center manifold theorem, which states that the origin possesses a center manifold. From the approximation theorem, we can write

$$\bar{x} = h_1(z) = a_1z^2 + a_2z^3 + a_3z^4 + \mathcal{O}(|z|^5) \quad (\text{B.9})$$

$$y = h_2(z) = b_1z^2 + b_2z^3 + b_3z^4 + \mathcal{O}(|z|^5) \quad (\text{B.10})$$

Again, using (1.15) to derive the equations that $h_1(z)$ and $h_2(z)$ must satisfy for all values of z , and subsequently solving for the coefficients, we find that

$$a_1 = 0, \quad a_2 = 0, \quad a_3 = 0$$

$$b_1 = 0, \quad b_2 = 0, \quad b_3 = 0$$

In this case, the center manifold of the fixed point C is parallel to the z -axis, and its flow is described by

$$z' = \sqrt{6}(\Gamma - 1)z^2 + \mathcal{O}(|z|^3). \quad (\text{B.11})$$

Once again, our focus is on the scenario where $\Gamma > 1$ and $z > 0$. Given the presence of both an unstable and a center manifold in the neighborhood of the fixed point, and the latter being governed by (B.11), we deduce that point C corresponds to an unstable node.

B.3 Fixed point D

To move the fixed point to the origin, we introduce the transformation $\bar{x} = x - 1$. This transformation yields the dynamical system

$$\begin{aligned} \bar{x}' = & 3(1 - w_b)\bar{x} + \sqrt{\frac{3}{2}}zy^2 - 3 + \frac{3}{2}\left[2z(\bar{x} + 1) + (w_b - 1)((z - 1)(\bar{x} + 1)^3 + 3\bar{x}) + \right. \\ & \left. (w_b + 1)((y^2 - 1)(z(\bar{x} + 1) - 1) - \bar{x}y^2)\right] \end{aligned} \quad (\text{B.12a})$$

$$\begin{aligned} y' = & 3y - \sqrt{\frac{3}{2}}yz(\bar{x} + 1) + \\ & \frac{3}{2}y[(w_b + 1)(y^2(z - 1) - z) + (w_b - 1)(\bar{x}(\bar{x} + 2)(z - 1) + z)] \end{aligned} \quad (\text{B.12b})$$

$$z' = -\sqrt{6}z^2(\bar{x} + 1)(1 - z)(\Gamma - 1) \quad (\text{B.12c})$$

The procedure for establishing the center manifold of D is the exact same as that of the fixed point C . The center manifold of D is also parallel to the z -axis, but the flow is now defined by

$$z' = -\sqrt{6}(\Gamma - 1)z^2 + \mathcal{O}(|z|^3) \quad (\text{B.13})$$

From (B.13), we know that trajectories on the center manifold of the fixed point D approach it. Additionally, since this point also possesses an unstable manifold, indicating that trajectories diverge from it, we conclude that it is a saddle point.

Appendix C

Proof of the Rescaled Cosmological Equations

In this appendix, we prove all the equations used in Section 6.3

We begin by rewriting the Friedmann equations, including radiation, matter and dark energy, specifically equations (4.11) and (4.13). Starting with equation (2.16) for the present-day value, the energy density of the i -th component can be expressed as

$$\Omega_{0i} = \frac{\rho_{0i}}{\rho_{0crit}} \xrightarrow{(2.15)} \frac{\kappa^2 \rho_{0i}}{3H_0^2} \xrightarrow{(2.12)} \frac{\kappa^2}{3H_0^2} \rho_i a^{3(1+w_i)} \Rightarrow \rho_i = \frac{3H_0^2}{\kappa^2} \frac{\Omega_{0i}}{a^{3(1+w_i)}}. \quad (C.1)$$

Next, using the fact that $w_r = 1/3$ and $w_m = 0$, the acceleration equation (4.13) takes the form

$$\begin{aligned} \frac{\ddot{a}}{a} &= -\frac{\kappa^2}{6} \left(\rho_m + 2\rho_r + 2\epsilon\dot{\phi}^2 - 2V(\phi) \right) \\ &= -\frac{\kappa^2}{3} \left(\frac{\rho_m}{2} + \rho_r + \epsilon\dot{\phi}^2 - V(\phi) \right) \xrightarrow{(C.1)} \\ \frac{\ddot{a}}{a} &= -H_0^2 \left(\frac{\Omega_{0r}}{a^4} + \frac{\Omega_{0m}}{2a^3} + \frac{\kappa^2}{3H_0^2} \epsilon\dot{\phi}^2 - \frac{\kappa^2}{3H_0^2} V(\phi) \right). \end{aligned} \quad (C.2)$$

Similarly, the first Friedmann equation (4.11) becomes

$$\begin{aligned} \frac{\dot{a}^2}{a^2} &= \frac{\kappa^2}{3} \left(\rho_r + \rho_m + \frac{\epsilon}{2}\dot{\phi}^2 + V(\phi) \right) \xrightarrow{(C.1)} \\ \frac{\dot{a}^2}{a^2} &= H_0^2 \left(\frac{\Omega_{0r}}{a^4} + \frac{\Omega_{0m}}{a^3} + \frac{\kappa^2}{3H_0^2} \frac{\epsilon}{2}\dot{\phi}^2 + \frac{\kappa^2}{3H_0^2} V(\phi) \right). \end{aligned} \quad (C.3)$$

Now, we proceed to obtain the rescaled equations. To achieve this, we must express the time derivatives of the scalar field and the scale factor in terms of the rescaled time variable. We have,

$$\dot{\phi} = \frac{d\phi}{dt} = \frac{\sqrt{3}}{\kappa} H_0 \frac{d(\kappa\phi/\sqrt{3})}{d(H_0 t)} \stackrel{(6.6a)}{\stackrel{(6.6b)}}{=} \frac{\sqrt{3}}{\kappa} H_0 \frac{d\bar{\phi}}{d\bar{t}} = \frac{\sqrt{3}}{\kappa} H_0 \bar{\phi}' \quad (C.4)$$

$$\ddot{\phi} = \frac{d\dot{\phi}}{dt} = H_0 \frac{d\dot{\phi}}{d(H_0 t)} \stackrel{(6.6a)}{\stackrel{(C.4)}}{=} H_0 \frac{\sqrt{3}}{\kappa} H_0 \frac{d\bar{\phi}'}{d\bar{t}} = \frac{\sqrt{3}}{\kappa} H_0^2 \bar{\phi}'' \quad (C.5)$$

$$\dot{a} = \frac{da}{dt} = H_0 \frac{da}{d(H_0 t)} \stackrel{(6.6a)}{=} H_0 \frac{da}{d\bar{t}} = H_0 a' \quad (C.6)$$

$$\ddot{a} = \frac{d\dot{a}}{dt} = H_0 \frac{d\dot{a}}{d(H_0 t)} \stackrel{(6.6a)}{\stackrel{(C.6)}}{=} H_0^2 \frac{da'}{d\bar{t}} = H_0^2 a'' \quad (C.7)$$

$$\frac{\partial V(\phi)}{\partial \phi} = \frac{3H_0^2}{\kappa^2} \frac{\kappa}{\sqrt{3}} \frac{\partial(\kappa^2 V(\phi)/(3H_0^2))}{\partial(\kappa\phi/\sqrt{3})} \stackrel{(6.6a)}{\stackrel{(6.6c)}}{=} \frac{\sqrt{3}}{\kappa} H_0^2 \frac{\partial \bar{V}(\bar{\phi})}{\partial \bar{\phi}} \quad (C.8)$$

where prime denotes the derivative w.r.t. \bar{t} .

At this stage, the goal becomes straightforward. By combining equations (C.2), (6.6c), (C.4) and (C.7), the rescaled acceleration equation takes the form

$$\frac{a''}{a} = -\frac{\Omega_{0r}}{a^4} - \frac{\Omega_{0m}}{2a^3} - \epsilon (\bar{\phi}')^2 + \bar{V}(\bar{\phi}), \quad (C.9)$$

while from equation (C.3), using (6.6c), (C.4) and (C.6), the rescaled first Friedmann equation is

$$\left(\frac{a'}{a}\right)^2 = \frac{\Omega_{0r}}{a^4} + \frac{\Omega_{0m}}{a^3} + \frac{\epsilon}{2} (\bar{\phi}')^2 + \bar{V}(\bar{\phi}). \quad (C.10)$$

The only remaining equation to prove is the rescaled Klein-Gordon equation. By substituting equations (C.4), (C.5), (C.6), and (C.8) into equation (6.4), we obtain the following expression

$$\bar{\phi}'' + 3\frac{a'}{a}\bar{\phi}' + \epsilon \frac{\partial \bar{V}(\bar{\phi})}{\partial \bar{\phi}}. \quad (C.11)$$

Finally, we aim to derive the initial condition presented in equation (6.9a). Assuming matter domination, we can neglect the contributions from radiation and dark energy terms in equation (C.10). Under these assumptions, the rescaled first Friedmann equation simplifies to

$$\frac{a'^2}{a^2} = \frac{\Omega_{0m}}{a^3}. \quad (C.12)$$

To determine the form of the scale factor, we solve this differential equation, which is straightforward to solve.

$$\begin{aligned} a'^2 &= \frac{\Omega_{0m}}{a} \xrightarrow[a'>0]{\text{expansion}} \sqrt{aa'} = \sqrt{\Omega_{0m}} \xrightarrow{\text{Integration}} \\ \frac{2}{3}a^{3/2} &= \sqrt{\Omega_{0m}} \bar{t} + \text{const.} \xrightarrow{\text{const.}=0} a = \left(\frac{9}{4}\Omega_{0m}\right)^{1/3} \bar{t}^{2/3}. \end{aligned} \quad (\text{C.13})$$

Similarly, to find the form of the scale factor during the radiation-dominated era, we neglect the contributions from matter and dark energy terms in equation (C.10). This results in the following simplified form of the rescaled first Friedmann equation

$$\frac{a'^2}{a^2} = \frac{\Omega_{0r}}{a^4}. \quad (\text{C.14})$$

Again, solving this equation is straightforward.

$$\begin{aligned} a'^2 &= \frac{\Omega_{0r}}{a^2} \xrightarrow[a'>0]{\text{expansion}} aa' = \sqrt{\Omega_{0r}} \xrightarrow{\text{Integration}} \\ \frac{1}{2}a^2 &= \sqrt{\Omega_{0r}} \bar{t} + \text{const.} \xrightarrow{\text{const.}=0} a = (4\Omega_{0r})^{1/4} \bar{t}^{1/2}. \end{aligned} \quad (\text{C.15})$$

For completeness, we now calculate the scale factor for a universe where both radiation and matter contribute to its dynamics. In this case, we neglect the dark energy term in equation (C.10), resulting in the following form of the rescaled first Friedmann equation

$$\frac{a'^2}{a^2} = \frac{\Omega_{0r}}{a^4} + \frac{\Omega_{0m}}{a^3}. \quad (\text{C.16})$$

This equation is more complicated than the previous cases. Rearranging the terms we get

$$a'^2 = \frac{\Omega_{0r}}{a^2} \left(1 + \frac{\Omega_{0m}a}{\Omega_{0r}}\right) \xrightarrow[a'>0]{\text{expansion}} a' = \frac{\sqrt{\Omega_{0r}}}{a} \sqrt{1 + \frac{\Omega_{0m}a}{\Omega_{0r}}}. \quad (\text{C.17})$$

Next, we introduce a new variable $b \equiv \frac{\Omega_{0m}}{\Omega_{0r}}$ and integrate this equation.

$$\int_{a_{eq}}^a d\tilde{a} \frac{\tilde{a}}{\sqrt{1 + b\tilde{a}}} = \int_{\bar{t}_{eq}}^{\bar{t}} dt \sqrt{\Omega_{0r}}. \quad (\text{C.18})$$

The left-hand side corresponds to the integral over the scale factor from the matter-radiation equality, $a_{eq} = \frac{1}{b}$, to a general scale factor a , while the right-hand side represents the integration with respect to time. Let us define a new variable $x \equiv 1 + b\tilde{a}$. This allows us to express the differential of \tilde{a} in terms of x , as $d\tilde{a} = \frac{dx}{b}$.

The integration limits, corresponding to $\tilde{a} = a_{eq}$ and $\tilde{a} = a$, are transformed into $x_1 = 1 + ba_{eq}$ and $x_2 = 1 + ba$, respectively. Substituting these into the integral, the left-hand side becomes

$$\begin{aligned} \int_{x_1}^{x_2} \frac{dx}{b^2} \frac{x-1}{\sqrt{x}} &= \int_{x_1}^{x_2} \frac{dx}{b^2} \left(\sqrt{x} - \frac{1}{\sqrt{x}} \right) = \frac{1}{b^2} \left[\frac{2}{3} x^{3/2} - 2x^{1/2} \right]_{x_1}^{x_2} \\ &= \frac{1}{b^2} \left[\frac{2}{3} (1+ba)^{3/2} - 2(1+ba)^{1/2} - \frac{2}{3} (1+ba_{eq})^{3/2} + 2(1+ba_{eq})^{1/2} \right]. \end{aligned} \quad (\text{C.19})$$

By solving the right-hand side integral of equation (C.18) and combining it with the result from equation (C.19), we arrive at the following equation

$$\frac{1}{b^2} \left[\frac{2}{3} (1+ba)^{3/2} - 2(1+ba)^{1/2} - \frac{2}{3} (1+ba_{eq})^{3/2} + 2(1+ba_{eq})^{1/2} \right] = \sqrt{\Omega_{0r}} (\bar{t} - \bar{t}_{eq}). \quad (\text{C.20})$$

This equation enables us to numerically solve for the scale factor in a universe where both radiation and matter contribute to its dynamics, thereby allowing us to determine its functional form.

Bibliography

- [1] K. Freese and M. W. Winkler. “Have pulsar timing arrays detected the hot big bang: Gravitational waves from strong first order phase transitions in the early Universe”. In: *Phys. Rev. D* 106.10 (2022), p. 103523. DOI: [10.1103/PhysRevD.106.103523](https://doi.org/10.1103/PhysRevD.106.103523). arXiv: [2208.03330](https://arxiv.org/abs/2208.03330) [[astro-ph.CO](#)].
- [2] K. Freese and M. W. Winkler. “Dark matter and gravitational waves from a dark big bang”. In: *Phys. Rev. D* 107.8 (2023), p. 083522. DOI: [10.1103/PhysRevD.107.083522](https://doi.org/10.1103/PhysRevD.107.083522). arXiv: [2302.11579](https://arxiv.org/abs/2302.11579) [[astro-ph.CO](#)].
- [3] A. G. Riess et al. “Observational evidence from supernovae for an accelerating universe and a cosmological constant”. In: *Astron. J.* 116 (1998), pp. 1009–1038. DOI: [10.1086/300499](https://doi.org/10.1086/300499). arXiv: [astro-ph/9805201](https://arxiv.org/abs/astro-ph/9805201).
- [4] S. Perlmutter et al. “Measurements of Ω and Λ from 42 High Redshift Supernovae”. In: *Astrophys. J.* 517 (1999), pp. 565–586. DOI: [10.1086/307221](https://doi.org/10.1086/307221). arXiv: [astro-ph/9812133](https://arxiv.org/abs/astro-ph/9812133).
- [5] E. Komatsu et al. “Five-Year Wilkinson Microwave Anisotropy Probe (WMAP) Observations: Cosmological Interpretation”. In: *Astrophys. J. Suppl.* 180 (2009), pp. 330–376. DOI: [10.1088/0067-0049/180/2/330](https://doi.org/10.1088/0067-0049/180/2/330). arXiv: [0803.0547](https://arxiv.org/abs/0803.0547) [[astro-ph](#)].
- [6] R. R. Caldwell, M. Kamionkowski, and N. N. Weinberg. “Phantom energy and cosmic doomsday”. In: *Phys. Rev. Lett.* 91 (2003), p. 071301. DOI: [10.1103/PhysRevLett.91.071301](https://doi.org/10.1103/PhysRevLett.91.071301). arXiv: [astro-ph/0302506](https://arxiv.org/abs/astro-ph/0302506).
- [7] M. Bouhmadi-Lopez et al. “The little sibling of the big rip singularity”. In: *Int. J. Mod. Phys. D* 24.10 (2015), p. 1550078. arXiv: [1407.2446](https://arxiv.org/abs/1407.2446).
- [8] S. Nesseris and L. Perivolaropoulos. “The Fate of bound systems in phantom and quintessence cosmologies”. In: *Phys. Rev. D* 70 (2004), p. 123529. DOI: [10.1103/PhysRevD.70.123529](https://doi.org/10.1103/PhysRevD.70.123529). arXiv: [astro-ph/0410309](https://arxiv.org/abs/astro-ph/0410309).
- [9] M. Dainotti et al. “The Hubble constant tension: current status and future perspectives through new cosmological probes”. In: *PoS CORFU2022* (2023), p. 235. DOI: [10.22323/1.436.0235](https://doi.org/10.22323/1.436.0235). arXiv: [2301.10572](https://arxiv.org/abs/2301.10572) [[astro-ph.CO](#)].

- [10] P. Bull et al. “Beyond Λ CDM: Problems, solutions, and the road ahead”. In: *Phys. Dark Univ.* 12 (2016), pp. 56–99. DOI: [10.1016/j.dark.2016.02.001](https://doi.org/10.1016/j.dark.2016.02.001). arXiv: [1512.05356](https://arxiv.org/abs/1512.05356) [astro-ph.CO].
- [11] J. Martin. “Everything You Always Wanted To Know About The Cosmological Constant Problem (But Were Afraid To Ask)”. In: *Comptes Rendus Physique* 13 (2012), pp. 566–665. DOI: [10.1016/j.crhy.2012.04.008](https://doi.org/10.1016/j.crhy.2012.04.008). arXiv: [1205.3365](https://arxiv.org/abs/1205.3365) [astro-ph.CO].
- [12] A. Del Popolo and M. Le Delliou. “Small scale problems of the Λ CDM model: a short review”. In: *Galaxies* 5.1 (2017), p. 17. DOI: [10.3390/galaxies5010017](https://doi.org/10.3390/galaxies5010017). arXiv: [1606.07790](https://arxiv.org/abs/1606.07790) [astro-ph.CO].
- [13] L. Perivolaropoulos and F. Skara. “Challenges for Λ CDM: An update”. In: *New Astron. Rev.* 95 (2022), p. 101659. DOI: [10.1016/j.newar.2022.101659](https://doi.org/10.1016/j.newar.2022.101659). arXiv: [2105.05208](https://arxiv.org/abs/2105.05208) [astro-ph.CO].
- [14] A. de la Macorra and G. Piccinelli. “General scalar fields as quintessence”. In: *Phys. Rev. D* 61 (2000), p. 123503. DOI: [10.1103/PhysRevD.61.123503](https://doi.org/10.1103/PhysRevD.61.123503). arXiv: [hep-ph/9909459](https://arxiv.org/abs/hep-ph/9909459).
- [15] P. J. E. Peebles and B. Ratra. “Cosmology with a Time Variable Cosmological Constant”. In: *Astrophys. J. Lett.* 325 (1988), p. L17. DOI: [10.1086/185100](https://doi.org/10.1086/185100).
- [16] R. R. Caldwell. “An introduction to quintessence”. In: *Braz. J. Phys.* 30 (2000). Ed. by D. B. Cline, pp. 215–229. DOI: [10.1590/S0103-97332000000200002](https://doi.org/10.1590/S0103-97332000000200002).
- [17] N. Roy. “Exploring the possibility of interacting quintessence model as an alternative to the Λ CDM model”. In: *Gen. Rel. Grav.* 55.10 (2023), p. 115. DOI: [10.1007/s10714-023-03160-1](https://doi.org/10.1007/s10714-023-03160-1). arXiv: [2302.10509](https://arxiv.org/abs/2302.10509) [astro-ph.CO].
- [18] R. G. Landim. “Cosmological perturbations and dynamical analysis for interacting quintessence”. In: *Eur. Phys. J. C* 79.11 (2019), p. 889. DOI: [10.1140/epjc/s10052-019-7418-8](https://doi.org/10.1140/epjc/s10052-019-7418-8). arXiv: [1908.03657](https://arxiv.org/abs/1908.03657) [gr-qc].
- [19] M. Shahalam et al. “Dynamics of interacting quintessence”. In: *Eur. Phys. J. C* 75.8 (2015), p. 395. DOI: [10.1140/epjc/s10052-015-3608-1](https://doi.org/10.1140/epjc/s10052-015-3608-1). arXiv: [1503.08712](https://arxiv.org/abs/1503.08712) [gr-qc].
- [20] P. Pérez, U. Nucamendi, and R. De Arcia. “Revisiting dynamics of interacting quintessence”. In: *Eur. Phys. J. C* 81.12 (2021), p. 1063. DOI: [10.1140/epjc/s10052-021-09857-4](https://doi.org/10.1140/epjc/s10052-021-09857-4). arXiv: [2104.07690](https://arxiv.org/abs/2104.07690) [gr-qc].
- [21] T. Chiba. “Slow-Roll Thawing Quintessence”. In: *Phys. Rev. D* 79 (2009). [Erratum: Phys.Rev.D 80, 109902 (2009)], p. 083517. DOI: [10.1103/PhysRevD.80.109902](https://doi.org/10.1103/PhysRevD.80.109902). arXiv: [0902.4037](https://arxiv.org/abs/0902.4037) [astro-ph.CO].

- [22] G. Gupta, R. Rangarajan, and A. A. Sen. “Thawing quintessence from the inflationary epoch to today”. In: *Phys. Rev. D* 92.12 (2015), p. 123003. DOI: [10.1103/PhysRevD.92.123003](https://doi.org/10.1103/PhysRevD.92.123003). arXiv: [1412.6915](https://arxiv.org/abs/1412.6915) [[astro-ph.CO](#)].
- [23] M. Sahlen, A. R. Liddle, and D. Parkinson. “Quintessence reconstructed: New constraints and tracker viability”. In: *Phys. Rev. D* 75 (2007), p. 023502. DOI: [10.1103/PhysRevD.75.023502](https://doi.org/10.1103/PhysRevD.75.023502). arXiv: [astro-ph/0610812](https://arxiv.org/abs/astro-ph/0610812).
- [24] S. D. Odintsov, V. K. Oikonomou, and G. S. Sharov. “Early dark energy with power-law $F(R)$ gravity”. In: *Phys. Lett. B* 843 (2023), p. 137988. DOI: [10.1016/j.physletb.2023.137988](https://doi.org/10.1016/j.physletb.2023.137988). arXiv: [2305.17513](https://arxiv.org/abs/2305.17513) [[gr-qc](#)].
- [25] J. S. Cruz, F. Niedermann, and M. S. Sloth. “Cold New Early Dark Energy pulls the trigger on the H_0 and S_8 tensions: a simultaneous solution to both tensions without new ingredients”. In: *JCAP* 11 (2023), p. 033. DOI: [10.1088/1475-7516/2023/11/033](https://doi.org/10.1088/1475-7516/2023/11/033). arXiv: [2305.08895](https://arxiv.org/abs/2305.08895) [[astro-ph.CO](#)].
- [26] G. Ye, J. Zhang, and Y.-S. Piao. “Alleviating both H_0 and S_8 tensions: Early dark energy lifts the CMB-lockdown on ultralight axion”. In: *Phys. Lett. B* 839 (2023), p. 137770. DOI: [10.1016/j.physletb.2023.137770](https://doi.org/10.1016/j.physletb.2023.137770). arXiv: [2107.13391](https://arxiv.org/abs/2107.13391) [[astro-ph.CO](#)].
- [27] T. Adi and E. D. Kovetz. “Can conformally coupled modified gravity solve the Hubble tension?” In: *Phys. Rev. D* 103.2 (2021), p. 023530. DOI: [10.1103/PhysRevD.103.023530](https://doi.org/10.1103/PhysRevD.103.023530). arXiv: [2011.13853](https://arxiv.org/abs/2011.13853) [[astro-ph.CO](#)].
- [28] Ö. Akarsu et al. “Relaxing cosmological tensions with a sign switching cosmological constant”. In: *Phys. Rev. D* 104.12 (2021), p. 123512. DOI: [10.1103/PhysRevD.104.123512](https://doi.org/10.1103/PhysRevD.104.123512). arXiv: [2108.09239](https://arxiv.org/abs/2108.09239) [[astro-ph.CO](#)].
- [29] O. Akarsu et al. “Relaxing cosmological tensions with a sign switching cosmological constant: Improved results with Planck, BAO, and Pantheon data”. In: *Phys. Rev. D* 108.2 (2023), p. 023513. DOI: [10.1103/PhysRevD.108.023513](https://doi.org/10.1103/PhysRevD.108.023513). arXiv: [2211.05742](https://arxiv.org/abs/2211.05742) [[astro-ph.CO](#)].
- [30] O. Akarsu et al. “ Λ_s CDM model: A promising scenario for alleviation of cosmological tensions”. In: (July 2023). arXiv: [2307.10899](https://arxiv.org/abs/2307.10899) [[astro-ph.CO](#)].
- [31] E. A. Paraskevas et al. “Transition dynamics in the Λ_s CDM model: Implications for bound cosmic structures”. In: *Phys. Rev. D* 109.10 (2024), p. 103522. DOI: [10.1103/PhysRevD.109.103522](https://doi.org/10.1103/PhysRevD.109.103522). arXiv: [2402.05908](https://arxiv.org/abs/2402.05908) [[astro-ph.CO](#)].
- [32] V. Marra and L. Perivolaropoulos. “Rapid transition of G_{eff} at $z \simeq 0.01$ as a possible solution of the Hubble and growth tensions”. In: *Phys. Rev. D* 104.2 (2021), p. L021303. DOI: [10.1103/PhysRevD.104.L021303](https://doi.org/10.1103/PhysRevD.104.L021303). arXiv: [2102.06012](https://arxiv.org/abs/2102.06012) [[astro-ph.CO](#)].

- [33] I. Banik, H. Desmond, and N. Samaras. “Strong constraints on a sharp change in G as a solution to the Hubble tension”. In: (Nov. 2024). arXiv: [2411.15301 \[astro-ph.CO\]](#).
- [34] G. Alestas et al. “Late-transition versus smooth $H(z)$ -deformation models for the resolution of the Hubble crisis”. In: *Phys. Rev. D* 105.6 (2022), p. 063538. DOI: [10.1103/PhysRevD.105.063538](#). arXiv: [2110.04336 \[astro-ph.CO\]](#).
- [35] G. Alestas, L. Perivolaropoulos, and K. Tanidis. “Constraining a late time transition of G_{eff} using low- z galaxy survey data”. In: *Phys. Rev. D* 106.2 (2022), p. 023526. DOI: [10.1103/PhysRevD.106.023526](#). arXiv: [2201.05846 \[astro-ph.CO\]](#).
- [36] Ruchika, L. Perivolaropoulos, and A. Melchiorri. “Effects of a local physics change on the SH0ES determination of H_0 ”. In: (Aug. 2024). arXiv: [2408.03875 \[astro-ph.CO\]](#).
- [37] L. Perivolaropoulos and F. Skara. “On the homogeneity of SnIa absolute magnitude in the Pantheon+ sample”. In: *Mon. Not. Roy. Astron. Soc.* 520.4 (2023), pp. 5110–5125. DOI: [10.1093/mnras/stad451](#). arXiv: [2301.01024 \[astro-ph.CO\]](#).
- [38] L. Perivolaropoulos and F. Skara. “A Reanalysis of the Latest SH0ES Data for H_0 : Effects of New Degrees of Freedom on the Hubble Tension”. In: *Universe* 8.10 (2022), p. 502. DOI: [10.3390/universe8100502](#). arXiv: [2208.11169 \[astro-ph.CO\]](#).
- [39] L. Perivolaropoulos. “Hubble tension or distance ladder crisis?” In: *Phys. Rev. D* 110.12 (2024), p. 123518. DOI: [10.1103/PhysRevD.110.123518](#). arXiv: [2408.11031 \[astro-ph.CO\]](#).
- [40] G. C. Layek. *An Introduction to Dynamical Systems and Chaos*. Springer, 2015.
- [41] M. Hirsch, S. Smale, and R. L. Devaney. *Differential Equations, Dynamical Systems, and an Introduction to Chaos*. Academic Press, 2013. ISBN: 978-0-12-382010-5.
- [42] L. Perko. *Differential Equations and Dynamical Systems*. Springer, 2009.
- [43] S. Wiggins. *Introduction to Applied Nonlinear Dynamical Systems and Chaos*. Springer, 2003.
- [44] M. P. Hobson, G. Efstathiou, and A. N. Lasenby. *General Relativity. An Introduction for Physicists*. Cambridge University Press, 2006.
- [45] V. Mukhanov. *Physical Foundations of Cosmology*. Cambridge University Press, 2005.

- [46] A. Nindos and C. E. Alissandrakis. *Galactic and Extragalactic Astrophysics (with elements of Cosmology)*. Greek Academic e-books, 2015. URL: https://repository.kallipos.gr/bitstream/11419/5494/3/00_master_document-K0Y.pdf.
- [47] E. Hubble. “A relation between distance and radial velocity among extragalactic nebulae”. In: *Proc. Nat. Acad. Sci.* 15 (1929), pp. 168–173. DOI: [10.1073/pnas.15.3.168](https://doi.org/10.1073/pnas.15.3.168).
- [48] A. Liddle. *An Introduction to Modern Cosmology, 3rd Edition*. John Wiley & Sons, 2015. ISBN: 978-1-118-50214-3.
- [49] P. Kanti. *Cosmology*. Lecture notes for Cosmology in the undergraduate programm in University of Ioannina. 2023.
- [50] M. Tristram et al. “Cosmological parameters derived from the final Planck data release (PR4)”. In: *Astron. Astrophys.* 682 (2024), A37. DOI: [10.1051/0004-6361/202348015](https://doi.org/10.1051/0004-6361/202348015). arXiv: [2309.10034](https://arxiv.org/abs/2309.10034) [[astro-ph.CO](#)].
- [51] E. F. Taylor, J. A. Wheeler, and E. Bertschinge. *Exploring black holes: Introduction to General Relativity*. 2018. URL: <https://archive.org/details/exploringblackholes/mode/2up>.
- [52] R. Rakhi and K. Indulekha. “Dark Energy and Tracker Solution: A Review”. In: (Oct. 2009). arXiv: [0910.5406](https://arxiv.org/abs/0910.5406) [[hep-ph](#)].
- [53] E. J. Copeland, M. Sami, and S. Tsujikawa. “Dynamics of dark energy”. In: *Int. J. Mod. Phys. D* 15 (2006), pp. 1753–1936. DOI: [10.1142/S021827180600942X](https://doi.org/10.1142/S021827180600942X). arXiv: [hep-th/0603057](https://arxiv.org/abs/hep-th/0603057).
- [54] V. Gorini et al. “The Chaplygin gas as a model for dark energy”. In: *10th Marcel Grossmann Meeting on Recent Developments in Theoretical and Experimental General Relativity, Gravitation and Relativistic Field Theories (MG X MMIII)*. Mar. 2004, pp. 840–859. DOI: [10.1142/9789812704030_0050](https://doi.org/10.1142/9789812704030_0050). arXiv: [gr-qc/0403062](https://arxiv.org/abs/gr-qc/0403062).
- [55] M. C. Bento, O. Bertolami, and A. A. Sen. “Generalized Chaplygin gas, accelerated expansion and dark energy matter unification”. In: *Phys. Rev. D* 66 (2002), p. 043507. DOI: [10.1103/PhysRevD.66.043507](https://doi.org/10.1103/PhysRevD.66.043507). arXiv: [gr-qc/0202064](https://arxiv.org/abs/gr-qc/0202064).
- [56] T. P. Sotiriou and V. Faraoni. “f(R) Theories Of Gravity”. In: *Rev. Mod. Phys.* 82 (2010), pp. 451–497. DOI: [10.1103/RevModPhys.82.451](https://doi.org/10.1103/RevModPhys.82.451). arXiv: [0805.1726](https://arxiv.org/abs/0805.1726) [[gr-qc](#)].
- [57] L. Amendola, D. Polarski, and S. Tsujikawa. “Are f(R) dark energy models cosmologically viable ?” In: *Phys. Rev. Lett.* 98 (2007), p. 131302. DOI: [10.1103/PhysRevLett.98.131302](https://doi.org/10.1103/PhysRevLett.98.131302). arXiv: [astro-ph/0603703](https://arxiv.org/abs/astro-ph/0603703).

- [58] S. Nojiri and S. D. Odintsov. “Modified $f(R)$ gravity consistent with realistic cosmology: From matter dominated epoch to dark energy universe”. In: *Phys. Rev. D* 74 (2006), p. 086005. DOI: [10.1103/PhysRevD.74.086005](https://doi.org/10.1103/PhysRevD.74.086005). arXiv: [hep-th/0608008](https://arxiv.org/abs/hep-th/0608008).
- [59] S. J. C. McGrand. “Dark Energy and Modified Gravity: A Dynamical Systems Approach”. MA thesis. Imperial College London, 2020. URL: <https://www.imperial.ac.uk/media/imperial-college/research-centres-and-groups/theoretical-physics/msc/dissertations/2020/Samuel-Carter-McGrand-Dissertation.pdf>.
- [60] K. Enqvist. “Lemaitre-Tolman-Bondi model and accelerating expansion”. In: *Gen. Rel. Grav.* 40 (2008), pp. 451–466. DOI: [10.1007/s10714-007-0553-9](https://doi.org/10.1007/s10714-007-0553-9). arXiv: [0709.2044](https://arxiv.org/abs/0709.2044) [[astro-ph](#)].
- [61] S. Rasanen. “Accelerated expansion from structure formation”. In: *JCAP* 11 (2006), p. 003. DOI: [10.1088/1475-7516/2006/11/003](https://doi.org/10.1088/1475-7516/2006/11/003). arXiv: [astro-ph/0607626](https://arxiv.org/abs/astro-ph/0607626).
- [62] J. R. Ellis, N. E. Mavromatos, and D. V. Nanopoulos. “String theory and an accelerating universe”. In: (May 2001). arXiv: [hep-th/0105206](https://arxiv.org/abs/hep-th/0105206).
- [63] C. E. Alissandrakis. *Introduction to Astrophysics*. Papazissi Publications, 2014. ISBN: 978-960-02-3058-1.
- [64] J. Storm et al. “Calibrating the Cepheid Period-Luminosity relation from the infrared surface brightness technique I. The p-factor, the Milky Way relations, and a universal K-band relation”. In: *Astron. Astrophys.* 534 (2011), A94. DOI: [10.1051/0004-6361/201117155](https://doi.org/10.1051/0004-6361/201117155). arXiv: [1109.2017](https://arxiv.org/abs/1109.2017) [[astro-ph.CO](#)].
- [65] M. Signore and D. Puy. “Supernova and cosmology”. In: *New Astron. Rev.* 45 (2001), pp. 409–423. DOI: [10.1016/S1387-6473\(00\)00163-9](https://doi.org/10.1016/S1387-6473(00)00163-9). arXiv: [astro-ph/0010634](https://arxiv.org/abs/astro-ph/0010634).
- [66] M. M. Phillips. “The absolute magnitudes of Type IA supernovae”. In: *Astrophys. J. Lett.* 413 (1993), pp. L105–L108. DOI: [10.1086/186970](https://doi.org/10.1086/186970).
- [67] M. Pettini. *Recombination and the Cosmic Microwave Background*. Introduction to Cosmology — Lecture 9. 2018. URL: <https://people.ast.cam.ac.uk/~pettini/Intro%20Cosmology/Lecture09.pdf>.
- [68] B. Ryden. *Introduction to cosmology*. 2nd ed. Cambridge University Press, 2016. ISBN: 978-1-316-65108-7. DOI: [10.1017/9781316651087](https://doi.org/10.1017/9781316651087).
- [69] M. Pettini. *Fluctuations in the Cosmic Microwave Background*. Introduction to Cosmology — Lecture 10. 2018. URL: <https://people.ast.cam.ac.uk/~pettini/Intro%20Cosmology/Lecture10.pdf>.

- [70] M. Pettini. *Large Scale Structure*. Introduction to Cosmology — Lecture 14. 2018. URL: <https://people.ast.cam.ac.uk/~pettini/Intro%20Cosmology/Lecture14.pdf>.
- [71] D. J. Eisenstein and W. Hu. “Baryonic features in the matter transfer function”. In: *Astrophys. J.* 496 (1998), p. 605. DOI: [10.1086/305424](https://doi.org/10.1086/305424). arXiv: [astro-ph/9709112](https://arxiv.org/abs/astro-ph/9709112).
- [72] L. Kazantzidis, L. Perivolaropoulos, and F. Skara. “Constraining power of cosmological observables: blind redshift spots and optimal ranges”. In: *Phys. Rev. D* 99.6 (2019), p. 063537. DOI: [10.1103/PhysRevD.99.063537](https://doi.org/10.1103/PhysRevD.99.063537). arXiv: [1812.05356](https://arxiv.org/abs/1812.05356) [[astro-ph](https://arxiv.org/abs/astro-ph).C0].
- [73] A. Theodoropoulos and L. Perivolaropoulos. “The Hubble Tension, the M Crisis of Late Time H(z) Deformation Models and the Reconstruction of Quintessence Lagrangians”. In: *Universe* 7.8 (2021), p. 300. DOI: [10.3390/universe7080300](https://doi.org/10.3390/universe7080300). arXiv: [2109.06256](https://arxiv.org/abs/2109.06256) [[astro-ph](https://arxiv.org/abs/astro-ph).C0].
- [74] É. Aubourg et al. “Cosmological implications of baryon acoustic oscillation measurements”. In: *Phys. Rev. D* 92.12 (2015), p. 123516. DOI: [10.1103/PhysRevD.92.123516](https://doi.org/10.1103/PhysRevD.92.123516). arXiv: [1411.1074](https://arxiv.org/abs/1411.1074) [[astro-ph](https://arxiv.org/abs/astro-ph).C0].
- [75] N. Aghanim et al. “Planck 2018 results. VI. Cosmological parameters”. In: *Astron. Astrophys.* 641 (2020). [Erratum: *Astron. Astrophys.* 652, C4 (2021)], A6. DOI: [10.1051/0004-6361/201833910](https://doi.org/10.1051/0004-6361/201833910). arXiv: [1807.06209](https://arxiv.org/abs/1807.06209) [[astro-ph](https://arxiv.org/abs/astro-ph).C0].
- [76] S. Navas et al. “Review of particle physics”. In: *Phys. Rev. D* 110.3 (2024), p. 030001. DOI: [10.1103/PhysRevD.110.030001](https://doi.org/10.1103/PhysRevD.110.030001).
- [77] Y. Wang and P. Mukherjee. “Observational Constraints on Dark Energy and Cosmic Curvature”. In: *Phys. Rev. D* 76 (2007), p. 103533. DOI: [10.1103/PhysRevD.76.103533](https://doi.org/10.1103/PhysRevD.76.103533). arXiv: [astro-ph/0703780](https://arxiv.org/abs/astro-ph/0703780).
- [78] M. O. Farooq. “Observational constraints on dark energy cosmological model parameters”. Other thesis. Sept. 2013. arXiv: [1309.3710](https://arxiv.org/abs/1309.3710) [[astro-ph](https://arxiv.org/abs/astro-ph).C0].
- [79] E. V. Linder. “The Dynamics of Quintessence, The Quintessence of Dynamics”. In: *Gen. Rel. Grav.* 40 (2008), pp. 329–356. DOI: [10.1007/s10714-007-0550-z](https://doi.org/10.1007/s10714-007-0550-z). arXiv: [0704.2064](https://arxiv.org/abs/0704.2064) [[astro-ph](https://arxiv.org/abs/astro-ph)].
- [80] W. Liu, J. Ouyang, and H. Yang. “Quintessence Field as a Perfect Cosmic Fluid of Constant Pressure”. In: *Commun. Theor. Phys.* 63.3 (2015), pp. 391–400. DOI: [10.1088/0253-6102/63/3/391](https://doi.org/10.1088/0253-6102/63/3/391). arXiv: [1211.0219](https://arxiv.org/abs/1211.0219) [[astro-ph](https://arxiv.org/abs/astro-ph).C0].
- [81] R. R. Caldwell. “A Phantom menace?” In: *Phys. Lett. B* 545 (2002), pp. 23–29. DOI: [10.1016/S0370-2693\(02\)02589-3](https://doi.org/10.1016/S0370-2693(02)02589-3). arXiv: [astro-ph/9908168](https://arxiv.org/abs/astro-ph/9908168).

- [82] L. Perivolaropoulos. “Constraints on linear negative potentials in quintessence and phantom models from recent supernova data”. In: *Phys. Rev. D* 71 (2005), p. 063503. DOI: [10.1103/PhysRevD.71.063503](https://doi.org/10.1103/PhysRevD.71.063503). arXiv: [astro-ph/0412308](https://arxiv.org/abs/astro-ph/0412308).
- [83] S. Bahamonde et al. “Dynamical systems applied to cosmology: dark energy and modified gravity”. In: *Phys. Rept.* 775-777 (2018), pp. 1–122. DOI: [10.1016/j.physrep.2018.09.001](https://doi.org/10.1016/j.physrep.2018.09.001). arXiv: [1712.03107 \[gr-qc\]](https://arxiv.org/abs/1712.03107).
- [84] E. J. Copeland, A. R. Liddle, and D. Wands. “Exponential potentials and cosmological scaling solutions”. In: *Phys. Rev. D* 57 (1998), pp. 4686–4690. DOI: [10.1103/PhysRevD.57.4686](https://doi.org/10.1103/PhysRevD.57.4686). arXiv: [gr-qc/9711068](https://arxiv.org/abs/gr-qc/9711068).
- [85] W. Fang et al. “Exact Analysis of Scaling and Dominant Attractors Beyond the Exponential Potential”. In: *Class. Quant. Grav.* 26 (2009), p. 155005. DOI: [10.1088/0264-9381/26/15/155005](https://doi.org/10.1088/0264-9381/26/15/155005). arXiv: [0810.4193 \[hep-th\]](https://arxiv.org/abs/0810.4193).
- [86] E. Jensko. “Scalar fields in cosmology: a dynamical systems approach”. MA thesis. School of Mathematical Sciences, University of Nottingham, 2018. URL: https://www.ucl.ac.uk/~ucaheje/PDF/MSc_Thesis.pdf.
- [87] C. G. Boehmer and N. Chan. “Dynamical systems in cosmology.” In: 2017. DOI: [10.1142/9781786341044_0004](https://doi.org/10.1142/9781786341044_0004). arXiv: [1409.5585 \[gr-qc\]](https://arxiv.org/abs/1409.5585).
- [88] G. R. Blumenthal et al. “Formation of Galaxies and Large Scale Structure with Cold Dark Matter”. In: *Nature* 311 (1984). Ed. by M. A. Srednicki, pp. 517–525. DOI: [10.1038/311517a0](https://doi.org/10.1038/311517a0).
- [89] K. Garrett and G. Duda. “Dark Matter: A Primer”. In: *Adv. Astron.* 2011 (2011), p. 968283. DOI: [10.1155/2011/968283](https://doi.org/10.1155/2011/968283). arXiv: [1006.2483 \[hep-ph\]](https://arxiv.org/abs/1006.2483).
- [90] A. H. G. Peter. “Dark Matter: A Brief Review”. In: (Jan. 2012). arXiv: [1201.3942 \[astro-ph.CO\]](https://arxiv.org/abs/1201.3942).
- [91] K. A. Olive. “TASI lectures on dark matter”. In: *Theoretical Advanced Study Institute in Elementary Particle Physics (TASI 2002): Particle Physics and Cosmology: The Quest for Physics Beyond the Standard Model(s)*. Jan. 2003, pp. 797–851. arXiv: [astro-ph/0301505](https://arxiv.org/abs/astro-ph/0301505).
- [92] F. Chadha-Day, J. Ellis, and D. J. E. Marsh. “Axion dark matter: What is it and why now?” In: *Sci. Adv.* 8.8 (2022), abj3618. DOI: [10.1126/sciadv.abj3618](https://doi.org/10.1126/sciadv.abj3618). arXiv: [2105.01406 \[hep-ph\]](https://arxiv.org/abs/2105.01406).
- [93] N. Sivanandam. “Is the Cosmological Coincidence a Problem?” In: *Phys. Rev. D* 87.8 (2013), p. 083514. DOI: [10.1103/PhysRevD.87.083514](https://doi.org/10.1103/PhysRevD.87.083514). arXiv: [1203.4197 \[astro-ph.CO\]](https://arxiv.org/abs/1203.4197).

- [94] S. Weinberg. “The Cosmological Constant Problem”. In: *Rev. Mod. Phys.* 61 (1989). Ed. by J.-P. Hsu and D. Fine, pp. 1–23. DOI: [10.1103/RevModPhys.61.1](https://doi.org/10.1103/RevModPhys.61.1).
- [95] P. P. Avelino. “The Coincidence problem in linear dark energy models”. In: *Phys. Lett. B* 611 (2005), pp. 15–20. DOI: [10.1016/j.physletb.2005.02.037](https://doi.org/10.1016/j.physletb.2005.02.037). arXiv: [astro-ph/0411033](https://arxiv.org/abs/astro-ph/0411033).
- [96] D. Brout et al. “The Pantheon+ Analysis: Cosmological Constraints”. In: *Astrophys. J.* 938.2 (2022), p. 110. DOI: [10.3847/1538-4357/ac8e04](https://doi.org/10.3847/1538-4357/ac8e04). arXiv: [2202.04077](https://arxiv.org/abs/2202.04077) [[astro-ph.CO](#)].
- [97] L. N. Granda and D. F. Jimenez. “Slow-Roll Inflation with Exponential Potential in Scalar-Tensor Models”. In: *Eur. Phys. J. C* 79.9 (2019), p. 772. DOI: [10.1140/epjc/s10052-019-7289-z](https://doi.org/10.1140/epjc/s10052-019-7289-z). arXiv: [1907.06806](https://arxiv.org/abs/1907.06806) [[hep-th](#)].
- [98] D. Wands. “Extended gravity theories and the Einstein-Hilbert action”. In: *Class. Quant. Grav.* 11 (1994), pp. 269–280. DOI: [10.1088/0264-9381/11/1/025](https://doi.org/10.1088/0264-9381/11/1/025). arXiv: [gr-qc/9307034](https://arxiv.org/abs/gr-qc/9307034).
- [99] D. Baumann and L. McAllister. *Inflation and String Theory*. Cambridge Monographs on Mathematical Physics. Cambridge University Press, May 2015. ISBN: 978-1-107-08969-3. DOI: [10.1017/CB09781316105733](https://doi.org/10.1017/CB09781316105733). arXiv: [1404.2601](https://arxiv.org/abs/1404.2601) [[hep-th](#)].
- [100] E. Dudas, N. Kitazawa, and A. Sagnotti. “On Climbing Scalars in String Theory”. In: *Phys. Lett. B* 694 (2011), pp. 80–88. DOI: [10.1016/j.physletb.2010.09.040](https://doi.org/10.1016/j.physletb.2010.09.040). arXiv: [1009.0874](https://arxiv.org/abs/1009.0874) [[hep-th](#)].
- [101] P.-H. Chavanis. “Cosmology with a stiff matter era”. In: *Phys. Rev. D* 92.10 (2015), p. 103004. DOI: [10.1103/PhysRevD.92.103004](https://doi.org/10.1103/PhysRevD.92.103004). arXiv: [1412.0743](https://arxiv.org/abs/1412.0743) [[gr-qc](#)].
- [102] Y. B. Zel’dovich. “The equation of state at ultrahigh densities and its relativistic limitations”. In: *Zh. Eksp. Teor. Fiz.* 41 (1961), pp. 1609–1615.
- [103] P. G. Ferreira and M. Joyce. “Structure formation with a selftuning scalar field”. In: *Phys. Rev. Lett.* 79 (1997), pp. 4740–4743. DOI: [10.1103/PhysRevLett.79.4740](https://doi.org/10.1103/PhysRevLett.79.4740). arXiv: [astro-ph/9707286](https://arxiv.org/abs/astro-ph/9707286).
- [104] T. Barreiro, E. J. Copeland, and N. J. Nunes. “Quintessence arising from exponential potentials”. In: *Phys. Rev. D* 61 (2000), p. 127301. DOI: [10.1103/PhysRevD.61.127301](https://doi.org/10.1103/PhysRevD.61.127301). arXiv: [astro-ph/9910214](https://arxiv.org/abs/astro-ph/9910214).
- [105] P. Binetruy. “Models of dynamical supersymmetry breaking and quintessence”. In: *Phys. Rev. D* 60 (1999), p. 063502. DOI: [10.1103/PhysRevD.60.063502](https://doi.org/10.1103/PhysRevD.60.063502). arXiv: [hep-ph/9810553](https://arxiv.org/abs/hep-ph/9810553).

- [106] I. Zlatev, L.-M. Wang, and P. J. Steinhardt. “Quintessence, cosmic coincidence, and the cosmological constant”. In: *Phys. Rev. Lett.* 82 (1999), pp. 896–899. DOI: [10.1103/PhysRevLett.82.896](https://doi.org/10.1103/PhysRevLett.82.896). arXiv: [astro-ph/9807002](https://arxiv.org/abs/astro-ph/9807002).
- [107] P. J. Steinhardt, L.-M. Wang, and I. Zlatev. “Cosmological tracking solutions”. In: *Phys. Rev. D* 59 (1999), p. 123504. DOI: [10.1103/PhysRevD.59.123504](https://doi.org/10.1103/PhysRevD.59.123504). arXiv: [astro-ph/9812313](https://arxiv.org/abs/astro-ph/9812313).
- [108] S. C. C. Ng, N. J. Nunes, and F. Rosati. “Applications of scalar attractor solutions to cosmology”. In: *Phys. Rev. D* 64 (2001), p. 083510. DOI: [10.1103/PhysRevD.64.083510](https://doi.org/10.1103/PhysRevD.64.083510). arXiv: [astro-ph/0107321](https://arxiv.org/abs/astro-ph/0107321).
- [109] M. Yashar et al. “Exploring Parameter Constraints on Quintessential Dark Energy: the Inverse Power Law Model”. In: *Phys. Rev. D* 79 (2009), p. 103004. DOI: [10.1103/PhysRevD.79.103004](https://doi.org/10.1103/PhysRevD.79.103004). arXiv: [0811.2253 \[astro-ph\]](https://arxiv.org/abs/0811.2253).
- [110] L. A. Urena-Lopez. “Unified description of the dynamics of quintessential scalar fields”. In: *JCAP* 03 (2012), p. 035. DOI: [10.1088/1475-7516/2012/03/035](https://doi.org/10.1088/1475-7516/2012/03/035). arXiv: [1108.4712 \[astro-ph.CO\]](https://arxiv.org/abs/1108.4712).
- [111] F. Giovi, C. Baccigalupi, and F. Perrotta. “Constraining the dark energy dynamics with the cosmic microwave background bispectrum”. In: *Phys. Rev. D* 68 (2003), p. 123002. DOI: [10.1103/PhysRevD.68.123002](https://doi.org/10.1103/PhysRevD.68.123002). arXiv: [astro-ph/0308118](https://arxiv.org/abs/astro-ph/0308118).
- [112] S. Tsujikawa. “Quintessence: A Review”. In: *Class. Quant. Grav.* 30 (2013), p. 214003. DOI: [10.1088/0264-9381/30/21/214003](https://doi.org/10.1088/0264-9381/30/21/214003). arXiv: [1304.1961 \[gr-qc\]](https://arxiv.org/abs/1304.1961).
- [113] S. M. Carroll. “Quintessence and the rest of the world”. In: *Phys. Rev. Lett.* 81 (1998), pp. 3067–3070. DOI: [10.1103/PhysRevLett.81.3067](https://doi.org/10.1103/PhysRevLett.81.3067). arXiv: [astro-ph/9806099](https://arxiv.org/abs/astro-ph/9806099).
- [114] I. Leanizbarrutia, A. Rozas-Fernández, and I. Tereno. “Cosmological constraints on a unified dark matter-energy scalar field model with fast transition”. In: *Phys. Rev. D* 96.2 (2017), p. 023503. DOI: [10.1103/PhysRevD.96.023503](https://doi.org/10.1103/PhysRevD.96.023503). arXiv: [1706.01706 \[astro-ph.CO\]](https://arxiv.org/abs/1706.01706).
- [115] D. Bertacca et al. “Unified Dark Matter scalar field models with fast transition”. In: *JCAP* 02 (2011), p. 018. DOI: [10.1088/1475-7516/2011/02/018](https://doi.org/10.1088/1475-7516/2011/02/018). arXiv: [1011.6669 \[astro-ph.CO\]](https://arxiv.org/abs/1011.6669).
- [116] E. Frion et al. “Bayesian analysis of a Unified Dark Matter model with transition: can it alleviate the H_0 tension?” In: (July 2023). DOI: [10.21105/astro.2307.06320](https://doi.org/10.21105/astro.2307.06320). arXiv: [2307.06320 \[astro-ph.CO\]](https://arxiv.org/abs/2307.06320).

- [117] R. Lazkoz, I. Leanizbarrutia, and V. Salzano. “Cosmological constraints on fast transition unified dark energy and dark matter models”. In: *Phys. Rev. D* 93.4 (2016), p. 043537. DOI: [10.1103/PhysRevD.93.043537](https://doi.org/10.1103/PhysRevD.93.043537). arXiv: [1602.01331](https://arxiv.org/abs/1602.01331) [[astro-ph.CO](#)].
- [118] Y. Wang et al. “Evolution of dark energy reconstructed from the latest observations”. In: *Astrophys. J. Lett.* 869 (2018), p. L8. DOI: [10.3847/2041-8213/aaf238](https://doi.org/10.3847/2041-8213/aaf238). arXiv: [1807.03772](https://arxiv.org/abs/1807.03772) [[astro-ph.CO](#)].
- [119] A. Mehrabi and M. Vazirnia. “Reconstruction of dark energy density by non-parametric approaches”. In: (Jan. 2022). arXiv: [2201.04993](https://arxiv.org/abs/2201.04993) [[astro-ph.CO](#)].
- [120] Ö. Akarsu et al. “Graduated dark energy: Observational hints of a spontaneous sign switch in the cosmological constant”. In: *Phys. Rev. D* 101.6 (2020), p. 063528. DOI: [10.1103/PhysRevD.101.063528](https://doi.org/10.1103/PhysRevD.101.063528). arXiv: [1912.08751](https://arxiv.org/abs/1912.08751) [[astro-ph.CO](#)].
- [121] D. H. Weinberg et al. “A Lower bound on the cosmic baryon density”. In: *Astrophys. J.* 490 (1997), pp. 564–570. DOI: [10.1086/304893](https://doi.org/10.1086/304893). arXiv: [astro-ph/9701012](https://arxiv.org/abs/astro-ph/9701012).
- [122] B. W. Keller et al. “Can Cosmological Simulations Reproduce the Spectroscopically Confirmed Galaxies Seen at $z \geq 10$?” In: *Astrophys. J. Lett.* 943.2 (2023), p. L28. DOI: [10.3847/2041-8213/acb148](https://doi.org/10.3847/2041-8213/acb148). arXiv: [2212.12804](https://arxiv.org/abs/2212.12804) [[astro-ph.GA](#)].
- [123] J. McCaffrey et al. “No Tension: JWST Galaxies at $z > 10$ Consistent with Cosmological Simulations”. In: (Apr. 2023). DOI: [10.21105/astro.2304.13755](https://doi.org/10.21105/astro.2304.13755). arXiv: [2304.13755](https://arxiv.org/abs/2304.13755) [[astro-ph.GA](#)].
- [124] Z. Zhai and Y. Wang. “Robust and model-independent cosmological constraints from distance measurements”. In: *JCAP* 07 (2019), p. 005. DOI: [10.1088/1475-7516/2019/07/005](https://doi.org/10.1088/1475-7516/2019/07/005). arXiv: [1811.07425](https://arxiv.org/abs/1811.07425) [[astro-ph.CO](#)].
- [125] C. Escamilla-Rivera. “Status on bidimensional dark energy parameterizations using SNe Ia JLA and BAO datasets”. In: *Galaxies* 4.3 (2016), p. 8. DOI: [10.3390/galaxies4030008](https://doi.org/10.3390/galaxies4030008). arXiv: [1605.02702](https://arxiv.org/abs/1605.02702) [[astro-ph.CO](#)].
- [126] H. Akaike. “A new look at the statistical model identification”. In: *IEEE Trans. Automatic Control* 19.6 (1974), pp. 716–723. DOI: [10.1109/TAC.1974.1100705](https://doi.org/10.1109/TAC.1974.1100705).
- [127] G. Schwarz. “Estimating the Dimension of a Model”. In: *Annals Statist.* 6 (1978), pp. 461–464.
- [128] D. Camarena and V. Marra. “Impact of the cosmic variance on H_0 on cosmological analyses”. In: *Phys. Rev. D* 98.2 (2018), p. 023537. DOI: [10.1103/PhysRevD.98.023537](https://doi.org/10.1103/PhysRevD.98.023537). arXiv: [1805.09900](https://arxiv.org/abs/1805.09900) [[astro-ph.CO](#)].

- [129] A. G. Riess et al. “A Comprehensive Measurement of the Local Value of the Hubble Constant with $1 \text{ km s}^{-1} \text{ Mpc}^{-1}$ Uncertainty from the Hubble Space Telescope and the SH0ES Team”. In: *Astrophys. J. Lett.* 934.1 (2022), p. L7. DOI: [10.3847/2041-8213/ac5c5b](https://doi.org/10.3847/2041-8213/ac5c5b). arXiv: [2112.04510](https://arxiv.org/abs/2112.04510) [[astro-ph.CO](#)].
- [130] C. Skordis and A. Albrecht. “Planck scale quintessence and the physics of structure formation”. In: *Phys. Rev. D* 66 (2002), p. 043523. DOI: [10.1103/PhysRevD.66.043523](https://doi.org/10.1103/PhysRevD.66.043523). arXiv: [astro-ph/0012195](https://arxiv.org/abs/astro-ph/0012195).
- [131] P. Brax and J. Martin. “The Robustness of quintessence”. In: *Phys. Rev. D* 61 (2000), p. 103502. DOI: [10.1103/PhysRevD.61.103502](https://doi.org/10.1103/PhysRevD.61.103502). arXiv: [astro-ph/9912046](https://arxiv.org/abs/astro-ph/9912046).
- [132] A. Paliathanasis et al. “Dynamical analysis in scalar field cosmology”. In: *Phys. Rev. D* 91.12 (2015), p. 123535. DOI: [10.1103/PhysRevD.91.123535](https://doi.org/10.1103/PhysRevD.91.123535). arXiv: [1503.05750](https://arxiv.org/abs/1503.05750) [[gr-qc](#)].